Search for Supersymmetry using Heavy Flavour Jets with the ATLAS Detector at the Large Hadron Collider

Alan Tua

Supervisor: Davide Costanzo

A Thesis Submitted for the
Degree of Doctor Of Philosophy in Physics

Department of Physics and Astronomy
University of Sheffield, September 2012

To Mama and Papa

The research work disclosed in this publication is partially funded by the Strategic Educational Pathways Scholarship (Malta). The scholarship is part-financed by the European Union - European Social Fund (ESF) under Operational Programme II - Cohesion Policy 2007-2013, "Empowering People for More Jobs and a Better Quality of Life"

Operational Programme II - Cohesion Policy 2007-2013

"Empowering People for More Jobs and a Better Quality of Life"

Scholarship part financed by the European Union European Social Fund (ESF).

Co-financing rate: 85% EU Funds, 15% National Funds

Investing in your future

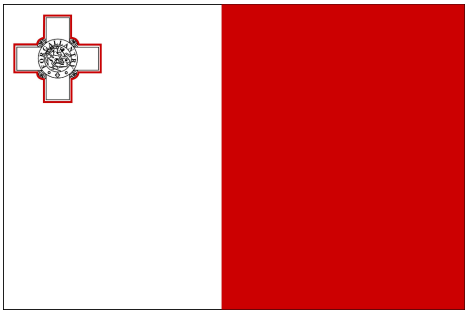

Abstract

The Standard Model of particle physics, despite being extremely successful, is not the ultimate description of physics. The nature of dark matter is not well described, unification of the forces is not achieved and the theory is plagued by a hierarchy problem. One of the proposed solutions to these issues is supersymmetry.

This thesis describes numerous searches for supersymmetry carried out using the ATLAS detector at the Large Hadron Collider. In scenarios where R-parity is conserved, supersymmetric final states contain large amounts of missing transverse energy. Furthermore, should supersymmetry correctly describe Nature, the scalar partners of the third generation quarks might be the lightest scalar quarks. The searches reported here exploit these possibilities and make use of signatures which are rich in missing transverse energy and jets coming from heavy flavour quarks.

Searches are carried out for direct pair production of third generation scalar quarks as well as gluino-mediated production of these particles. A data driven technique to estimate the backgrounds coming from multijet production is described and shown to work in analyses targeting heavy flavour quarks. No significant excesses are observed in a number of analyses. In each case limits are set on the allowed masses of supersymmetric particles in a variety of phenomenological models and in specific supersymmetry breaking scenarios.

Acknowledgments

I would first of all like to thank my supervisor, Davide Costanzo, for his guidance in physics matters and his appreciation of what the English weather can do to somebody accustomed to the Mediterranean sea. I would definitely be far less of a physicist if it were not for you. Many thanks also to Dan Tovey for his helpful advice throughout my PhD. Thanks to all the ATLAS HEP staff at Sheffield for their help during the years. In particular I would like to mention Matt Robinson, Paul Hodgson, Elena Korolkova for their computing expertise and Rob Duxfield, Kerim Suruliz and Mark Hodgkinson for sharing their physics experience. To Josh, Steve, Gary and Simon I say thank you for putting up with my rants about English cuisine, as well continuing to play office badminton against me, even when it was clear that I was far better than any of you.

Thank you to the Sheffield Graduate Scheme Scholarship for funding my PhD as well as my stay in Sheffield and thank you to the administrators of the STEPS programme, without which it would have been financially impossible for me to spend so much time based at CERN.

The work in this thesis owes a great deal to many people in the ATLAS SUSY group. In particular I would like to thank Monica D'Onofrio from whom I learnt an incredible amount of physics and a thing or two about dedication. Similarly I would like to acknowledge Xavi Portell, Iacopo Vivarelli and Antoine Marzin for their insights and knowledge, along with other members of the SUSY with b-jets team and the SUSY Working Group, including Bart, Takashi, TJ and Chris.

Sheffield would have been nowhere near as fun were it not for some of the local and not-so-local people I got to know. Thank you Hazel, Rachel, Julia and Melvin for adding a few kilos to my waistline. Similarly, going back to sunny Malta was only so relaxing because of the proverbial "dawgs" at home; Benji, Saliba, Barb, Japan, Moses, Jesmar and their various better halves... Thank you Sandro Grech from San Alwiġi and Charles Sammut and Kris Żarb Adami from the University of Malta, who

instilled in me the desire to continue studying physics and the confidence to pursue a doctorate.

I would like to express my gratitude to my parents for constantly supporting me throughout my life. A bonus thank you goes to Mama for proof reading this document. Thank you to Jeremy, for always agreeing to join me on my Maltese-restaurant-sprees whenever I was back home. Finally, a massive thank you to Angelica, for forcing me to go jogging, enjoying ridiculously good food with me, being a super proof-reader and being absolutely awesome in the good times and the tough times.

Author's Contributions

The material presented in this thesis is based upon work performed by a large number of people in the ATLAS collaboration. The author's contribution will be stated explicitly at the start of each chapter and is summarised here for completeness.

Service Work

The author was responsible for maintaining and developing the Full Chain Testing framework, described in Section 4.3. The author also took numerous "Computing at Point 1" shifts; these involved checking the functionality and integrity of ATLAS IT services at CERN and monitoring the data flow from the CERN Tier 0 computing farm to Tier 1 and Tier 2 sites around the world.

Multijet Background Estimation

The author worked on the multijet background estimation in a number of searches for supersymmetry which veto leptons and require heavy flavour jets. The author used this method as the default multijet background estimation technique in a number of journal papers and conference notes [1] [2] [3] [4] [5] [6]. It was also used as a cross-check of another data driven method in a search for supersymmetry requiring high jet multiplicity [7].

Searches for Supersymmetry

The focus of the author's work was the search for supersymmetry using heavy flavour jets. This work is described in Chapter 6 [2] , Chapter 7 [1] [8] [2] [4] and Chapter 8 [5] [8]. Contributions include the optimisation of the analyses, the study of the signal properties, the multijet background estimation and the statistical interpretation of the results. The author also carried out various cross-checks of yields, non-multijet background estimates and distributions.

The author also made minor contributions to a number of other ATLAS searches for supersymmetry, via contributions to the generation of signal samples [9] or help with the interpretation of results [10].

Other Contributions

The author presented various SUSY results at a number of national and international conferences and meetings. These included talks in the UK at ATLAS UK 2010 (London) and the IOP HEP 2012 meeting (London). The author spoke on behalf of the ATLAS collaboration at Pheno 2011 (Wisconsin) and presented a poster at Physics In Collision 2012 (Vancouver). Finally, the author has spoken on behalf of both the ATLAS and CMS collaborations at the Implications of LHC Physics Workshop held at CERN (2012).

Contents

List of Tables

List of Figures

Chapter 1

Introduction

Il-mistoqsija oħt il-għerf[1]

The search for supersymmetry is one of the most important tasks for modern experimental particle physics. Should supersymmetry be the correct description of Nature, there is a good chance that the first supersymmetric particles to be observed will be third generation scalar quarks. A number of searches at ATLAS exploit this possibility in order to look for exciting physics beyond the Standard Model. This thesis describes searches for third generation scalar quarks which involve jets coming from heavy flavour quarks. A particular emphasis is put on the data driven estimate of the multijet background and the statistical interpretation of the results.

Chapter 2 gives an overview of the Standard Model of particle physics. The

[1]A proverb in Maltese can be found following each chapter title. Appendix D contains a list of these proverbs, along with a translation into English.

pitfalls of the theory are explained and supersymmetry is proposed as a possible solution. The role of the third generation in a variety of supersymmetry models is also described. The current status of relevant supersymmetry searches is then reviewed. Chapter 3 describes the Large Hadron Collider and the ATLAS detector, explaining how the different components can be used to measure interesting physics quantities. Chapter 4 describes the analysis tools used in this thesis. The chapter includes a description of the object reconstruction used in ATLAS and an outline of the statistical methods used to interpret the results of the analyses.

Chapter 5 outlines a data driven method, called jet smearing, which is used to estimate the multijet background in analyses using data collected in 2011. Chapter 6 describes a search for scalar bottom quarks in the scenario where these are the only supersymmetric particles which can be produced in collisions at the LHC. Chapter 7 introduces a slightly more complicated supersymmetric signal, where the scalar bottom quarks are produced in gluino decay chains. This search is carried out with three inclusive datasets recorded in 2011. In Chapter 8 a search for gluino-mediated scalar top quarks is described, and this search is combined with the gluino-mediated scalar bottom quark search in order to extract an interpretation in the hypothesis of minimal supergravity. This chapter also describes a search for direct scalar top quark production.

Chapter 9 gives a summary of the major results within the thesis and concludes.

Chapter 2

Theory and Motivation

Ebda warda bla xewka

2.1 Introduction

The Standard Model (SM) of particle physics is the most complete mathematical description of nature which exists today. Whilst the first theories date back to Democritus and the Greek Atomists, modern experimental particle physics began at the end of the 19^{th} century when Thomson discovered the electron [12]. The field has come a long way since then and today the Large Hadron Collider at the European Centre for Nuclear Research (CERN) provides us with an experimental setup unrivalled by past efforts and physically many orders of magnitude larger than the Thomson cathode ray experiment.

The predictive precision and explanatory power offered by the Standard Model are testament to what is one of the most successful frameworks designed by humankind. However, it is not the final piece of the puzzle. Despite the accuracy of the SM, there are unresolved issues such as a lack of understanding of gravity at the quantum level and the mysterious nature of dark matter. It is at CERN and the LHC where the limits of the Standard Model are being pushed in order to discover what the solution to these problems could be.

This chapter first gives an overview of the Standard Model and the shortcomings of the theory and then moves on to describe supersymmetry and how this solves some of these difficulties. Further details regarding the Standard Model can be found in [13] and [14]. The treatment of supersymmetry shown here follows that in [15], where the reader can find a deeper mathematical treatment than provided here.

2.2 Standard Model

The Standard Model describes all matter and interactions using point like particles without any spatial extension. These do however carry an internal angular momentum, which is defined mathematically by the spin quantum number. The particles which constitute the matter in the universe all have half-integer spin and are known as fermions. The forces between them are mediated by integer spin particles, called bosons. The concept of symmetry is central to the theory and the various forces in the SM can be derived from the constraints imposed by invariance under local gauge transformations. This means that each force is associated with a symmetry over a redundant degree of freedom in the Lagrangian. Gauge transformations are said to be local when they vary between different points in space time.

2.2.1 Matter

The fermions of the Standard Model are further divided into two categories, depending on whether they interact via the strong nuclear force of quantum chromodynamics

(QCD) or not. Particles which do experience this force are known as quarks and these are always bound into more complex entities called mesons (pairs of quarks) or baryons (triplets of quarks), collectively known as hadrons. All of the quarks in the universe are of the lightest two varieties, the up quark and the down quark, which form the building blocks for protons and neutrons. The second set of fermions are known as leptons and carry only the weak charge and/or electromagnetic charges. Table 2.1 lists the known SM fermions. For each particle in the table, there also exists an anti-particle.

Quarks			Leptons		
Particle	Mass (MeV)	Charge (e)	Particle	Mass (MeV)	Charge (e)
up (u)	1.7-3.1	$\frac{2}{3}$	electron (e)	0.511	-1
down (d)	4.1-5.7	$-\frac{1}{3}$	e neutrino (ν_e)	$< 2 \times 10^{-6}$	0
charm (c)	1290^{+50}_{-110}	$\frac{2}{3}$	muon (μ)	105.7	-1
strange (s)	100^{+30}_{-20}	$-\frac{1}{3}$	μ neutrino (ν_μ)	$< 2 \times 10^{-6}$	0
top (t)	1.73×10^5	$\frac{2}{3}$	tau (τ)	1777	-1
bottom (b)	4190^{+180}_{-60}	$-\frac{1}{3}$	τ neutrino (ν_τ)	$< 2 \times 10^{-6}$	0

Table 2.1: Fermions in the Standard Model. These particles have spin $s = 1/2$. Interactions between these particles are mediated by the gauge bosons shown in Table 2.2.

The SM as it stands today contains three quasi-identical copies of quarks and leptons, differing only in mass. These three copies are known as families or generations. The bulk of ordinary matter is composed of the first generation. This includes the doublet containing the previously mentioned up and down quarks along with the electron and the electron neutrino. The reason for the three-fold repetition of generations is as of yet unknown, so much so, that when the muon was discovered Nobel laureate I. Rabi asked "who ordered that?" [16].

2.2.2 Forces

Mathematically, each of the three forces of the Standard Model is associated with the local symmetry operations of a Lie group. The force mediators are the photon, γ, for electromagnetic interactions, the gluons for strong interactions and the $W^{\pm}$ and Z bosons for weak interactions. Gluons possess colour charge and the $W^{\pm}$ and Z bosons carry weak isospin. Therefore these particles not only mediate the force, but also experience it. This leads to more complex phenomenologies than that found in electromagnetism. The strength of the gravitational force between elementary particles is so tiny in comparison to the other three forces that it can be considered negligible. Table 2.2 lists the SM gauge bosons. We now consider each of the forces individually in more detail.

Force	Vector Boson	Mass (GeV)	Electric Charge (e)
Strong	gluon (g)	0	0
Weak	$W^{\pm}$	80.4	± 1
	Z	91.2	0
Electromagnetism	photon (γ)	0	0

Table 2.2: Vector gauge bosons in the Standard Model. These particles possess integer spin and mediate interactions between the fermions shown in Table 2.1.

Electromagnetic Force

Quantum electrodynamics (QED) is the simplest of the theories that form the SM. It forms the mathematical grounds upon which subsequent, more complex, forces were modelled. QED based on the $U(1)_Q$ Abelian symmetry group and it describes the interaction between charged fermions and the massless photon. The QED electromagnetic Lagrangian, $\mathcal{L}_{EM}$, describing a fermion ψ of mass m is given by Equation 2.1.

$$\mathcal{L}_{EM} = \bar{\psi}(i\not{D}_{QED} - m)\psi - \frac{1}{4}F_{\mu\nu}F^{\mu\nu} \tag{2.1}$$

The covariant derivative $\not{D}_{QED,\mu}$ replaces the usual partial derivative, as shown in Equation 2.2, to maintain the local $U(1)_Q$ gauge invariance. It necessitates the introduction of the photon gauge field.

$$\partial_\mu \rightarrow \not{D}_{QED,\mu} = \partial_\mu + iQA_\mu \tag{2.2}$$

Here Q is the charge of the fermion under consideration and would be e for the electron. The electromagnetic field $F^{\mu\nu}$ is given in terms of the photon field such that $F^{\mu\nu} = \partial^\mu A^\nu - \partial^\nu A^\mu$. The Abelian structure of $U(1)_Q$ does not allow any self-interaction terms for the photon field.

Strong Force

The strong force of QCD is modelled on the electromagnetic force with a very consequential difference, which is that the $SU(3)_C$ colour gauge group is more complex than $U(1)$. In particular, it is non-Abelian. The Lagrangian is given by $\mathcal{L}_{QCD}$, shown in Equation 2.3, and is of a similar form to the QED one.

$$\mathcal{L}_{QCD} = \sum_n \bar{\psi}_n^a (i\gamma^\mu \not{D}_{QCD,\mu} - m_n)\psi_n^a - \frac{1}{4} G_{\mu\nu}^\alpha G_\alpha^{\mu\nu} \tag{2.3}$$

Here the index α runs from 1 to 8, with the gluon field tensor, $G_{\mu\nu}^\alpha$, corresponding to the $F^{\mu\nu}$ in electromagnetism. The index n runs over all the quark flavours (u, d, c, s, t, b) and a labels the colour charge (red, blue, green). The terms $\not{D}_{QCD,\mu}$ and $G_{\mu\nu}^\alpha$ both depend on the gluon gauge field, A_μ^α, as shown in Equation 2.4 and Equation 2.5.

$$\not{D}_{QCD,\mu} = \partial_\mu + ig_s A_\mu^\alpha \lambda_\alpha \tag{2.4}$$

$$G_{\mu\nu}^\alpha = \partial_\mu A_\nu^\alpha - \partial_\nu A_\mu^\alpha - g_s f^{ijk} A_\mu^j A_\nu^k \tag{2.5}$$

The λ_α are the generators of the $SU(3)_C$ group and the f^{ijk} are the non-trivial structure constants of the group:

$$[\lambda_\alpha, \lambda_\beta] = i f^{\gamma}_{\alpha\beta} \lambda_\gamma \tag{2.6}$$

It is this non-Abelian nature which allows for gluon-gluon self-interaction.

An important property of QCD is the fact that the coupling constant g_s decreases as the renormalisation scale μ increases. This variation is dictated by the following differential equation:

$$\mu \frac{\partial g_s(\mu)}{\partial \mu} = -\left(11 - \frac{2n_f}{3}\right) \frac{g_s(\mu)^3}{16\pi^2} + \mathcal{O}(g_s(\mu)^5) \tag{2.7}$$

where the value of n_f is equal to the number of flavours available below a given scale μ. In fact, as $\mu \to \infty$, $g_s \to 0$ logarithmically, an effect known as asymptotic freedom. At high enough energies, when g_s is small, perturbation theory can be applied in computations. Non-perturbative effects manifest themselves at lower energy scales, which is where the theory becomes strongly coupled and perturbation theory ceases to be valid.

Quarks and gluons, which are copiously produced at the LHC, are always confined to colourless bound states, an effect called quark confinement. Individual quarks and gluons are never observed alone. This means that when these coloured particles are produced at the LHC, they are not observed directly but instead can be detected as a stream of collimated hadrons in the final state, often simply called jets.

Weak force and Electroweak Unification

The final force in the Standard Model is the weak force, which is responsible for effects in nature such as nuclear beta decay and initiates the process of hydrogen fusion in stars. By requiring that the Lagrangian describing the interactions of left handed fermion doublets is invariant under $SU(2)_L$ in the space of weak isospin, I, one can obtain the theory of the weak force.

Within the SM, the electromagnetic and weak interactions are two different aspects of a unified electroweak interaction [17, 18, 19] with the gauge group $SU(2)_L \times U(1)_Y$ where the gauge group $U(1)_Y$ is that of weak hypercharge Y. This is connected to $U(1)_Q$ via the definition of Y which is $Y = Q - I_3$, where Q is the electric charge and I_3 is the third component of weak isospin. The electroweak Lagrangian is

$$\mathcal{L}_{EW,f} = \sum_f \bar{\psi}_f i \not{D}_{EW,\mu} \psi_f \tag{2.8}$$

The ψ_f are the chiral matter fields which include the left and right handed quarks and leptons, organised in doublets and singlets under $SU(2)_L$ as listed below. Right handed neutrinos have not been observed in nature and are hence omitted, though they can easily be added as singlets to the SM.

$$\Psi_{leptons} = \begin{pmatrix} \nu_L^e \\ e_L \end{pmatrix}, e_R, \begin{pmatrix} \nu_L^\mu \\ \mu_L \end{pmatrix}, \mu_R, \begin{pmatrix} \nu_L^\tau \\ \tau_L \end{pmatrix}, \tau_R \tag{2.9}$$

$$\Psi_{quarks} = \begin{pmatrix} u_L \\ d_L \end{pmatrix}, u_R, d_R, \begin{pmatrix} c_L \\ s_L \end{pmatrix}, c_R, s_R, \begin{pmatrix} t_L \\ b_L \end{pmatrix}, t_R, b_R \tag{2.10}$$

Maintaining the gauge invariance under $SU(2)_L \times U(1)_Y$ requires the introduction of the B_μ and W_μ^i fields via the covariant derivative:

$$\not{D}_{EW,\mu} = \partial_\mu + ig\frac{Y}{2}B_\mu + ig'\frac{\tau_L^i}{2}W_\mu^i. \tag{2.11}$$

The g and g' are the coupling constants for the $U(1)_Y$ and $SU(2)_L$ forces respectively and the τ_L^i are the generators of the $SU(2)_L$ group. The electroweak gauge fields $W_\mu^\pm, Z_\mu$ and A_μ are then linear combinations of the W_μ^i and B_μ:

$$W_\mu^\pm = \frac{1}{\sqrt{2}}(W_1 \pm iW_2) \tag{2.12}$$

$$Z_\mu = \cos\theta_W W_\mu^3 - \sin\theta_W B_\mu \tag{2.13}$$

$$A_\mu = \sin\theta_W W_\mu^3 - \cos\theta_W B_\mu \tag{2.14}$$

where θ_W is the Weinberg angle and is equal to $\tan(\theta_W) = g/g'$.

2.2.3 Mass and Broken Symmetry

As we have described them, the W and Z bosons in the Standard Model are massless; something which clearly contradicts experiment. In fact, they have a mass of around 80.4 GeV and 91.2 GeV respectively [20]. The most naive way to remedy this is to add gauge boson mass terms by hand in the Lagrangian. However, this destroys the symmetry and results in a non-renormalisable theory with catastrophic divergences. These divergences have been circumvented using the concept of spontaneous symmetry breaking [21, 22, 23]. This can be introduced into a global $U(1)$ symmetry as shown here, with the more complex case of $SU(2) \times U(1)$ touched upon later. Consider first the potential $V(\varphi)$:

$$V(\varphi) = \mu^2 \varphi^\dagger \varphi + \lambda(\varphi^\dagger \varphi)^2 \tag{2.15}$$

$$= \mu^2 |\varphi|^2 + \lambda |\varphi|^4 \tag{2.16}$$

This can be incorporated into a Lagrangian as shown in Equation 2.17. If $\varphi(x)$ is a single complex scalar field, transforming as $\varphi(x) \rightarrow \mathrm{e}^{i\alpha}\varphi(x); \alpha \in \mathcal{R}$, then the Lagrangian has a global $U(1)$ symmetry.

$$\mathcal{L} = (\partial^\mu \varphi^\dagger)(\partial_\mu \varphi) - \mu^2 \varphi^\dagger \varphi - \lambda(\varphi^\dagger \varphi)^2 \tag{2.17}$$

If $\lambda < 0$ then the minimum energy of the potential is not bounded below. This is not a physically feasible option and therefore only $\lambda > 0$ is considered. When $\mu > 0$ the potential has a unique minimum value given by $V_{min} = 0$ at $\varphi = \varphi_0 = 0$. For $\mu^2 < 0$ the minimum lies on a circle given by Equation 2.18.

$$\varphi_0 = \langle 0 | \varphi | 0 \rangle = \sqrt{\frac{-\mu^2}{2\lambda}} e^{i\theta} \tag{2.18}$$

The value of the phase is arbitrary and there are an infinite number of minima, with the physical vacuum state realised being any of these possible states. Once a particular vacuum state is realised the $U(1)$ symmetry is broken. For simplicity, we can take the selected minimum to be real, at $\varphi_0 = \sqrt{-\frac{\mu^2}{2\lambda}} = \frac{\nu}{\sqrt{2}}$ where $\nu = \sqrt{\frac{-\mu^2}{\lambda}}$. One can then introduce two Hermitian fields $\sigma(x)$ and $\eta(x)$ and expand $\varphi(x)$ around

the chosen vacuum expectation value as shown in Equation 2.19:

$$\varphi(x) = \frac{1}{\sqrt{2}}\left[\nu + \sigma(x) + i\eta(x)\right] \tag{2.19}$$

The fields $\sigma(x)$ and $\eta(x)$ must have zero vacuum expectation values. Expanding the Lagrangian in these fields gives the Lagrangian of Equation 2.20:

$$\mathcal{L} = \frac{1}{2}(\partial^\mu\sigma)(\partial_\mu\sigma) - \frac{1}{2}m_\sigma^2\sigma^2 + \frac{1}{2}(\partial^\mu\eta)(\partial_\mu\eta) \tag{2.20}$$

What has happened here is that the σ field has obtained a mass, $m_\sigma^2 = \mu^2/2$, whilst the η field remains massless. Therefore one massive scalar boson and one massless scalar boson have been obtained by introducing two degrees of freedom via the complex scalar field.

What we have described above involved the breaking of a global symmetry. The procedure can be repeated with a local $U(1)$ symmetry, which is the case for electromagnetism, as described in Section 2.2.2. Equation 2.21 shows a Lagrangian where the covariant derivative is used to preserve the local gauge symmetry. The kinetic term is shown explicitly and the same potential as in Equation 2.16 is assumed.

$$\mathcal{L} = -\frac{1}{2}[(\partial^\mu - iQA^\mu)\varphi^\dagger(\partial_\mu + iQA_\mu)\varphi] - \frac{1}{4}F^{\mu\nu}F_{\mu\nu} - V(\varphi) \tag{2.21}$$

Since the symmetry is now local, we can now choose α such that both the vacuum and φ are real:

$$\varphi(x) = v + h(x) \tag{2.22}$$

Substituting this into Equation 2.21, it follows that

$$\mathcal{L} = -\frac{1}{2}\partial^\mu\partial_\mu - \frac{1}{5}4\lambda v^2h^2 - \frac{1}{4}F^{\mu\nu}F_{\mu\nu} - \frac{1}{2}Q^2v^2A^2 + \mathcal{L}_{interactions} \tag{2.23}$$

Before picking the vacuum state we had a complex scalar field φ and a massless vector field, the photon A^μ, with two polarisation states. Following the symmetry breaking we have a single real scalar h with a mass equal to $\sqrt{4\lambda v^2}$ and a field with mass Qv. The force carrying particle has gained a mass, which is precisely what we

wanted.

In the more complicated case of $SU(2)_L \times U(1)_Y$ a similar procedure can be carried out by introducing four new degrees of freedom via a weak isospin doublet of complex scalar fields:

$$\Phi = \begin{pmatrix} \varphi^+ \\ \varphi^0 \end{pmatrix}, \bar{\Phi} = \begin{pmatrix} \bar{\varphi}^0 \\ \bar{\varphi}^- \end{pmatrix} \tag{2.24}$$

An argument analogous to the one outlined above will result in three degrees of freedom being absorbed into the originally massless gauge bosons, leaving one massive real scalar field. To do this a gauge invariant scalar component $\mathcal{L}_D$, of the form shown in Equation 2.25, is added to the electroweak Lagrangian.

$$\mathcal{L}_D = (D_\mu \Phi)^\dagger (D^\mu) - \mu^2 \Phi^\dagger \Phi - \lambda (\Phi^\dagger \Phi)^2 \tag{2.25}$$

For $\mu^2 < 0$, there are again multiple minima and after a single one is realised the Lagrangian contains extra terms, including mass terms for the three weak gauge bosons. The remaining degree of freedom is a massive scalar particle, predicted by the breaking mechanism and called the Higgs boson, H. The masses of the W and Z bosons obey the following relationships:

$$m_{W^\pm} = \frac{1}{2} v g' \tag{2.26}$$

$$m_Z = \frac{v}{2} \sqrt{g'^2 + g^2} \tag{2.27}$$

$$\cos\theta_W = \frac{m_W}{m_Z} \tag{2.28}$$

In the Standard Model one cannot construct singlet terms out of only left-handed and right-handed quarks or leptons, which means that there is no way of giving these particles mass. The Higgs mechanism however also provides a formalism for fermion masses. It allows for mass terms to be written and fermions acquire a mass via Yukawa couplings to the proposed Higgs field. These have the form shown in Equation 2.29.

$$\mathcal{L}_{\text{Yukawa}} = -g_e \bar{\Psi}_L \psi_{dR} \Phi + \text{Hermitian conjugate} \tag{2.29}$$

These terms give leptons masses which are proportional to the vacuum expectation value of the scalar field. The neutrinos are left massless. Observed neutrino oscillations [24, 25, 26, 27] indicate that they have non-zero mass differences and therefore are not massless. Neutrino masses can be incorporated into the theory. However, since they are less than 1 eV, the approximation that they are massless is a reasonable one.

The quark mass eigenstates are not equal to the weak eigenstates and this allows charged weak interactions to involve transitions between the three generations. The mixing matrix for the quarks with charge $-1/3$ is the Cabibbo-Kobayashi-Maskawa (CKM) matrix [28, 29]. The same mixing matrix introduces a single complex phase which violates the combined charge (C) and parity (P) symmetry CP. This was first observed in 1964 [30].

The particles mentioned have all been observed, with Thomson's electron being the first in 1897. The top quark was the last quark to be observed, being discovered at the Tevatron in 1995 [31, 32]. The tau neutrino was the last fermion found. It was discovered by the Direct Observation of the Nu Tau (DONUT) collaboration in 2001 [33]. The Higgs boson discovery was announced recently after both the ATLAS and CMS collaborations at CERN [34, 35] observed very strong evidence for a scalar boson at a mass of 126.5 GeV which has the properties of the Higgs boson.

2.3 Shortcomings of the Standard Model

The Standard Model has produced a large number of predictions which have been experimentally verified. However, it is not without its issues. Astrophysical and cosmological observations such as galaxy velocity dispersion [36] and rotation curves [37] have resulted in the proposal of dark matter [38, 39], which is entirely unaccounted for in the Standard Model. There is also no reason as to why there are three generations of quarks and leptons or why the masses of the different generations should be so drastically different. Unification of the forces is also not achieved within the Standard Model. Another problem is that many phenomena, such as electroweak mixing and CP violation, are determined by free parameters, which have to be fixed by experi-

ment. Finally, the theory contains a potentially disastrous hierarchy problem which will be discussed here.

The Higgs Mass and the Hierarchy problem

The value of the Higgs mass is one of the 19 free parameters of the SM, dependent on the curvature of the scalar potential at the vacuum minimum. The value of the mass receives radiative corrections from Feynman diagrams at higher order than tree level. When computing the mass to second and higher orders, considering radiative corrections via loop diagrams, all particles which couple to the Higgs must be considered. The Higgs-fermion coupling, shown on the left of Figure 2.1, is of the form $-\lambda_f H\bar{f}f$ and one must consider contributions from every loop correction. This leads to a quadratically divergent integral.

Since gravity is not incorporated into the SM, we know that it is an effective field theory, valid only to some cut-off energy Λ_{UV}, above which gravitational effects become important and the theory is no longer valid. One then obtains a Higgs mass as given in Equation 2.30, where m_f is the mass of the fermion in the loop and λ_f the Higgs-fermion coupling.

$$\Delta m_H^2 = \frac{|\lambda_f|^2}{16\pi^2}\left[-2\Lambda_{UV}^2 + 6m_f^2 \ln(\Lambda_{UV}/m_f) + ...\right] \tag{2.30}$$

If we assume new physics to come into play at around the Planck mass, $\approx 10^{18}$ GeV, then we are left with an incredibly large value of m_H, around 10^{34} GeV. Taking into account various contributions from scalars and other particles coupling to the Higgs, one can cancel out the divergent terms by fixing the bare mass very precisely. In order to reproduce the observed W and Z masses, the required tuning is at the level of the twelfth decimal place in the bare Higgs mass.

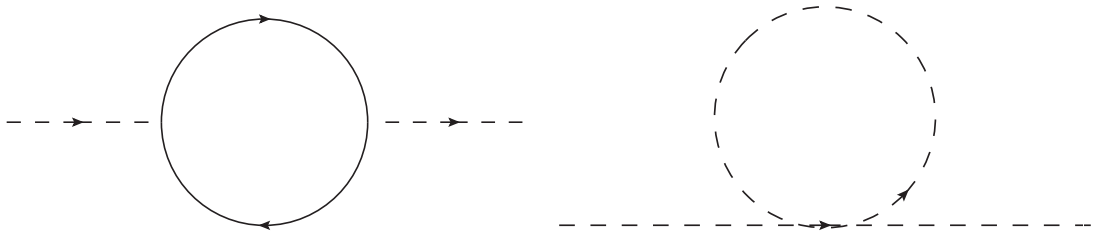

Figure 2.1: Fermion (*left*) and scalar (*right*) Higgs loop diagrams.

2.4 Supersymmetry

Numerous theories exist to solve the issues with the Standard Model and these include large extra dimensions [40], Kaluza Klein models [41] and the focus of this thesis, supersymmetry [42, 43, 44, 45, 46, 47, 48], often referred to as SUSY. All these introduce new physics at around the TeV scale. Supersymmetry extends the Standard Model by hypothesising a symmetry between fermions and bosons whereby each fermion has a scalar boson superpartner and each boson a fermionic superpartner. The superpartners are referred to as "sparticles" and the superpartner of the Standard Model particle p is denoted using a $\tilde{}$, i.e. $\tilde{p}$. If the masses of the additional particles are small enough they allow for the fermionic and scalar Higgs interactions to cancel out. This stabilises the Higgs mass and hence solves the hierarchy problem. Over and above this, supersymmetry also provides a candidate for dark matter as well as a means of unifying the fundamental forces at high energy.

2.4.1 Addressing the Hierarchy Problem

The loop diagram for Higgs coupling to scalar particles, shown on the right in Figure 2.1, contributes the term in Equation 2.31 to the Higgs mass.

$$\Delta m_H^2 = \frac{\lambda_s}{16\pi^2}\left[\Lambda_{UV}^2 - 2m_s^2 \ln(\Lambda_{UV}/m_s) + ...\right] \tag{2.31}$$

Here λ_s is the Higgs to scalar coupling of the particle with mass m_s. The form of the leading terms in Equation 2.31 and Equation 2.30 indicates that, if two scalars existed for each fermion, then the divergent parts of the equation would cancel out. Indeed, if $\lambda_s = |\lambda_f^2|$, then the cancellation would be perfect and letting Λ_{UV} be equal to the Planck mass would result in a Higgs mass of order 100 GeV. Therefore, by introducing extra degrees of freedom, supersymmetry naturally allows for cancellation without any fine tuning. The remnant correction to m_H^2 is then proportional to $|g|^2 m_f^2 \ln(\Lambda_{UV}/m_f)$, where g is a coupling. In order for this correction to be at the electroweak scale the masses of the proposed particles must be less than, or around, 1 TeV.

Supersymmetry has some other beneficial implications. The requirement of a Grand Unified Theory (GUT) adds credence to SUSY. One finds that within the Standard Model, when the running of the coupling constants is extrapolated upwards, they almost meet at around 10^{15} GeV. When one also considers supersymmetry the running couplings are modified in such a way that the agreement is far better [49]. SUSY also solves the problem of dark matter, as described later in Section 2.4.4.

2.4.2 Supersymmetric Transformations

A supersymmetric transformation, S, converts a fermionic state into a bosonic state and vice versa as shown in Equations 2.33 and 2.33.

$$S\,|\text{Boson}\rangle = |\text{Fermion}\rangle \tag{2.32}$$

$$S\,|\text{Fermion}\rangle = |\text{Boson}\rangle \tag{2.33}$$

The single particle states are organized into *supermultiplets* containing the same number of bosonic and fermionic degrees of freedom. They contain corresponding fermion and boson states with equal mass, weak isospin, electric charge and colour degrees of freedom.

Standard model particles and their superpartners fill the supermultiplets. The

quarks and leptons have spin-0 superpartners called squarks and sleptons and denoted $\tilde{q}$ and $\tilde{\ell}$. Spin-$\frac{1}{2}$ superpartners of the gauge bosons are called gauginos. In particular the partner of the gluon is called a gluino, the partner of the $W^{\pm}$ and W^0 are called winos and the partner of the B is called a bino.

The Standard Model particles and their superpartners are shown in Tables 2.3 and 2.4. Superpartners of the Standard Model scalars have larger spin than their counterparts but the superpartners of the fermions and bosons have spin less than their partners. They share equal charge, weak isospin and colour degrees of freedom.

Names		spin-0	$spin - \frac{1}{2}$	$SU(3)_c, SU(2)_L, U)(1)_Y$
squarks, quarks	S	$(\tilde{u}_L, \tilde{d}_L)$	(u_L, d_L)	$(3, 2, \frac{1}{6})$
($\times$ 3 families)	L	$\tilde{u}^*_R$	$\bar{u}^\dagger_R$	$(\bar{3}, 1, -\frac{2}{3})$
	$\bar{d}$	$\tilde{d}^*_R$	$\bar{d}^\dagger_R$	$(\bar{3}, 1, +\frac{1}{3})$
sleptons, leptons	$\bar{L}$	$(\tilde{\nu}, \tilde{e}_L)$	(ν_L, e_L)	$(\bar{1}, 2, -\frac{1}{2})$
($\times$ 3 families)	e	e^*_R	$e^\dagger_R$	$(1, 1, 1)$
Higgs, Higgsinos	H_u	e^*_R	$e^\dagger_R$	$(1, 2, +\frac{1}{2})$
	H_d	e^*_R	$e^\dagger_R$	$(1, 2, -\frac{1}{2})$

Table 2.3: Chiral supermultiplet fields in the MSSM.

Names	spin-$\frac{1}{2}$	spin-1	$SU(3)_c, SU(2)_L, U)(1)_Y$
gluinos, gluons	$\tilde{g}$	g	$(8, 1, 0)$
winos, W bosons	$\tilde{W}^{\pm}, \tilde{W}^0$	$W^{\pm}, W^0$	$(1, 3, 0)$
bino, B boson	$\tilde{B}$	B	$(1, 1, 0)$

Table 2.4: Gauge supermultiplet fields in the MSSM.

In the Standard Model masses can be generated by the Higgs doublet for u-type quarks, with d-type quark masses being generated via the conjugate of the doublet. This cannot be done within supersymmetry, since it results in a non-analytical Lagrangian. Furthermore, supersymmetric models with a non-zero sum of hypercharge contain anomalies. Introducing a single Higgs doublet would result in such a non-zero sum and hence cause further issues. The consequence of this is that two

doublets have to be introduced within supersymmetric theories, with a total of eight degrees of freedom. The eight degrees of freedom are reduced to five when three give masses to the $W^{\pm}$ and Z bosons. The rest form five physical Higgs states denoted $H^{\pm}, A^0, h^0$ and H^0.

2.4.3 Mixing and the MSSM

The simplest possible SUSY model which is consistent with the SM is called the Minimal Supersymmetric Standard Model (MSSM). It postulates the smallest number of new particles. The physically observable mass states are formed from mixing the available supersymmetric states. The neutral MSSM fermions, consisting of the neutral bino, wino and Higgsino ($\tilde{H}_u^0, \tilde{H}_d^0$), mix to form four neutral particles called neutralinos and denoted $\tilde{\chi}_{1,2,3,4}^0$. Two chargino states ($\tilde{\chi}_{1,2}^{\pm}$) are formed from a mix of the charged winos ($\tilde{W}^{\pm}$) and Higgsinos ($\tilde{H}_u^+, \tilde{H}_d^-$). In the squark sector the amount of mixing is proportional to the corresponding standard model partner mass and is hence only non-negligible in the third generation. The stop $\tilde{t}_L$ and $\tilde{t}_R$ mix to form the $\tilde{t}_1$ and $\tilde{t}_2$. Similarly the superpartners of the right and left handed sbottom mix to form the $\tilde{b}_1$ and $\tilde{b}_2$. The same applies to sleptons and only staus are considered to mix significantly, forming the $\tilde{\tau}_1$ and $\tilde{\tau}_2$ from the $\tilde{\tau}_L$ and $\tilde{\tau}_R$. The mixing is summarised in Table 2.5. Further details on the third generation mixing will be provided in Section 2.4.6.

Original States	Mixed States (Mass Eigenstates)	Names
$\tilde{B}^0, \tilde{W}^0, \tilde{H}_u^0, \tilde{H}_d^0$	$\tilde{\chi}_1^0$, $\tilde{\chi}_2^0$, $\tilde{\chi}_3^0, \tilde{\chi}_4^0$	neutralinos
$\tilde{W}^{\pm}, \tilde{H}_u^+, \tilde{H}_d^-$	$\tilde{\chi}_1^{\pm}, \tilde{\chi}_2^{\pm}$	charginos
$(\tilde{t}_L, \tilde{t}_R), (\tilde{b}_L, \tilde{b}_R)$	$(\tilde{t}_1, \tilde{t}_2), (\tilde{b}_1, \tilde{b}_2)$	stops and sbottoms
$(\tilde{\tau}_L, \tilde{\tau}_R)$	$(\tilde{\tau}_1, \tilde{\tau}_2)$	staus

Table 2.5: Mixing in supersymmetry. Neutral winos, binos and Higgsinos mix to form the neutralinos. Charginos are a mix of charged winos and Higgsinos. In the squark sector only the third generation experiences non-negligible mixing.

2.4.4 R-parity

The additional particle content in the MSSM allows for terms in the SUSY Lagrangian which permit the violation of either baryon or lepton number. However, searches looking for such processes have not yet discovered them [50]. The terms themselves cannot be forbidden by allowing baryon number and lepton number to be fundamental symmetries of nature as they are violated by non-perturbative EW effects [51]. Instead, one can circumvent the issue via a new symmetry called "R-parity", defined as follows:

$$R_p = (-1)^{2s+3B+L} \tag{2.34}$$

Here s is the spin, B is the baryon number and L is the lepton number. R-parity is a multiplicative quantum number which is +1 for Standard Model particles and -1 for supersymmetric particles. If R-parity is conserved then the problematic terms are forbidden. This has profound consequences for the search for supersymmetry as discussed in this thesis. A system of colliding protons at the LHC will have an R-parity of +1 and sparticles, which have an R-parity of -1, must be produced in multiples of two. Furthermore, sparticles can only decay into an odd number of sparticles. Therefore the lightest supersymmetric particle (LSP) must be stable in R-parity conserving scenarios. Since such a particle has not been observed, it must also be electrically neutral and weakly interacting. This stable, massive, neutral weakly interacting particle is a perfect dark matter candidate and fits in well with Cold Dark Matter (CDM) models [52]. Such a particle would not interact with the ATLAS detector and therefore would result in substantial missing transverse momentum in an event, a fact which is exploited by the analyses described in later chapters.

2.4.5 Supersymmetry Breaking

If supersymmetry were an exact symmetry, sparticles would have the same masses as their Standard Model partners. However, no sparticles have been observed, so this clearly cannot be the case. Whilst supersymmetry must be broken, the relationships between couplings must also remain unchanged, to ensure that the theory still solves

the hierarchy problem. This is known as soft supersymmetry breaking and the scale, m_{soft}, of the breaking must, at most, be of order 1 TeV.

Supergravity

Supergravity [53] is the name given to gravity mediated SUSY breaking, in which SUSY is broken at a high scale where we have universality of the forces. It is one of the most commonly studied classes of supersymmetry-breaking models, partially due to the fact that the number of parameters can be reduced to a manageable number. The simplest of these models are known as minimum supergravity models (mSUGRA) and in this case $\mathcal{L}_{soft}$ is dependent on just five parameters. There are two mass terms which are the common mass for all scalar particles at the GUT scale (m_0) and the common fermion mass at the same scale ($m_{1/2}$). The masses of the different SUSY fermions denoted M_1 (winos), M_2 (binos) and M_3 (gluinos), are then uniquely determined via the following relation:

$$\frac{M_1}{\frac{5}{3}g'^2} = \frac{M_2}{g^2} = \frac{M_3}{g_s^2} = m_{1/2} \tag{2.35}$$

The value of $\tan\beta$ defines the ratio of the Higgs vacuum expectation values of the two neutral Higgs scalars. Finally there are the common GUT scale trilinear coupling, A_0 and the sign of the Higgs potential parameter, μ. The GUT scale mass parameters are then evolved down to the EW scale using Renormalisation Group Equations to give the different sparticle masses. Despite the seemingly small parameter set there are a vast number of different phenomenologies available within mSUGRA. Due to this, various points in the parameter space have been used as benchmarks for the preparations of various analyses by ATLAS.

2.4.6 Heavy flavour in SUSY

Heavy Flavour in the MSSM

The mixing of the third generation squarks described in Section 2.4.3 is shown in Equation 2.36 for stop quarks and in Equation 2.37 for sbottom quarks.

$$m(\tilde{t})^2 = \begin{pmatrix} m(\tilde{t}_L)^2 & m(t)(A_t - \mu \cot\beta) \\ m(t)(A_t - \mu \cot\beta) & m(\tilde{t}_R)^2 \end{pmatrix} \quad (2.36)$$

$$m(\tilde{b})^2 = \begin{pmatrix} m(\tilde{b}_L)^2 & m(b)(A_b - \mu \cot\beta) \\ m(b)(A_b - \mu \cot\beta) & m(\tilde{b}_R)^2 \end{pmatrix} \quad (2.37)$$

The large top and bottom mass means that mixing between the chiral states of the super-partners of the Standard Model fermions might yield low masses for the lightest scalar bottom and scalar top states ($\tilde{b}_1$ and $\tilde{t}_1$ respectively). The light masses would imply large cross sections and greater accessibility within decay chains starting with gluino-gluino production.

At the LHC, if the gluino is light enough to be produced in 7 TeV proton-proton collisions, the sbottom (stop) quarks are expected to be produced through $\tilde{g} \to \tilde{b}b(\tilde{t}t)$ decays when $m_{\tilde{g}} > m_{\tilde{b}(\tilde{t})} + m_{b(t)}$ (gluino-mediated production). Searches for such production would benefit from the relatively large gluino cross section, which is around 10 pb for a gluino with a mass of 400 GeV. If the gluino is too heavy to be produced, then sbottoms and stops would only be produced via direct sparticle pair production. Feynman diagrams for the two production modes are shown in Figure 2.2. If the gluinos can be produced at the LHC and the sbottom (stop) is the lightest squark but is still heavier than the gluino, then gluinos can decay into bottom (top) quark pairs and a neutralino via an off-shell sbottom (stop) quark as shown below:

$$\tilde{g}_1 \to b\bar{b}\tilde{\chi}_1^0 \quad (2.38)$$

$$\tilde{g}_1 \to t\bar{t}\tilde{\chi}_1^0 \quad (2.39)$$

The production cross section of supersymmetric particles depends almost exclusively

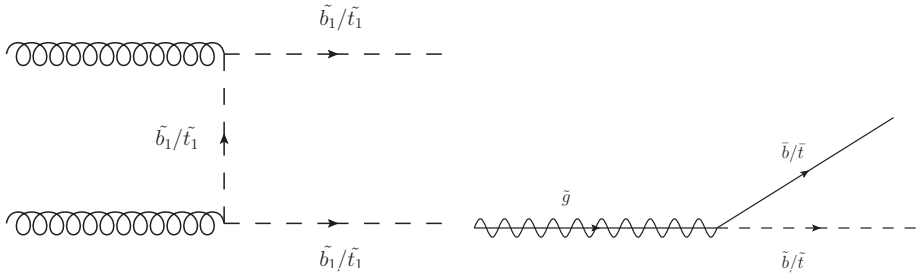

Figure 2.2: If the gluino is accessible at 7 TeV then stops and sbottoms can be produced via gluino decays (*right*). If the gluino is too heavy, stops and sbottoms may be produced in direct pair production (*left*).

on the mass of the particle in question, especially when other sparticle masses are very large. An overview of these cross sections can be seen in Figure 2.3.

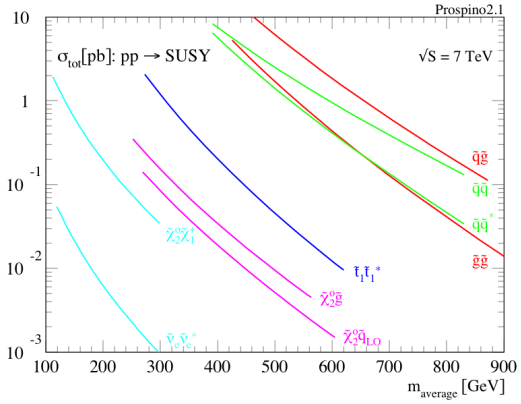

Figure 2.3: The dependence of the sparticle production cross sections on mass at 7 TeV [54].

A variety of different decay modes are possible for stops and sbottoms, and which of these occur depends on the particle spectrum. Throughout this thesis the sleptons and sneutrinos are always assumed to be very heavy and hence decoupled from the stops and sbottoms. Only the simplest sbottom quark decay, where $\tilde{b}_1 \rightarrow b\tilde{\chi}_1^0$, is considered and it is shown in Figure 2.4. A similar decay mode exists for the stop quark, with $\tilde{t} \rightarrow t\tilde{\chi}_1^0$. If $m(\tilde{t}_1) > m(\tilde{\chi}_1^{\pm}) + m(b)$, then the stop can decay via $\tilde{t}_1 \rightarrow \tilde{\chi}_1^{\pm} b$

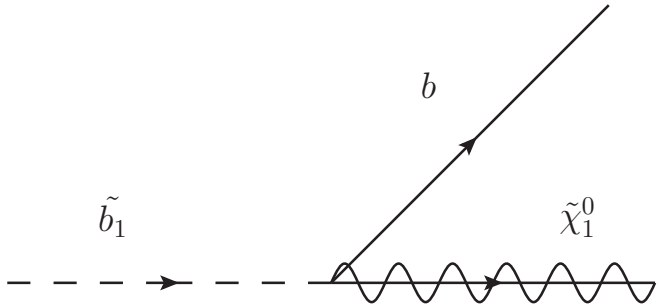

Figure 2.4: Decay mode considered for the sbottom quark where the $\tilde{b}_1$ decays into a $\tilde{\chi}_1^0$ and a b quark.

with subsequent decay of the $\tilde{\chi}_1^\pm$ into $ff'\tilde{\chi}_1^0$. These combinations of production

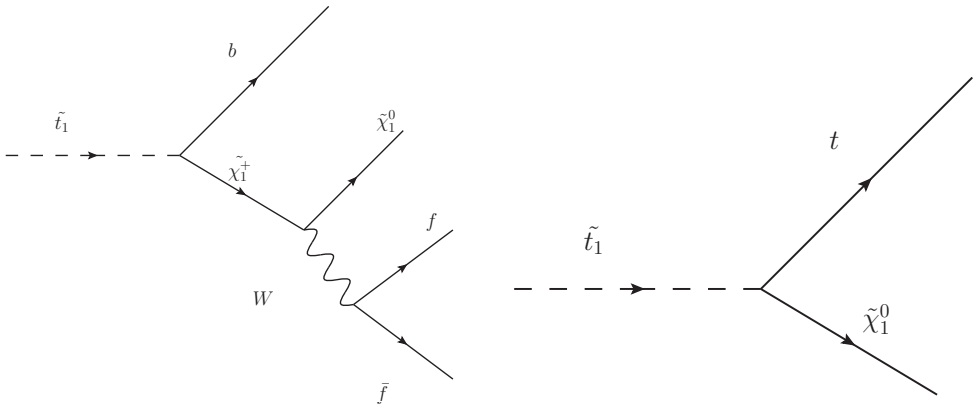

Figure 2.5: The two stop decays considered in this thesis are $\tilde{t}_1 \to \tilde{\chi}_1^\pm b$ (*left*) or $\tilde{t} \to t\tilde{\chi}_1^0$ (*right*).

and decays lead to a variety of final states, involving missing energy and different numbers of jets, ranging from 2 in the direct sbottom pair production up to 12 in gluino mediated stop production.

It will often be the case in this thesis that the mass hierarchy being investigated will be set by hand. This allows us to focus on one or two production processes. Such constructs, which only describe part of the supersymmetric mass spectrum, are called phenomenological MSSM or pMSSM models. The simpler particle spectra and decays also allow for an easier interpretation of analysis results.

Heavy Flavour in Simplified Models

A further generalisation of phenomenological MSSM is the concept of simplified models. The production, decay and the final state signature and kinematics of various supersymmetric scenarios can be approximated using a few well-motivated assumptions [55], almost independently of the exact model. Simplified models are designed to contain a very basic particle spectrum with a single production mode and decay mode. This is far less than a typical model of physics beyond the Standard Model such as minimal supergravity. Furthermore, no assumptions are made on the cross sections of the production mode, allowing results to be generalized to non-SUSY models which share similar kinematics.

Heavy Flavour in mSUGRA

If the squark masses are unified at the GUT scale, the $\tilde{t}_R$ mass is driven down at the EW scale because of the large Yukawa coupling of the top. This in turn reduces the observeable $\tilde{t}_1$ mass. In general, the mass spectrum will depend strongly on the mSUGRA parameters. In particular, large $\tan\beta$ and $A_0 < 0$ scenarios favour large mass splitting between the two mass eigenstates of the third generation squarks. This will be further discussed in Chapter 8.

2.4.7 Current Experimental Bounds from Hadron Colliders

The most recent direct experimental constraints on heavy flavour squarks come from D0 and CDF, the two detectors at the Tevatron $p\bar{p}$ 1.96 TeV collider at Fermilab in Batavia, Illinois.

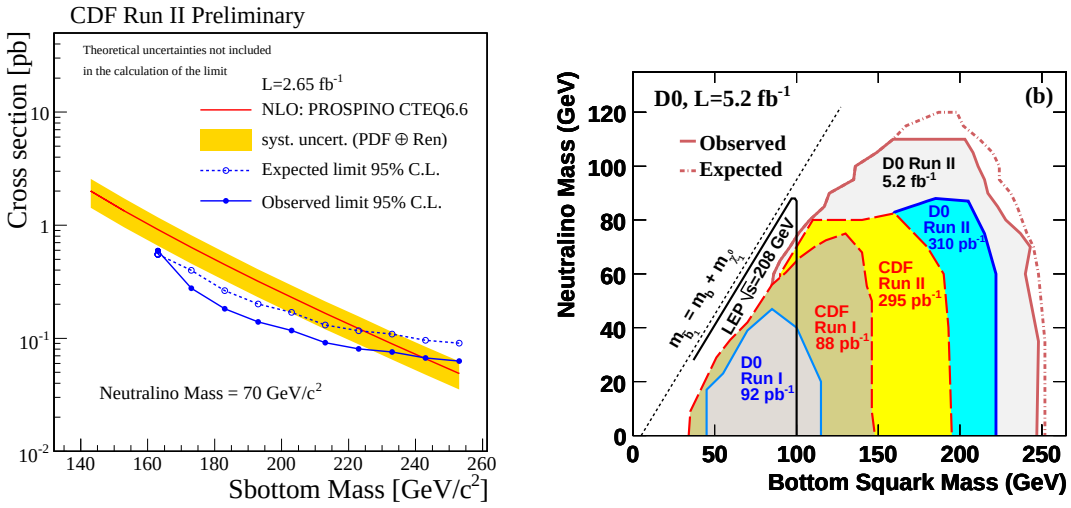

Figure 2.6: Tevatron limits on direct sbottom pair production from CDF [56] (*left*) and D0 [57] (*right*)

Direct Sbottom and Stop Searches

Both Tevatron experiments searched for direct sbottom pair production in $p\bar{p}$ collisions with $\sqrt{s} = 1.96$ TeV at the Tevatron. The CDF detector used 2.65 fb^{-1} of data [56] and looked for events with two energetic jets and large missing transverse energy, assuming that the sbottom quark decays exclusively into a b-quark and a $\tilde{\chi}_1^0$. They did not observe any significant excess and instead set 95% confidence level upper limits on the allowed sbottom and neutralino masses, as shown in Figure 2.6 (left). D0 carried out a similar search using a larger data set size of 5.2 fb^{-1} [57] in the same mass hierarchy scenario. The analysis excluded $m_{\tilde{b_1}} < 247$ GeV for $m_{\tilde{\chi}_1^0} = 0$ GeV and $m_{\tilde{\chi}_1^0} < 100$ GeV for $160 < m_{\tilde{b_1}} < 200$ GeV. The D0 limits are also shown in Figure 2.6 (right).

Limits on direct stop pair production with subsequent $\tilde{t} \to b\tilde{\chi}_1^{\pm}$ decays were set by both experiments, with results depending on the chargino mass and possible branching ratios of the chargino decay. For a chargino mass of 106 GeV, CDF excludes stop masses of 180 GeV (135 GeV) for neutralino masses of 45 GeV (85 GeV) in the most optimistic scenario. D0 excludes stop masses of 130 GeV to 190 GeV for a

chargino mass between 90 and 150 GeV.

Gluino-Mediated Sbottom Searches

CDF searched for gluino-mediated sbottoms in 2.5 fb^{-1} of data [58] using events containing two or more jets and missing transverse energy. The analysis is divided in two, with one selection requiring exclusively one jet coming from a b-quark and the second selection requiring at least two such jets. An optimisation using a Neural Network is also carried out using a number of discriminating variables such as jet transverse energies and angular correlations between the jets and the missing transverse energy. Two optimisations are carried out, geared towards different gluino and sbottom mass hierarchies. No excesses were observed and limits were set in the $(m_{\tilde{g}}, m_{\tilde{b_1}})$ plane. The results from this search are shown in Figure 2.7.

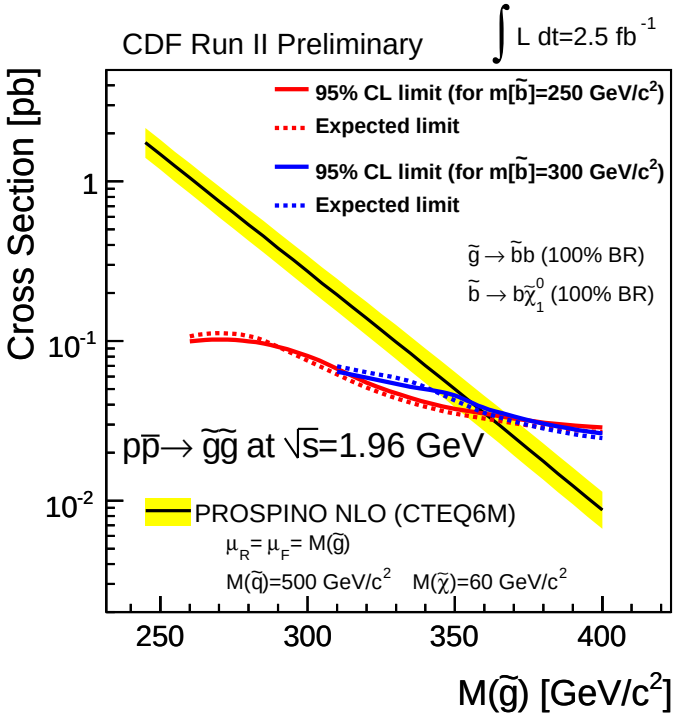

Figure 2.7: Tevatron limits on gluino-mediated sbottom production from CDF [58] .

mSUGRA/CMSSM

Both Tevatron experiments have performed a variety of searches for mSUGRA, exploiting gaugino ($\tilde{\chi}_2^0$ or $\tilde{\chi}_1^\pm$) pair production followed by decays into leptons and neutralinos. Such events have 3 leptons and large missing transverse energy, a signature with very few Standard Model backgrounds.

D0 performed two searches [59], one of which uses τ leptons and another which does not. The latter uses both soft and tight lepton transverse momentum cuts with 2.3 fb^{-1} of data, whilst the former is a softer analysis using 1 fb^{-1} of data. Agreement between the Standard Model expectation and the data is observed in both analyses and 95% confidence level upper limits are constructed as shown in Figure 2.8. CDF carried out a 3.2 fb^{-1} analysis [60] where three lepton events were binned exclusively according to the lepton type (using e and μ only). The fact that the selections are not overlapping allows for an easy statistical combination of the results. Good agreement between the data and the Standard Model expectation is observed and 95% confidence level upper limits are set. Figure 2.8 shows the CDF and D0 limits on mSUGRA.

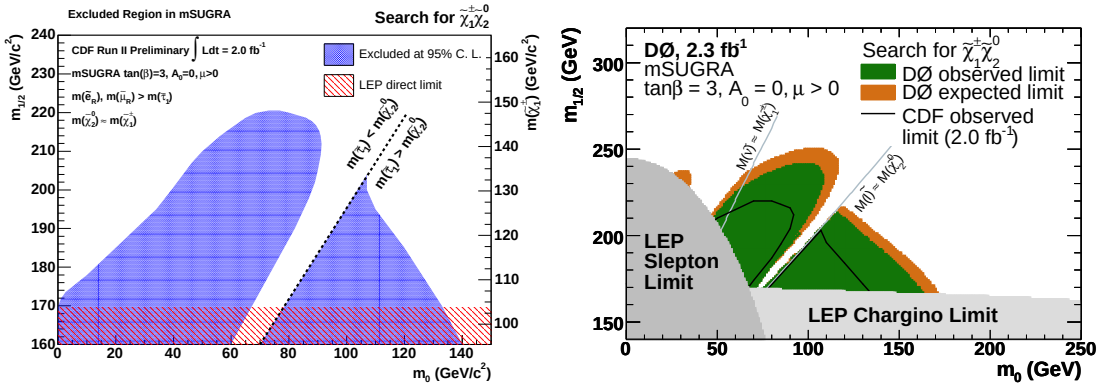

Figure 2.8: Tevatron limits on mSUGRA from D0 [59] (*left*) and CDF [60] (*right*) using lepton searches.

Searches for squarks and gluinos are carried out by CDF [61] and D0 [62] in events with at least 2, 3 or 4 jets and substantial missing transverse energy. CDF uses

2 fb^{-1} of data whilst D0 uses 2.1 fb^{-1} and both experiments observe good agreement between the data and expected SM background, following which they derive the 95% confidence level upper limits shown in Figure 2.9.

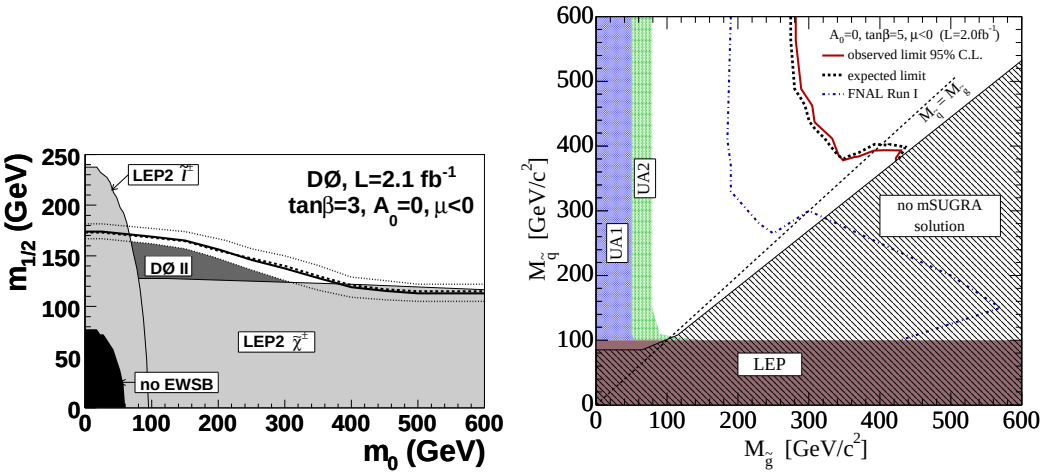

Figure 2.9: Tevatron limits on mSUGRA from D0 [62] (*left*) and CDF [61] (*right*) using jet based searches.

Searches for Supersymmetry at LEP

The mass of the neutralino, which throughout this thesis will always be the lightest supersymmetric particle, has also been constrained by the Large Electron Positron Collider (LEP). The limits [63] on the neutralino mass are indirect, and are derived via limits on chargino production, using the assumption that at the GUT scale the gauge boson masses are unified. Limits on the chargino mass from the four LEP collaborations (ALEPH, DELPHI, L3 and OPAL) are combined to provide a single limit. If slepton masses are very high, which is the scenario considered in the later chapters, then the neutralino mass is bound below at 52 GeV. If the sleptons are allowed to be light then the limit on the neutralino mass drops to 47 GeV.

2.5 Summary

The Standard Model of particle physics has been the cornerstone of fundamental physics for decades. Despite having withstood experimental testing over the years it is not without problems. Supersymmetry solves many of these issues and is considered one of the most promising extensions of the SM. In particular, searches for third generation squarks might prove to be crucial to discovering supersymmetry because of possibly low stop and sbottom masses. Searches for supersymmetry have already been carried out at the Tevatron, but the increased centre of mass energy at the LHC, which will be described in the next chapter, will allow for more powerful and exhaustive searches.

Chapter 3

The ATLAS Detector

L-għodda nofs is-sengħa

3.1 Introduction

Supersymmetry and dark matter can either be discovered at collider experiments or via dark matter searches for Weakly Interacting Massive Particles (WIMPs) at experiments such as DRIFT [64], CDMS [65] and Edelweiss [66]. This thesis focuses on direct searches, utilising the world's most powerful operational collider: the Large Hadron Collider (LHC) [67, 68] at CERN. In particular, data recorded by A Toroidal LHC Apparatus (ATLAS), one of four detectors lying at the collision points around the LHC ring, is used to search for supersymmetric particles. This chapter gives a brief description of the LHC as well as a survey of the ATLAS detector and how its

various components are used to derive precise information about the physics objects produced in collisions.

3.2 The Large Hadron Collider

The Large Hadron Collider is situated on the French-Swiss border, just outside Geneva. It sits in a 27 km long circular tunnel, originally dug out to house the Large Electron-Positr on collider (LEP). It is designed to collide proton beams together at a centre of mass energy of $\sqrt{s} = 14$ TeV. This represents a factor of 7 more energy than the Tevatron at Fermilab. The increased energy means that more energy is available for the production of new particles. The instantaneous luminosity is designed to reach 1.0×10^{34} cm^{-2}s^{-1}, with around 10^{11} protons in each bunch, colliding at a rate of 40 MHz.

The proton beams are focused to collide in four places around the LHC ring, each housing a detector. The largest two, ATLAS [11] and the Compact Muon Solenoid (CMS) [69], are general purpose detectors with diverse physics programmes. The third, the Large Hadron Collider beauty experiment (LHCb) [70] searches for new physics by looking at rare b decays and by making precision measurements of CP violation. Finally, A Large Ion Collider Experiment (ALICE) [71] is a heavy-ion experiment looking at the quark-gluon plasma thought to exist just after the Big Bang.

The LHC accelerator complex is shown in Figure 3.1. The high energy protons are accelerated by a linear accelerator (LINAC) to 1.4 GeV before passing to the Proton Synchroton (PS), which takes the energy up to 25 GeV. Bunches are collected and injected into the Super Proton Synchroton (SPS), increasing the beam energy to 450 GeV over 12 turns. The LHC then uses over 1300 dipole magnets at 8.3 T to ramp up the energy to a maximum of 7 TeV per beam. In order to keep the beam focused, 392 quadropole magnets are used. Various sextupole, octupole and decapole magnets are used to compensate for systematic non-linearities. Table 3.1 summarises some of the technical parameters of the LHC.

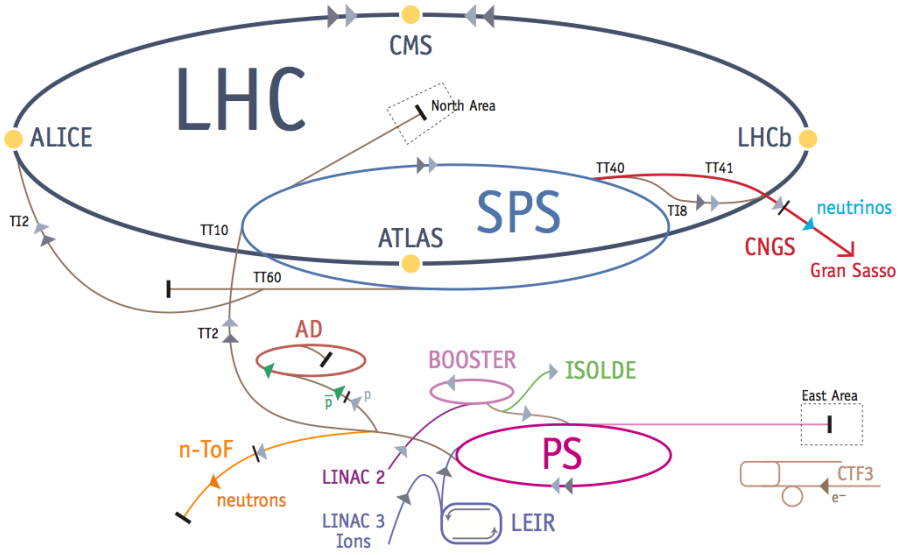

Figure 3.1: A schematic showing the LHC accelerator complex, including a number of older accelerators used to ramp up the energy prior to injection into the LHC. The yellow dots show the four collision points, where the four large detectors are situated. Figure is taken from [72].

Parameter	Value
Energy at collision	7 TeV
Energy at injection	0.45 TeV
Machine circumference	26658.833 m
Dipole field at 7 TeV	8.33 T
Luminosity	10^{34} cm$^{-2}s^{-1}$
RMS Bunch length	7.55 cm
Number of particles per bunch	1.15 $\times 10^{11}$
Number of bunches per beam	2808
Time between bunches at nominal luminosity	25 ns
Circulating beam current	0.1582
Dipole magnet temperature	1.9 K
Number of dipole magnets	$\approx$ 1232
Number of quadrupole magnets	$\approx$ 392
Number of corrector magnets	$\approx$ 5000

Table 3.1: Machine design parameters for the LHC, taken from [68].

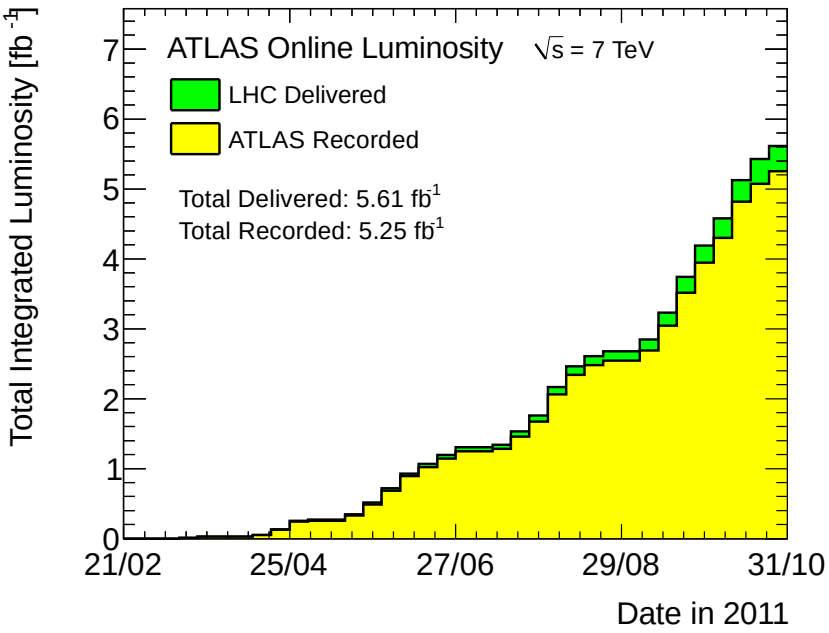

Figure 3.2: Cumulative integrated luminosity delivered to (in green) and recorded by (in yellow) the ATLAS detector during stable beam running at $\sqrt{s} = 7$ TeV in 2011.

The LHC was to start data taking during 2008, however technical issues meant that long term running was postponed up until November 2009, when proton collisions at $\sqrt{s} = 900$ GeV were recorded. In March of 2010, $\sqrt{s} = 7$ TeV collisions were recorded and an integrated luminosity of around 45 pb^{-1} was accumulated by the end of the year, enough to produce many papers across a wide physics spectrum. Figure 3.2 illustrates the data collected up to October 2011, by when ATLAS had collected over 5 fb^{-1} of data. This is the dataset which is used throughout this thesis, though in some sections only a subset of it is used.

3.3 ATLAS

3.3.1 General Physics Goals

An indication of the vast physics programme underway at ATLAS can be obtained from the various sections within the Expected Physics Performance report [73]. The physics chapters of this document include sections on Higgs physics, supersymmetry searches, exotic searches looking for other types of physics beyond the Standard Model, b-physics, top quark physics and other Standard Model physics.

3.3.2 Geometry and Transverse Quantities

A right-handed Cartesian coordinate system is used to describe the ATLAS detector and the particles produced within it. The origin is at the nominal interaction point, the beam defines the z axis and the x-y plane is transverse to it. The positive x direction points towards the centre of the LHC and the positive y-axis points upwards. The azimuthal angle φ is measured around the beam axis and the polar angle θ is the angle from the beam axis. The pseudorapidity, approximately equal to the rapidity[1], is defined as $\eta = -\ln\tan(\theta/2)$. This is widely used instead of θ as differences in η are invariant under Lorentz boosts. The distance ΔR in the $\eta - \varphi$ space is defined as $\Delta R = \sqrt{(\Delta\eta)^2 + (\Delta\varphi)^2}$.

At the LHC, the hard scatter in a collision occurs not between the protons, but between their constitutent partons. These carry an unknown proportion of the total proton momentum and therefore conservation of momentum can only be applied in the plane transverse to the beam axis. For this reason, tranverse quantities such as p_{T} (transverse momentum) are commonly used.

[1]Rapidity is defined as $y = \frac{1}{2}\ln\left[(E + p_z)/(E - p_z)\right]$ and cannot be calculated if the masses of particles are unknown. In the relativistic limit rapidity and pseudo-rapidity are identical.

3.3.3 Detector Overview

The ATLAS detector, shown in Figure 3.3, is 46 m long and 25 m high. It is designed as a series of concentric cylinders around the interaction point where the LHC proton beams collide. It can be divided into four major components which are the magnet systems, the inner detector, the calorimeters and the muon spectrometer. These, along with their various sub-components, are described below.

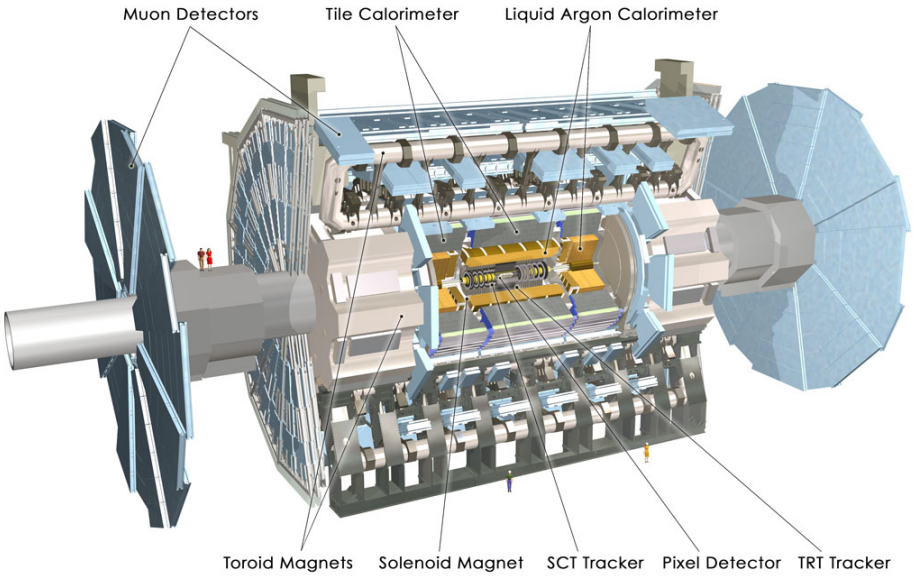

Figure 3.3: A schematic showing the ATLAS detector and its various components. An idea of the scale of the detector can be obtained by comparing it to the size of a human being as illustrated in the figure. Figure taken from [11].

3.4 Magnet System

In order to allow for particle momentum measurement, ATLAS houses two magnet systems. The first is a central solenoid which surrounds the inner detector and the second is a toroid system which generates the magnetic field for the muon spectrometer. The entire system weighs 1300 tonnes and operates at a temperature of 4.8 K,

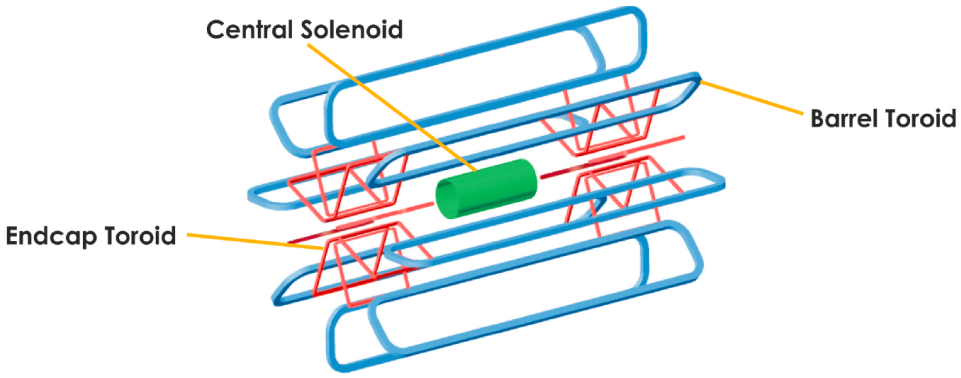

Figure 3.4: Geometry of the ATLAS magnet configurations [74].

storing over 1 GJ of energy when running. The magnet configurations are shown in Figure 3.4.

The ATLAS toroid system consists of three toroids, each with eight coils, radially assembled around the beam axis. The barrel part of the toroid is 25 m long and 5 m wide, whilst the endcap components are around 5 m long, with a 22.5 degree rotation. The barrel system dominates up to $|\eta| < 1$ and the endcaps take precedence for $1.4 < |\eta| < 2$. The intermediate region uses a superposition of the two fields. The toroid system has an average field of around 0.6 T and allows for the momentum measurement of muons with a p_T of up to 6 TeV.

The central solenoid lies outside the inner detector and is extremely thin, at just 45 mm, in order not to obstruct the calorimeters, which lie just outside it. It is 5.3 m long and 2.5 m in diameter, providing a magnetic field of 2 T along the beam axis and allowing for the measurement of charged particles with a p_T of up to 100 GeV.

3.5 Inner Detector

The inner detector (ID) is cylindrical in shape and is 7 m long, extending radially from 50 mm away from the beam pipe to 1.15 m away. It lies immersed in the ATLAS 2 T

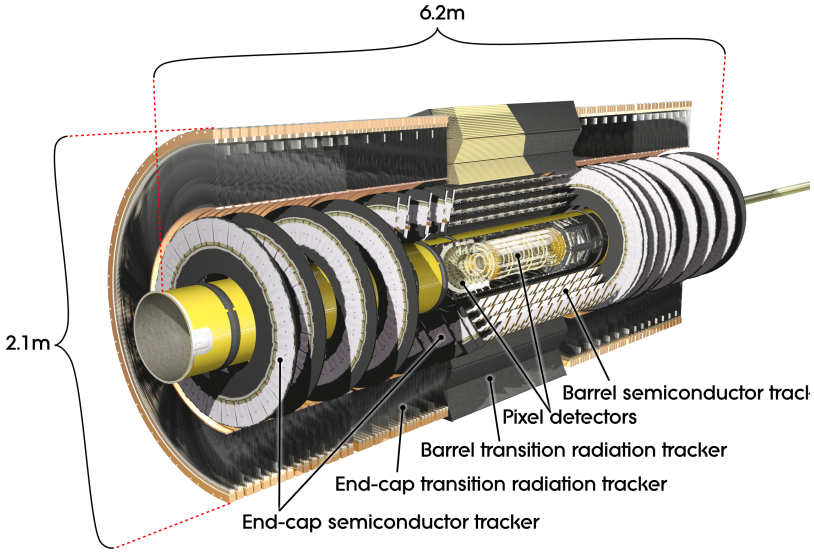

Figure 3.5: A schematic showing the Inner Detector, taken from [11].

solenoid field. A schematic showing the various sub-components is shown in Figure 3.5. Its purpose is to reconstruct charged particle tracks and vertices originating from, or near, the interaction point. The tracks can subsequently be used to measure charges and momenta for the various particles passing through the detector. The highest granularity can be found closest to the beam pipe, where particle track density is highest. Further away, where particle occupancy is lower, a coarser granularity is enough. The innermost region uses discrete, high resolution semiconductor pixel and strip detectors for effective tracking and vertex positioning measurements. These are called the Pixel Detector and Semiconductor Tracker (SCT) respectively. Surrounding these components is a system called the Transition Radiation Tracker (TRT).

3.5.1 Pixel Detector

The pixel detector comprises 80 million readout channels and it is crucial to the resolution of secondary vertices, thereby making this part of the detector of vital importance to the identification of jets originating from b-quarks, called b-jets. Due to their long lifetime, B-mesons travel a measurable distance away from the collision

point before they decay. When travelling at almost the speed of light, this distance is around 500 μm. Identifying the point where the B-meson decays, called the secondary vertex, plays a big part in the selection, or "tagging" of b-jets.

The pixel detector consists of 3 barrels and 6 disks, with 3 per side. The barrel contains approximately 1500 identical modules which measure 62.4 mm $\times$ 22.4 mm. Around a further 1000 can be found in each of the disks, arranged in 16 mm $\times$ 60 mm arrays. The disks lie between 9 cm and 12 cm from the beam whereas the barrel layers lie at average radii of 5 cm, 9 cm and 12 cm. The innermost layer is called the b-Layer and is the most important for the identication of b-jets.

3.5.2 Semiconductor Tracker

At the radii where the Semiconductor Tracker is situated (299 mm - 514 mm away from the beam pipe) particle densities are reduced sufficiently to allow for the use of strip detectors. The SCT is made of modules, each of which is constructed using two planes of silicon strip detectors. Each silicon detector has an area of 6.36 $\times$ 6.4 cm^2 and 768 readout strips. The SCT has 4 coaxial cylindrical barrels and 2 endcap components, the latter each having 9 disks, providing an η coverage up to 2.5. The detector contributes to the measurement of track momenta, impact parameter measurements and vertex positioning. A total of 8 precision measurements can be made per track. The spatial resolution of the silicon detectors allows for a track separation of 200 μm.

3.5.3 Transition Radiation Tracker

The ATLAS Transition Radiation Tracker provides on average 32 hits, with a maximum of 36, in $(R\varphi, z)$ space. This can be used in combination with the other trackers to construct robust pattern recognition and track finding algorithms. The barrel component ($|\eta| < 0.7$) contains 50,000 straw-tubes arranged in 73 straw planes that lie parallel to the beam axis. In the end-caps, covering up to $|\eta| < 2$, 160 straw planes

are assembled. As ionising particles traverse the tube, they release electrons which drift towards the wire. The electron drift avalanches in the high electric field close to the wire and this helps amplify the signal. The constant drift velocity within the wires means that the point where the incident particle traversed can be calculated.

As ionising particles pass through the TRT, which does not have a homogeneous refractive index, they emit radiation along their tracks. This transition radiation deposited in the TRT supplements energy from ionisation losses. Electronics sensitive to two thresholds is used to distinguish between prompt electrons and minimally ionising particles such as pions. The low threshold, at around 250 eV, detects charge liberated by ionising particles. A 5 keV threshold detects higher charges, produced by transition radiation photons. For a given energy, electrons have a much higher Lorentz gamma factor than pions and hence emit more transition radiation. Therefore, the fraction of total hits in a track passing the high threshold is a powerful variable for discriminating between electrons and pions.

3.6 Calorimetry

The ATLAS calorimeters, shown in Figure 3.6, allow for precise measurement of the energies of charged and neutral particles within the entire φ range and up to $|\eta| < 4.9$. This is absolutely crucial as it allows all particles with significant transverse momentum to be measured. This in turn means that solid estimates of the missing transverse energy can be calculated. Both electromagnetic (EM) and hadronic calorimeters are used.

Electrons and photons incident on matter create cascades of particles from bremsstrahlung ($e \to e\gamma$) or pair production ($\gamma \to ee$). They have a narrow transverse profile and can be characterised by their radiation length X_0. Hadrons behave slightly differently and the interactions between them and dense materials produce cascades with particle multiplication via successive inelastic hadron-nuclear interactions. This leads to wider transverse spreads and nuclear interaction lengths an order of magnitude greater than X_0. The calorimeters are sampling calorimeters with alter-

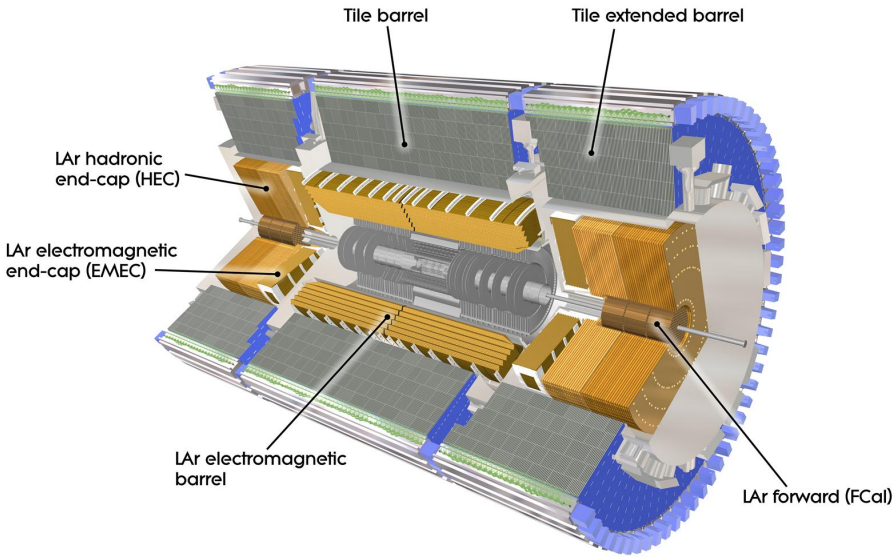

Figure 3.6: The ATLAS calorimeter system, taken from [11].

nating layers of absorbing material and active medium. The absorbing material has to provide enough stopping power to ensure that the showers from incident particles are contained within the calorimeter volume, where they can be measured.

The system consists of three subsystems which correspond to the electromagnetic calorimeter, the hadronic calorimeter and the forward calorimeter. The Liquid Argon (LAr) electromagnetic barrel and electromagnetic endcap calorimeter (EMEC) are closest to the beam pipe and cover an η range of $|\eta| < 3.2$. The hadronic calorimeter also comprises barrel (TileCal) and endcap (HEC) components and extends up to $|\eta| < 3.2$. The extreme forward range ($3.1 < |\eta| < 4.9$) is covered by the forward calorimeter (FCal) which combines electromagnetic and hadronic measurements and is designed to withstand the higher radiation flux expected in this regime.

3.6.1 Electromagnetic Calorimetry

The electromagnetic calorimeter uses lead as a passive absorber and liquid argon as an active medium. The barrel electromagnetic calorimeter is contained within a cryostat system surrounding the entire inner detector cavity. A pre-sampler is placed in front of the main electromagnetic calorimeter (in the region $|\eta| < 1.8$), to correct for energy lost in the material before the calorimeter. The ID structure limits the range for precision physics with electrons to $|\eta| < 2.5$ and it is within this region that the calorimeter granularity is best, with a coarser granularity up to $|\eta| < 3.2$. Full symmetry in φ is guaranteed by using an accordion structure for the calorimeters. There are however gaps in η, in the region of transition between the barrel and the end-cap. Early analyses of ATLAS data ignored electrons and photons within this region for physics purposes. Within $|\eta| < 2.5$ there are three layers of absorber-active medium. The first layer is a strip layer $6X_0$ thick which acts as a pre-shower detector used for particle identification and η positioning. The second layer is transversely segmented into square towers in $\eta - \varphi$ space with size $\Delta\eta \times \Delta\varphi = 0.025 \times 0.025$. The total thickness up to the end of the second sampling layer is $24X_0$. Finally, the "back layer" is coarser in η and has varying thickness ranging between $2X_0$ and $12X_0$.

3.6.2 Hadronic Calorimetry

The bulk of the hadronic calorimeter consists of a scintillator tile calorimeter which is divided into barrel ($|\eta| < 1$) and extended barrel ($0.8 < |\eta| < 1.7$) components. Iron plates are used as absorbers and plastic scintillator plates called tiles are used as active material. The 3 mm thick tiles are placed in a staggered fashion to avoid gaps. Particles coming out of the absorbers produce flashes in the scintillator with wavelength shifting fibres transporting the light to photo-multiplier tubes. These transform the light into a signal proportional to the energy sampled. Inter TileCal scintillators (ITC) are used in the gap between the barrel and extended barrel. The three layers of the tile calorimeter represent $9.7\lambda_{int}$ at $|\eta| = 0$ and this is sufficient to shield the muon system from hadronic punch through. The hadronic endcap calorime-

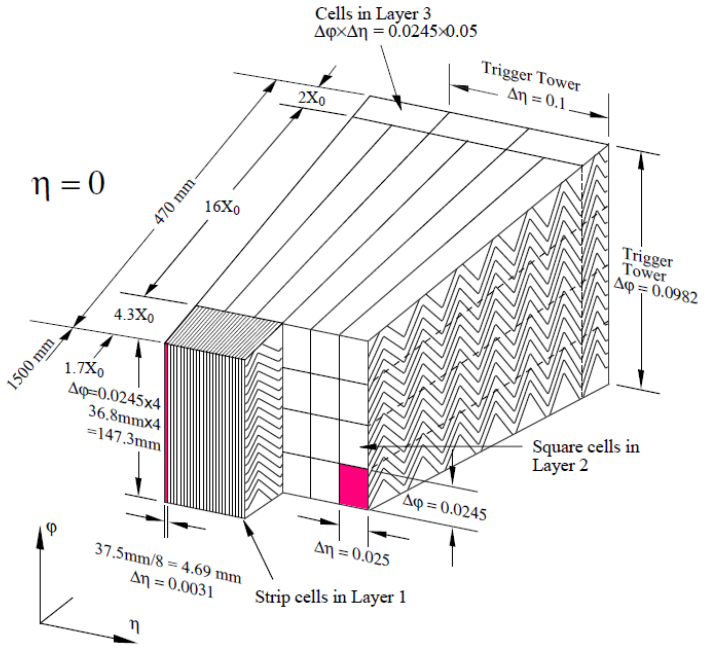

Figure 3.7: Sketch of an electromagnetic calorimeter barrel module [11]. The granularity in η and φ of the cells in each of the three layers is indicated.

ter uses copper absorbers and liquid argon as an active medium. The HEC consists of two wheels on either side of the detector, each having 32 modules arranged into 4 sampling layers. It covers the range $1.5 < |\eta| < 3.2$.

3.6.3 Forward Calorimetry

The forward calorimeter is placed in the extreme forward region ($3.1 < |\eta| < 4.9$) where particle flux is highest. The design of the FCal is thus suited to deal with high radiation densities. Liquid argon is used as the active material. The first of three compartments uses copper which dissipates the heat produced very quickly. This is optimised for electromagnetic energy measurements. The other two compartments use tungsten, which has a high absorption length, and is intended for hadronic calorimetry.

3.6.4 Jet Energy Measurement

The resolution of jet energy measurement can be described using the function shown in Equation 3.1.

$$\frac{\sigma_E}{E} = \sqrt{\frac{a^2}{E} + \frac{b^2}{E^2} + c} \tag{3.1}$$

Here a is the stochastic term and is around 60% $\mathrm{GeV}^{1/2}$ and c a constant term expected to be around 3%. The noise term b is expected to vary between 0.5 and 1.5 GeV. Below 100 GeV in energy the stochastic and noise terms are the dominant ones.

3.7 Muon System

The muon spectrometer (MS) is designed to provide stand-alone triggering and momentum measurement of muons over all φ and a wide range of p_{T} and η. A strong magnetic field over long distances is thus required and this is provided by the toroids. In the barrel region the muon chambers are arranged in three cylindrical layers around the beam axis, called stations. In the intermediate and end-cap regions the chambers are installed vertically. Monitored Drift Tubes (MDT) give precision measurements of track coordinates in the principal bending direction of the magnetic field. Large values of η and points close to the interaction point are covered using Cathode Strip Chambers, which are better equipped to deal with the increased occupancy and radiation. Resistive Plate Chambers (RPCs) and Thin Gap Chambers (TGCs) are used for triggering in the barrel and end-caps respectively.

Muons which have an energy on the order of 100 GeV are measured using a statistical combination of the information coming from the inner detector and the muon spectrometer. Very energetic muons can only be marginally bent within the physically small inner detector and therefore the muon system alone is used. The system is capable of measuring the p_{T} of 1 TeV muons with a precision of less than 10 %.

3.8 Trigger System

At design luminosity the ATLAS detector will observe 40 million collisions per second. In addition to the primary collision, an additional 23 pile-up events are expected to occur per collision. A sequence of trigger levels will reduce the collision rate of almost 1 GHz to a more manageable 100 Hz, minimising the number of interesting events which are rejected. This is extremely challenging as the most interesting physics processes, in particular the ones we have not observed yet, are expected to have the smallest cross sections and branching ratios.

The trigger consists of three sequential layers, which progressively filter out events, making use of increasing information at each step. A schematic of the system is shown in Figure 3.8. The allowed time to process an event increases with trigger level, as less events need to be considered at each successive stage. The first level, L1, is a hardware based trigger built with fast custom electronics. It is capable of making a decision in under 2.5 μs, utilising coarse calorimeter and muon information to identify high p_T objects such as jets, muons, electrons, photons and large missing transverse momentum. It also identifies possible Regions of Interest (ROI) in the detector for the second level, L2, to look at in more detail.

The High Level Trigger, which comprises both the L2 and the Event Filter (EF), consists of farms of commodity processors connected by fast dedicated networks (Gigabit and 10 Gigabit Ethernet). The L2 selection is based on fast custom algorithms processing partial event data within the ROIs identified by L1, thereby reducing the required data volume to take a decision to 2-6% of the total. The L2 output rate is around 1 kHz. Finally the EF trigger makes the decision whether to store the event permanently or not. It is software based and uses the entire event information at a level of detail close to that of the reconstruction level, which will be described in detail in Chapter 4.

When a class of events is produced extremely often it is unfeasible and impractical to record every single one. In this case the trigger is often *prescaled* and only a fraction of the events passing it are retained. A trigger item with a prescale of 10

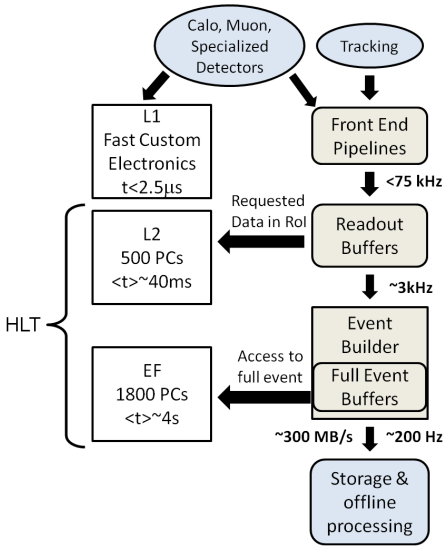

Figure 3.8: A schematic of the ATLAS trigger system, taken from [75].

will only record one in 10 of the events which would pass the normal requirements of the trigger.

The trigger naming convention in ATLAS specifies some of the details of the trigger chain. As an example we can consider a single jet trigger, `EF_jZ_a4tc_EFFS`. The term `_a4tc` reflects the fact that the anti-k_t algorithm is used with topo clusters. The extension `_EFFS` stands for Event Filter Full-Scan, as the entire event information is used and not just a particular ROI. The value of `Z` shows the value of the EF cut on the leading jet p_{T}. A similar naming convention applies to the L1 and L2 components of the trigger, which in this case would be `L1_jX` and `L2_jY`, where `X` and `Y` indicate the p_{T} thresholds on the leading jet at L1 and L2 respectively.

3.9 Summary

The LHC, which is the most powerful collider in the world, has provided around 5 fb^{-1} of 7 TeV proton-proton collisions to the ATLAS detector in 2011. The detector, by means of its various components, is capable of detecting a wide variety of physics

objects which are crucial to the hunt for supersymmetry.

Chapter 4

Analysis Tools

L-ilma fil-bir ma jaqtax għatx

4.1 Introduction

This section discusses the tools which are used to go from raw detector signals within ATLAS to physics results. In particular, a description of how data is turned into physics objects will be provided, along with an explanation of how this process is simulated using Monte Carlo event generation. The systematic uncertainties associated with Monte Carlo generation will be discussed briefly. A summary of the event variables which are useful will also be given. Finally, a description of the statistical framework used to interpret the results is provided.

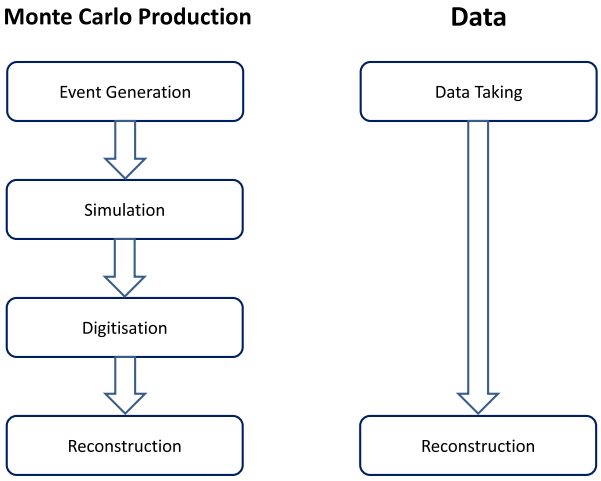

Figure 4.1: The steps used for the production of MC (*left*) and data (*right*) samples at ATLAS.

4.2 Monte Carlo Production

The generation of Monte Carlo (MC) samples has a well-defined structure which goes through a sequence of steps within the ATLAS computing system. A number of these are the same as those applied to raw data recorded by the detector. These steps are shown in Figure 4.1 and are described in the following sections.

Event Generation

The production of Monte Carlo samples begins with the generation of particle four-vectors, usually coming from a specific physics process. A number of generators exist for each possible Standard Model and supersymmetric process. Of particular importance are the `PYTHIA` [76], `ALPGEN` [77] and `MC@NLO` [78] generators for Standard Model processes and the `ISAJET` [79], `MadGraph` [80] and `SUSYHIT` [81] generators for supersymmetric ones. `HERWIG` [82] is used to generate both signal and background samples. The cross sections for these processes are either obtained via the generator

itself or some dedicated cross section calculation program such as PROSPINO [83], which calculates the cross sections for supersymmetric particles. Often the data is used to normalise the amount of expected background, in which case a cross section is not required for the final result.

Monte Carlo generators such as PYTHIA simulate the hard scattering, as well as soft and collinear radiation, but are ill-equipped to handle hard QCD radiation resulting in additional jets. The same holds true for HERWIG, which is interfaced with JIMMY [84] to provide the parton shower component. PYTHIA is used to simulate multijet production throughout this thesis. Matrix element generators, like ALPGEN, compute the exact process with additional hard radiation to a fixed order, usually Leading Order (LO). They can accurately model events with large jet multiplicities but need to be interfaced with a parton shower algorithm to correctly handle the jet structure and soft radiation. Next to Leading Order (NLO) generators, like MC@NLO, generate events with correct NLO normalisation and describe the hardest emission well. Soft and collinear jets need to be produced via a parton shower. In this thesis, vector boson production in association with additional jets is simulated using ALPGEN and top pair production is simulated using MC@NLO or ALPGEN.

Simulation

A GEANT4 simulation [85] calculates where each particle interacts with the detector and how much energy it deposits as it passes through. It includes a complete treatment of all the interactions with the various detector components and magnetic fields. A typical event takes around 10 minutes to simulate [86].

Digitisation

The various interactions, or hits, from the simulation step are then subject to the detector response to produce digits such as times and voltages. These are then recorded, mimicking the process a real particle in the ATLAS detector would undergo.

Object Reconstruction

Finally the digits are reconstructed into physics objects using a number of dedicated algorithms specific to the various objects which pass through the detector. This step is common to real data and Monte Carlo generated events. Further details regarding the reconstruction of different types of objects is given in Section 4.4. Once reconstructed, an event is recorded on tape in what is known as Event Summary Data (ESD) format, taking up approximately 500 kb. This is filtered down to a more manageable Analysis Object Data (AOD) which takes up around 100 kb. Different groups within ATLAS then construct Derived Physics Data (DPD) from AODs, retaining the information required for their particular analyses.

Fast Simulation

ATLFAST-II is a simulation package developed by ATLAS which is substantially faster than the standard simulation procedure. The standard ATLAS reconstruction is used but the overall generation time is significantly reduced by simplifying the calorimeter [87] and tracking [88] simulation. Instead of simulating electromagnetic showers, which take up 75% of the simulation time, truth particles coming out of the inner tracking volume are passed through a parametrisation of the shower energy profiles, which is fed directly into the calorimeter cells. The reduction in the required computational time is of $\mathcal{O}(10)$.

Comparisons of Data to Monte Carlo

Ensuring that the reconstruction algorithms are functioning properly and that Monte Carlo samples describe the data accurately is of paramount importance to any SUSY analysis. Appendix A describes a very first look at LHC data taken in 2010 [89], focusing on a kinematic regime relevant to searches for supersymmetry using jets coming from heavy flavour quarks. The results indicate a good understanding of the detector, which is crucial to the searches described in the rest of the thesis.

4.3 Full Chain Testing

The simulation and reconstruction software is integrated into the ATHENA [90] framework used by ATLAS. The Full Chain Testing (FCT) software is a system which tests each of the stages in the ATLAS production system. It runs every night on a number of small samples ($\approx$ 10 events), going from event generation to reconstruction for a variety of physics processes. Any software problems which are identified can then be rectified without interrupting the full production. To ensure that the entire chain, including the dozens of reconstruction algorithms, is tested, a variety of samples are used. These include Higgs production, Z boson production and minimum bias production. A slightly larger sample ($\approx$ 1000 events) of top pair production is also run. The testing runs on nightly queues at CERN and the author of this thesis was involved in maintaining the testing framework as part of his service work required to become an ATLAS author.

4.4 The Reconstruction Stage

A concise description of the reconstruction methods, employed to derive the various physical objects used throughout this thesis, is given here. These algorithms are applied to both the data and events generated using Monte Carlo.

4.4.1 Jets

Jets are reconstructed using a sequential recombination algorithm. Clusters of energy in the calorimeters, called TopoClusters, are used as input. The distance metric, d_{ij}, between any two TopoClusters i and j is defined as:

$$d_{ij} = \min(p_{Ti}^{2k}, p_{Tj}^{2k}) \frac{\Delta R_{ij}^2}{R_s^2} \tag{4.1}$$

where R_s sets the scale of the radii of the jets and k determines the relative importance of the distance and momentum scales. To reconstruct the jets in an event, an ordered list of all the distances and p_{Ti}^{2k} is constructed. If the smallest item is a pair with distance d_{ij} then the jets i and j are combined to form a single pseudo-particle. If the smallest item is a p_{Ti}^{2k} then i is labelled a jet and removed from the list. The procedure goes on until the list is empty. The jets used in the analyses described in this thesis are reconstructed with $k = -1$, which is called the anti-k_T recombination algorithm [91]. The value of R is set to$R = 0.4$. Unless otherwise stated, jets in this thesis are always contained within $|\eta| < 2.8$ and have a p_{T} of at least 20 GeV.

The clustering and initial jet reconstruction is performed at the electromagnetic scale. The transverse momenta of the jets are then corrected as a function of jet p_{T} and η [92] to account for the difference in response between hadrons and electrons in the detector. This is known as the Jet Energy Scale (JES) correction.

4.4.2 Electrons

The reconstruction of an electron is based on a track in the inner detector and an energy deposit in the calorimeter. Clusters are formed in the EM calorimeter using a sliding window algorithm [93] which looks for seeds by moving a window in $\eta - \varphi$ space across the calorimeter. Seeds are then used to form clusters which are matched to an ID track. A series of cleaning cuts are used to retain real electrons only. The variables used include the amount of hadronic leakage and the shower shapes in the EM calorimeter. The matched track must also point towards the primary vertex and must have at least some minimum number of hits in the pixel and SCT detectors.

4.4.3 Muons

Muons pass throughout the entire ATLAS detector, leaving a track in the inner detector, small energy deposits in the calorimeters and a track in the muon spectrometer. The first stage of muon reconstruction is finding a track within the muon spectrom-

eter, constructed using segments in the separate muon spectrometer modules. This is done using segment pattern recognition and track tracing throughout the toroidal magnetic field. These tracks are extrapolated back towards the interaction point, taking into account energy loss and multiple scattering. For muons with $p_{\mathrm{T}} < 100$ GeV the track in the muon spectrometer is matched to and combined with a track in the inner detector.

4.4.4 Overlapping Objects

When jets, electrons and muons passing the object selection overlap with each other, a classification is required to remove all but one of them. The following scheme is applied throughout this thesis:

1 If an electron and a jet are found within $\Delta R < 0.2$, the object is interpreted as an electron and the overlapping 'jet' is ignored.

2 If a muon and a jet are found within $\Delta R < 0.4$, the object is treated as a jet and the muon is ignored.

3 If an electron and a jet are found within $0.2 \leq \Delta R < 0.4$, the object is interpreted as a jet and the nearby 'electron' is ignored.

4.4.5 Missing Transverse Energy

The transverse component of the missing energy in an event, or $E_{\mathrm{T}}^{\mathrm{miss}}$, is a crucial variable in R-parity conserving SUSY scenarios. The precise definition of the variable changed over the first few years of data taking, as a greater understanding of the detector allowed for more complex formulations. In the bulk of the analysis the two vectorial components of the missing transverse energy are constructed as shown below:

$$E_{x(y)}^{Miss} = -\sum_{electrons} p_{x(y)}^{electron} - \sum_{jets} p_{x(y)}^{jet} - \sum_{muons} p_{x(y)}^{muon} - \sum_{CellOut} p_{x(y)}^{CellOut} \tag{4.2}$$

Jets with the standard calibration, but extending up to $|\eta| < 4.5$, are considered along with electrons and muons. The remaining calorimeter clusters, not belonging to any high p_{T} objects, are included in the `CellOut` term. During the very early periods of data taking a simpler form of $E_{\mathrm{T}}^{\mathrm{miss}}$ was used, which takes into account the missing energy as defined by the topological clusters in the calorimeter. The value of the transverse missing energy is given by the quadratic sum of the x and y components:

$$E_{\mathrm{T}}^{\mathrm{miss}} = \sqrt{(E_x^{Miss})^2 + (E_y^{Miss})^2} \tag{4.3}$$

4.4.6 b-Jets

Jets originating from b-quarks are identified by tagging algorithms which make use of the special properties of B-hadrons. Three taggers, of increasing sophistication, were used in the analyses described in this thesis. A jet is selected a b-jet if it possesses a weight, which is an output of the tagging algorithm, greater than some pre-defined threshold. The value of the threshold results in a trade off between efficiency in selecting true b-quarks and the probability of incorrectly tagging a light quark as a b-jet (called a mistag). The choice, referred to as an Operating Point (OP), is quantified in terms of these two values as calculated in $t\bar{t}$ MC samples.

SV0

During initial data taking periods a relatively simplistic and robust tagger, called SV0, was used. It is a lifetime based tagger, exploiting the time it takes a B-meson to decay and explicitly reconstructs secondary vertices from selected tracks within a jet. To determine whether a jet is a b-jet or not, a cut is made on the signed decay length significance, $L/\sigma(L)$, of the reconstructed secondary vertex. The sign of this quantity is determined by the projection of the decay length vector onto the jet axis. The relevant quantities are illustrated in Figure 4.2.

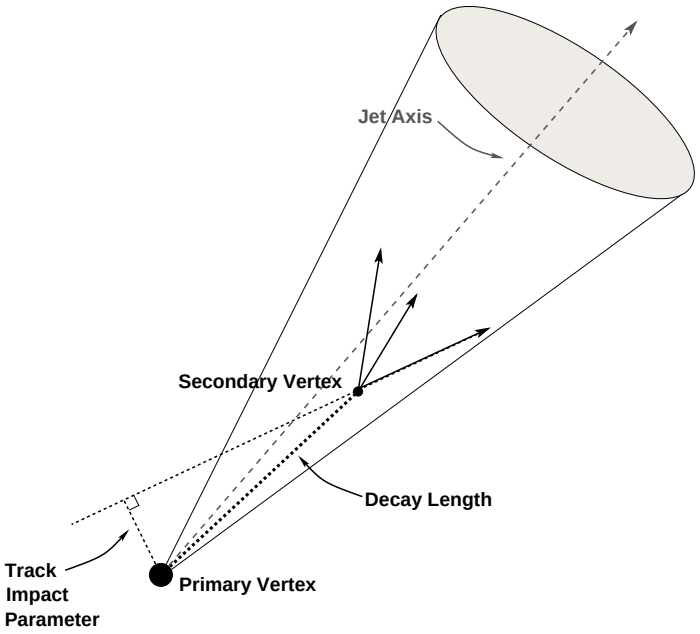

Figure 4.2: An illustraction of how the SV0 algorithm works, taken from [94].

JetFitterCOMBNN

Once a better understanding of the detector was attained, the use of more complex taggers such as JetFitterCOMBNN [95] was possible. This is constructed using two separate weights. The first is produced by an algorithm called JetFitter [96]. In JetFitter, a Kalman filter is used to construct a common line on which the primary vertex and possible heavy flavour vertices lie, resulting in an approximated flight path for a b-hadron. To discriminate, JetFitter uses a likelihood incorporating a number of variables such as decay length significances, the invariant mass of tracks associated to a vertex and the number of two track vertices. The second component of the JetFitterCOMBNN weight is obtained using the IP3D algorithm. This is an impact parameter based method which uses a likelihood ratio technique in which input variables are compared to pre-defined smoothed and normalised distributions for both the b-jet and light jet hypotheses. The combined tagger is calculated using a neural network of the JetFitter and IP3D taggers. The network has three output nodes for b, c and light jets and is trained to maximise light jet rejection.

MV1

The third algorithm used is known as `MV1` and it uses a neural network approach. It takes the weights of a number of other taggers, including JetFitterCOMBNN, as input and produces a single weight. This tagger is only used on the full 4.7 fb^{-1} dataset.

Calibration

It is crucial to know the efficiency of selecting a jet originating from a b-quark as well as the probability of mistakenly tagging a jet coming from a light quark or gluon. In general, the MC will not provide a perfect description of the efficiency and mistag rates and discrepancies with the data are quoted as scale factors:

$$\kappa_{\epsilon_b}^{\text{data/MC}} = \frac{\epsilon_b^{\text{data}}}{\epsilon_b^{\text{MC}}} \tag{4.4}$$

$$\kappa_{\epsilon_l}^{\text{data/MC}} = \frac{\epsilon_l^{\text{data}}}{\epsilon_l^{\text{MC}}} \tag{4.5}$$

Here $\epsilon_b^{\text{MC(data)}}$ and $\epsilon_l^{\text{MC(data)}}$ are the fractions of b-jets and light-flavour jets which are tagged in simulated events (data). Jets in Monte Carlo samples are reweighted using these scale factors, to ensure that the MC mimics the data correctly. Calculating ϵ_b^{MC} and ϵ_l^{MC} in MC is relatively simple, since the truth information is readily available. Calculating them in data is obviously more difficult, but can be achieved. The efficiency is estimated using semi-leptonic B hadron decays with a technique called p_{T}^{rel}, whilst the mistag rate is calculated using the negative tag method. For further details see [97].

4.4.7 Pile-up Reweighting

Monte Carlo samples are often generated prior to data taking, before the exact LHC running conditions are known. This means that only a best guess of the pile-up

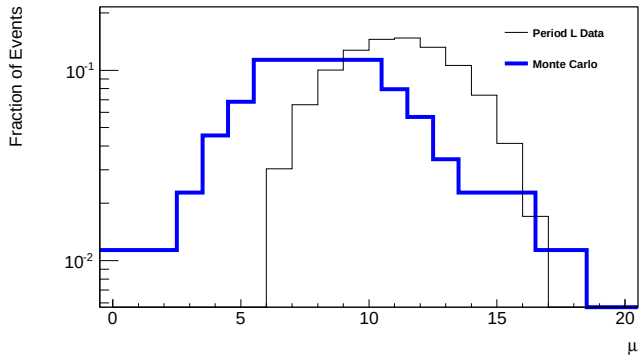

Figure 4.3: Average number of interactions per bunch crossing measured in data samples and produced for Monte Carlo simulation samples.

scenario can be made throughout the simulation of events. In order to counter this, a scheme was devised to re-weight Monte Carlo events in order to match the running conditions in data. The procedure utilises the average number of pile-up interactions, computed from beam parameters, and denoted $< \mu >$. Monte Carlo events were produced with a wide variety of values of μ, ranging from 0 to 20. The actual value of μ in data was measured using online luminosity monitors and is clearly very different, as can be seen in Figure 4.3. To address this, events in MC samples are reweighted so that they match the data distribution of $< \mu >$.

4.5 Variable Definitions

A number of event variables which are useful for discriminating different physics processes are listed here.

Minimum $\Delta\varphi$ or $\Delta\varphi_{min}$

This is defined as the minimum $\Delta\varphi$ between any of the leading n jets and the $\vec{E}_T^{miss}$ vector:

$$\Delta\varphi_{min} = \min(|\varphi_1 - \varphi_{E_{\mathrm{T}}^{\mathrm{miss}}}|, ..., |\varphi_n - \varphi_{E_{\mathrm{T}}^{\mathrm{miss}}}|) \tag{4.6}$$

where the index refers to the p_{T} ordered list of jets. It is primarily used as a means of reducing the amount of multijet production in event yields. This is because many of the selection cuts in this thesis involve a large $E_{\mathrm{T}}^{\mathrm{miss}}$ requirement. In the case of multijet production this $E_{\mathrm{T}}^{\mathrm{miss}}$ is often the result of the mismeasurement of a single jet's energy. If the mismeasurement is large enough for an event to pass the $E_{\mathrm{T}}^{\mathrm{miss}}$ cut, the $E_{\mathrm{T}}^{\mathrm{miss}}$ will be aligned to the jet, resulting in a low $\Delta\varphi_{min}$. In supersymmetric events, or other events with real $E_{\mathrm{T}}^{\mathrm{miss}}$, the missing energy is the result of a neutrino or a neutralino, which are unlikely to be aligned with a jet.

Effective Mass, $m_{\mathbf{eff}}$

The effective mass [98] is defined as the scalar sum of the p_{T} of the n jets selected in the analysis and the $E_{\mathrm{T}}^{\mathrm{miss}}$:

$$m_{\mathrm{eff}} = \sum_{i \leq n} ({p_{\mathrm{T}}}^{jet})_i + E_{\mathrm{T}}^{\mathrm{miss}} \tag{4.7}$$

It is a measure of the overall activity in an event. Busy supersymmetric events, such as gluino pair-production followed by subsequent decay chains, will have higher m_{eff} values than most Standard Model processes. In analyses which involve leptons the p_{T} of the additional objects is also included in the definition:

$$m_{\mathrm{eff}} = \sum_{i \leq n} ({p_{\mathrm{T}}}^{jet})_i + E_{\mathrm{T}}^{\mathrm{miss}} + p_{\mathrm{T}}^{lep} \tag{4.8}$$

Transverse Mass, $m_{\mathbf{T}}$

This is defined using the highest transverse momentum lepton in the event (${p_{\mathrm{T}}}^{lep}$) and the $E_{\mathrm{T}}^{\mathrm{miss}}$ as follows:

$$m_{\mathrm{T}} = \sqrt{2 p_{\mathrm{T}}^{lep} E_{\mathrm{T}}^{\mathrm{miss}} - 2 \vec{\mathbf{p}}_{\mathrm{T}}^{lep} \cdot \vec{\mathbf{E}}_{\mathrm{T}}^{\mathrm{miss}}} \tag{4.9}$$

This variable is often used in the definitions of 1-lepton control regions in order to gain a handle on W backgrounds and to reduce the amount of signal contamination.

Contransverse Mass, $m_{\mathbf{CT}}$

The contransverse mass, m_{CT} [99], is a kinematic variable that can be used to measure the masses of pair-produced semi-invisibly decaying heavy particles. For a system with two identical decays of heavy particles into visible particles (or particle aggregates) a_1 and a_2, and invisible particles, m_{CT} is defined as:

$$m_{\mathrm{CT}}^2(a_1, a_2) = \left[E_{\mathrm{T}}(a_1) + E_{\mathrm{T}}(a_2)\right]^2 - \left[\mathbf{p_T}(a_1) - \mathbf{p_T}(a_2)\right]^2, \tag{4.10}$$

It is an invariant quantity for two frames of reference boosted back-to-back in the transverse plane. m_{CT} is bounded from above by an analytical combination of particle masses. This bound is saturated when the two visible objects are collinear. When the pair production process is $p \to a + b$, where a is the visible component and b the invisible component, the bound is given by:

$$m_{CT}^{max} = \frac{m^2(p) - m^2(b)}{m(a)} \tag{4.11}$$

The boost-corrected contransverse mass [100] conservatively corrects m_{CT} to account for boosts in the transverse plane due to initial state radiation (ISR). This correction ensures that the calculated m_{CT} is not smeared to higher values due to the boost from ISR and hence protects the expected endpoint in the distribution.

4.6 Systematic Uncertainties

Imperfect knowledge and MC modelling of SM and SUSY processes can result in tension or agreement between expected and observed yields which does not reflect reality. It is crucial that these uncertainties are taken into account when intepreting an analysis. A brief overview of the major systematics, used throughout Chapters 7

to 9 is given here. Other, analysis dependent, systematic uncertainties are described in the relevant chapters.

4.6.1 Detector Uncertainties

Jet Energy Scale

The Jet Energy Scale (JES) correction to account for the difference in detector response to hadrons and electrons is not necessarily accurately modelled by the MC. To account for this, the uncertainty on the JES correction in MC is measured in data [92]. This uncertainty depends on jet p_{T}, η, flavour and the presence of nearby jets. The impact of the uncertainty on the event yield depends heavily on the number of jets required in the analysis.

Jet Energy Resolution

An extra p_{T} smearing is added to the jets based on their p_{T} and η, to account for a possible underestimation of the jet energy resolution (JER) in the MC simulation. The impact of this uncertainty is negligible in comparison to the JES uncertainty in early analyses.

B-tagging

The efficiency and mistag scale factors which are applied to the Monte Carlo are affected by a number of uncertainties. The derivation of the scale factors includes an MC component and this brings out uncertainties due to the heavy flavour modelling as well as detector uncertainties such as JES. Limited statistics in the data and the generalisation from semi-leptonic b hadron decays (used in the p_T^{rel} method) to inclusive b-jets, also contribute to the overall uncertainty. The final uncertainty on the yield is highly dependent on the number of b-jets required in a selection, as well

as the tagger being used. More sophisticated taggers, used in analyses with more integrated luminosity, reduce the tagging uncertainty.

Pile-up Uncertainties

The jet energy of soft jets is affected by pile-up conditions and this bias is not corrected for. Instead, it is considered as an uncertainty which is added in quadrature to the JES uncertainty. The uncertainty ranges from 7% for forward jets ($2.1 < |\eta| < 4.5$) with low p_{T} ($20 < p_{\mathrm{T}} < 50$ GeV) to 0 % for jets with $p_{\mathrm{T}} > 100$ GeV.

Lepton Identification Efficiency and Energy Scale

Scale factors that correct the electron identification efficiency in MC to that measured in $Z \to ee$ events have been calculated to always be within 3% of 1. Therefore, no electron scale factors were used throughout the analyses. Instead a conservative 3% systematic uncertainty on the final event yield was assumed.

The lepton energy scale is also known with an uncertainty of around 3% . The impact on the final event yield was evaluated by shifting all lepton momenta up and down by 3%. In the analyses described in this thesis the resulting effect was found to be smaller than 1% and therefore neglected.

Luminosity

An uncertainty is assigned to the integrated luminosity of a dataset. The luminosity is determined from the counting rates measured by the ATLAS luminosity detectors which are calibrated using van-der-Meer beam-separation techniques. The uncertainty varied between 11% at the start of data taking to around 3% on the full 5 fb^{-1} of 2011 [101].

4.6.2 Background Theoretical Uncertainties

Top Quark Production

When using the $t\bar{t}$ production cross section, both scale (renormalisation and factorisation) and Parton Distribution Function uncertainties are considered. Other uncertainties are calculated by varying the generation of events in some way. These uncertainties include:

- The uncertainty on the initial and final state radiation. This is evaluated by generating various samples with different initial and final state radiation settings and evaluating the impact of these changes on the event yields.
- The uncertainty on the parton shower model. This is estimated by evaluating the differences in expected background yields as calculated by `POWHEG` interfaced with `PYTHIA` and `HERWIG`.
- The default `MC@NLO` Monte Carlo is compared to `POWHEG` to obtain an uncertainty due to the use of a different NLO calculation.

Boson+Jets production Uncertainties

W production cross sections are normalised to NNLO calculations, with a theoretical uncertainty of 4% assigned to the inclusive W and Z plus jets cross sections. Further uncertainties on the boson plus jets expectations include:

- Uncertainties on the matching between hard radiation and showering affect the cross section ratios between the W plus $(n+1)$ jet samples and the W plus n jet samples. This uncertainty, sometimes referred to as the Berends-Giles uncertainty [102], is 24% per parton and for an n parton process it is $\sqrt{n} \times 24\%$.
- Scaling factors are applied to the to cross section values of W and Z production in association with heavy flavour jets. These account for the measured cross

section of b-jets in W events [103]. Theoretical uncertainties on the scale factors are considered.

4.6.3 Signal Theoretical Uncertainties

Renormalisation and Factorisation scale

The calculated cross section for supersymmetric processes depends on the choice of renormalisation and factorisation scale μ_R and μ_F. The default is to set these to be equal, i.e. $\mu_R{=}\mu_F{=}\mu$. The average mass of the produced sparticles is then used as a value for μ. The dependence on the chosen scale μ is considered as a systematic uncertainty with the scale set to vary between 2μ and $\mu/2$. For gluino-pair production $\Delta(\mu_R, \mu_F)$ varies between 15% and 17% as gluino mass increases and for sbottom pair production it is about 25% for all mass values.

Parton Distribution Function Uncertainties

The nominal values for the expected signal yields are estimated using the CTEQ6.6M PDFs [104] for the lightest 5 quarks/anti-quarks and the gluon. For each central PDF value, there are 22 PDF sets which take into account the systematic uncertainties coming from the experimental uncertainties of the measurements used to extract the PDF. This uncertainty is propagated to the final cross section by varying each of the 22 sets individually during the calculation of the cross section of a given process. This leads to 44 different outcomes of the cross section $(i, \pm)$, where the index $\pm$ denotes that the upper (lower) bound of the parameter is used, and index i is the PDF parameter. The resulting systematic uncertainty is then given by Equation 4.12.

$$\delta(PDF) = \frac{1}{2}\sqrt{(\sum(\sigma_i^+ - \sigma_i^-)^2)} \tag{4.12}$$

The relative uncertainty on the cross section σ^{NLO} is then given by:

$$\Delta(PDF) = \frac{\delta(PDF)}{\sigma^{NLO}} * 100\%.$$

These uncertainties, which are given in terms of 90% confidence level intervals, vary between 18% and 45% for gluino masses from 360 GeV to 1 TeV for gluino pair production. For sbottom pair production they range between 10% and 28% as a function of sbottom mass in the range 240 GeV to 650 GeV. In order to obtain the 68% confidence level uncertainties these values are divided by 1.645.

4.7 Statistical Tools

Any search for new physics results in either the observation and subsequent discovery of the proposed theory, or the rigorous exclusion of it as a viable alternative to the Standard Model. For this to be carried out properly it must be done within a solid mathematical framework. We describe here the statistical set-up utilised in the derivation of the exclusion limits of Chapters 6, 7 and 8.

In a cut and count analysis, the expected number of events $\lambda_{SR}[n]$ in the signal region is given by the sum of the Standard Model background and a possible new physics component as shown in Equation 4.13.

$$\lambda_{SR}[n] = \mu s + b_{SM} \tag{4.13}$$

Here s is the number of signal events, modulated by a signal strength parameter μ, and b_{SM} is the total Standard Model background. A value of $\mu = 0$ corresponds to no signal present and $\mu = 1$ corresponds to a signal cross section equivalent to that provided by the theory under study. The statistical model used is encoded within a likelihood function of the following form:

$$L(n|\mu, b, \theta) = P(n_{SR}|\lambda_{SR}(\mu, b, \theta)) \times P_{Syst}(\theta^0, \theta) \tag{4.14}$$

Uncertainties	
Correlated	Uncorrelated
Jet Energy Scale, Jet Energy Resolution, b-tagging efficiency, Luminosity lepton identification	Theoretical uncertainties, Statistical uncertainties, Factorisation & Renormalisation Scale

Table 4.1: Uncertainties and correlations used in the likelihood.

The first term is a Poisson distribution which reflects the measurement of the signal and background counts within the signal region. The function $\lambda_{SR}(\mu, \mathbf{b}, \theta)$ is the Poisson expectation. The second term incorporates the systematic uncertainties, which are dealt with as nuisance parameters. Correlations of systematics between signal and background are fully taken into account. The quantity θ^0 determines the nominal value of the variable, around which θ can be varied when maximizing the likelihood. Some of the uncertainties used throughout this thesis are listed in Table 4.1. The table also indicates which of the uncertainties are correlated between the signal and backgrounds.

4.7.1 Profile Likelihood

When constructing an interpretation one has to derive a quantity that depends on the data in such a way that it ranks outcomes as being more signal-like or more background-like, a quantity called the test statistic. The test statistic is denoted q_μ. Once its value has been obtained using the observed data, which is referred to as q_{obs}, a p-value quantifying the agreement between the data and the hypothesised value of μ can be constructed:

$$p = \int_{q_{obs}}^{\infty} f(q_\mu|\mu) dq_\mu \tag{4.15}$$

where $f(q_\mu|\mu)$ is the sampling distribution of q_μ under μ. A model is said to be excluded with a confidence level (C.L.) $1 - \alpha$ if $p < \alpha$. The standard in the field of particle physics, when deriving exclusion limits, is to work with a 95% C.L. and fix $\alpha = 0.05$ [105]. When setting exclusion limits on a particular model the value $\mu = 1$ is used and the p-value is denoted p_1. When attempting to reject the background

only hypothesis, as would be the case in the scenario of a discovery, then $\mu = 0$ and the p-value is called p_0.

The Neymann-Pearson lemma [106] states that the optimum way to test a hypothesised value of μ is to construct the profile likelihood ratio as given in Equation 4.16. The denominator is the unconditional Maximum Likelihood Estimator (MLE), as indicated by the single $\hat{}$ whilst the numerator is the conditional MLE for a given value of μ, denoted using $\hat{\hat{}}$.

$$\Lambda(\mu) = \frac{L(\mu, \mathbf{b}, \hat{\hat{\theta}})}{L(\hat{u}, \hat{\mathbf{b}}, \hat{\theta})} \tag{4.16}$$

The test statistic q_μ is then defined as follows:

$$q_\mu = \begin{cases} -2\ln\Lambda(\mu) & \text{if } \hat{\mu} > \mu \\ 0 & \text{if } \hat{\mu} < \mu \end{cases} \tag{4.17}$$

We set $q_\mu = 0$ when $\hat{\mu} < \mu$ since one does not consider upward fluctuations in the data over and above $b_{SM} + \mu s$ as representing incompatability with the hypothesised value of μ.

To evaluate the p-value in Equation 4.15 one needs to construct the probability distribution function of q_μ under signal assumptions corresponding to the background only hypothesis ($\mu = 0$) and the nominal signal strength hypothesis ($\mu = 1$). This can be done by generating toy Monte Carlo experiments and varying the nuisance parameters within their uncertainties.

In the scenario where a reasonably well populated signal region is used, a number of approximations can be made which greatly reduce the computational cost of the limit calculation. It can be shown [107] that in these cases $-2\ln\Lambda(\mu)$ can be simplified as follows:

$$-2\ln\Lambda(\mu) = \frac{(\mu - \hat{\mu})^2}{\sigma^2} + \mathcal{O}(1/\sqrt{N}) \tag{4.18}$$

where $\hat{\mu}$ is Gaussian with mean μ' and standard deviation σ, μ' being the signal strength parameter in the data. Neglecting the terms in $\mathcal{O}(1/\sqrt{N})$, the test statistic

in Equation 4.17 becomes:

$$q_\mu = \begin{cases} \frac{(\mu-\hat{\mu})^2}{\sigma^2} & \hat{\mu} > \mu \\ 0 & \hat{\mu} < \mu \end{cases} \tag{4.19}$$

This results in a p value which can be calculated very rapidly using the following analytic formula.

$$p_\mu = 1 - \Phi(\sqrt{q_\mu}) \tag{4.20}$$

Here Φ is the cumulative distribution for the standard Gaussian with unit mean and variance. This approximation circumvents the need to run toy Monte Carlo, which is an extremely computationally intensive procedure. It has been shown that this approximaiton is valid for values of background expectation, b_{SM}, larger than 10 [108]. Within the analyses described in this paper, when using approximately 10 events, the results derived using the Asimov approximation are always validated using toys.

4.7.2 Spurious Exclusion: PCL and CL_s

A fluke underfluctuation in the observed data could result in a limit where an experiment has no real sensitivity, an effect sometimes called *spurious exclusion*. This can be dealt with formally in two ways, as described below.

Power-Constrained Limits

Power Constrained Limits (PCL) [109] seek to prevent excessive exclusion due to under-fluctuations in the data by checking whether the power of the test, which is the probability to reject $\mu = 1$ when $\mu_{true} = 0$, is larger than some pre-determined threshold. When PCL is used within this thesis this threshold is taken to be 0.1587. This choice is motivated by the fact that it corresponds to requiring that the observed yield is within the resolution (1 sigma) of the background expectation. In practical terms this means that if the observed data count is larger than the expected value

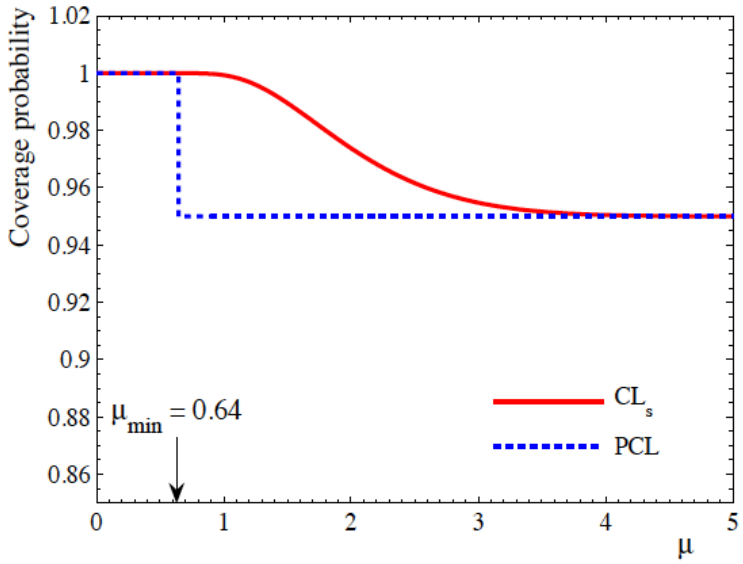

Figure 4.4: A comparison of the coverage obtained using PCL and CL_s

of d_{min}, defined as $d_{min} = b_{SM} - \sigma(b_{SM})$ then the exclusion limit is unaffected. In the scenario where the observed count is less than this quantity the observed limit is taken to be the limit which would have been obtained had d_{min} events been observed.

$\mathbf{CL_s}$

When using CL_s [110] one tests whether $CL_s < \alpha$ for a confidence level of $1 - \alpha$, where CL_s is defined as follows:

$$CL_s = \frac{CL_{s+b}}{CL_b} = \frac{p_1}{1 - p_0} \tag{4.21}$$

When we have an under-fluctuation in the data the value of p_0 goes up, diminishing the value of $1-p_0$ and increasing the overall CL_s value, weakening the exclusion limit. In general CL_s is more conservative than PCL as $1-p_0 < 1$, and will thus result in less stringent limits. This is reflected in the fact that the frequentist coverage probability of the CL_s upper limits is larger than the value being tested for. A comparison of the coverage of CL_s and PCL can be seen in Figure 4.4.

Chapter 5

The Jet Smearing Method

Qis mitt darba, u aqta' darba

5.1 Introduction

In searches for supersymmetry without leptons the multijet background arises from events where the p_{T} of one or many jets fluctuates to give rise to $E_{\mathrm{T}}^{\mathrm{miss}}$. Such fluctuations could either arise from jet energy mismeasurement or from real $E_{\mathrm{T}}^{\mathrm{miss}}$ in semi-leptonic heavy flavour decays. When a hard cut on $E_{\mathrm{T}}^{\mathrm{miss}}$ is introduced there is a very small probability for a multijet event to pass the signal region selection. This, combined with the large cross section, makes the multijet background extremely difficult to estimate. In particular, to obtain statistically meaningful results using a Monte Carlo technique would require the simulation of a prohibitively large sample. The background estimation method described in this chapter, which is called jet

smearing, was first used by ATLAS [111]. In the form presented here it has been used by a variety of published analyses [2] [7] [3] [4] [5]. The work in this chapter is entirely that of the author, unless explicitly stated.

The technique is based on repeatedly smearing the momentum of jets in clean data events, with little $E_{\mathrm{T}}^{\mathrm{miss}}$, to generate "pseudoevents" with possibly large $E_{\mathrm{T}}^{\mathrm{miss}}$ values. Each step of the method is described in detail throughout the chapter but a brief outline is given here:

1 Selection of events with little fake or real $E_{\mathrm{T}}^{\mathrm{miss}}$. These are called *seed events*.

2 Construction of a smearing or response function using a sample of simulated dijet events. This reflects the probability of measuring some jet p_{T} value for a given true jet p_{T}.

3 Validation of the smearing functions using data.

4 Smearing of the momentum of jets in seed events using the smearing functions. This operation is repeated a large number of times per seed event to randomly generate configurations where the $E_{\mathrm{T}}^{\mathrm{miss}}$ comes from one or multiple fluctuating jets.

5 The generated sample of smeared events, or pseudoevents, is then treated like a Monte Carlo sample and is normalised within a multijet enriched control region.

Figure 5.1 shows a cartoon of the jet smearing method in action. The diagram shows two events, with non-zero $E_{\mathrm{T}}^{\mathrm{miss}}$, generated from a single well-measured seed event.

5.2 Seed Selection

The kinematic configuration of seed events should mirror that of events selected in the analysis, with the exception that they should only contain jets which are well-measured, with little or no jet energy fluctuations. This means that only triggers

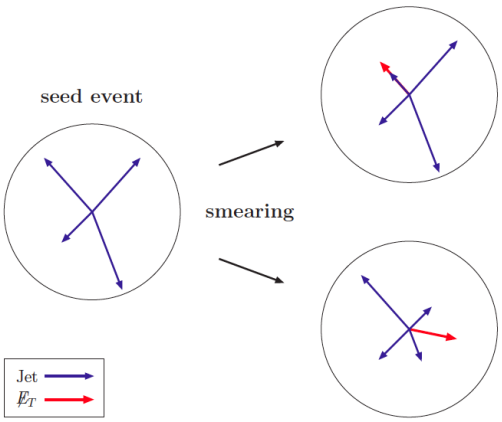

Figure 5.1: A cartoon showing how the jet smearing technique can take a well measured seed event and produce various low and high $E_{\mathrm{T}}^{\mathrm{miss}}$ configurations.

which do not cut explicitly on missing transverse energy can be used. This rules out the triggers used to select events for the various signal regions described in this thesis, which usually involve some $E_{\mathrm{T}}^{\mathrm{miss}}$ requirement. Instead, triggers which require a single jet of above some p_{T} threshold are used. Due to the fact that events which would fire these triggers are produced in copious amounts at the LHC, they are heavily prescaled. The trigger chains used, along with their average prescale values across the first 2 fb^{-1} and 4.7 fb^{-1} of data, are shown in Table 5.1. Also shown in the table are the Level 1 and Level 2 parts of the trigger chains.

Trigger Chain	L2	L1	Average Prescale	
			2 fb^{-1}	5 fb^{-1}
EF_j55_a4tc_EFFS	L2_j50	L1_j30	2017	5120
EF_j75_a4tc_EFFS	L2_j70	L1_j50	561	2470
EF_j100_a4tc_EFFS	L2_j95	L1_j75	165	690
EF_j135_a4tc_EFFS	L2_j95	L1_j75	16	178
EF_j180_a4tc_EFFS	L2_j95	L1_j75	2.9	41

Table 5.1: The 2011 prescaled trigger chains used to select seed events in the jet smearing analysis. The naming convention used is the one described in Section 3.8.

In order to minimize the complications introduced by working on the trigger turn

on, events passing a given trigger are retained only if they have a jet within the plateau for that trigger. Since the prescale values increased steadily with higher instantaneous luminosities, events are weighted using a prescale factor which is averaged over a given data period. Events containing high p_{T} jets will also pass the low p_{T} triggers so the prescale utilized is that of the hardest trigger for which the leading jet p_{T} in the event is on plateau. For the triggers shown in Table 5.1 the prescale selection would proceed as follows:

- If EF_j180_a4tc_EFFS is fired and leading jet $p_T > 260$ GeV then the event is retained and the prescale for EF_j180_a4tc_EFFS is used.
- If EF_j135_a4tc_EFFS is fired and leading jet 200 GeV $< p_T <$ 260 GeV then the event is retained and the prescale for EF_j135_a4tc_EFFS is used.
- If EF_j100_a4tc_EFFS is fired and leading jet 165 GeV $< p_T <$ 200 GeV then the event is retained and the prescale for EF_j100_a4tc_EFFS is used.
- If EF_j55_a4tc_EFFS is fired and leading jet 100 GeV $< p_T <$ 165 GeV then the event is retained and the prescale for EF_j55_a4tc_EFFS is used.

To ensure that the events are clean and do not contain large amounts of jet energy mismeasurement or neutrinos from heavy flavour jets, a cut on large $E_{\mathrm{T}}^{\mathrm{miss}}$ values could be used. This would however introduce a bias, where active events are relatively less likely to be selected, even when the total mismeasurement they contain is a small percentage of the overall event energy. To counter this, seed events are chosen using a cut on the $E_{\mathrm{T}}^{\mathrm{miss}}$ significance, S, which is defined as shown in Equation 5.1.

$$S = \frac{E_{\mathrm{T}}^{\mathrm{miss}}}{\sqrt{\sum E_T}} \tag{5.1}$$

Here $\sum E_T$ is the scalar sum of the transverse energy of all the objects in an event. Dividing by this number results in a scale invariant cut, thereby reducing the previously mentioned bias. The distribution of S is shown in Figure 5.2 in the full 4.7 fb^{-1} dataset taken by ATLAS in 2011. The cut on S is set at $S < 0.6$ GeV$^{1/2}$.

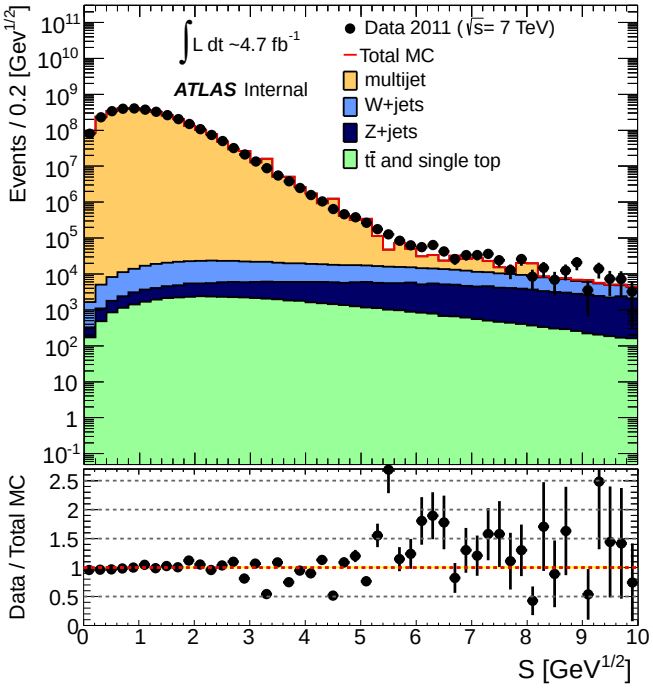

Figure 5.2: The $E_{\mathrm{T}}^{\mathrm{miss}}$ significance, S, in 4.7 fb^{-1} of data taken by ATLAS in 2011.

To reduce the computational cost of the technique, further cuts are required when selecting the seed events. This is done in order to avoid smearing events which will never make it into the signal region. These cuts are dependent on the particular analysis being considered, but typically include the requirement that there are no leptons (electrons and muons) in the event as well requirements on the jet momenta of the leading jet or jets. These cuts are set to be softer than the ones used to select signal region events in order to allow for upward smearing of jet momenta, which might promote events with soft jets into the signal region.

5.3 The Response Function

As discussed previously, the ATLAS calorimeter cannot reconstruct jets perfectly and therefore these objects have an associated resolution or response distribution. The

jet p_{T} response, denoted R, is defined as follows:

$$R = \frac{p_{\mathrm{T}}(\text{reco jet})}{p_{\mathrm{T}}(\text{true jet})} \tag{5.2}$$

In order to construct the detector response, R is evaluated for jets in a MC sample. The p_{T} of any neutrinos within $\Delta R(\text{true jet}, \nu) < 0.4$ of the jet are added back to $p_{\mathrm{T}}(\text{true jet})$, thereby ensuring that the full true jet momentum is accounted for. Since the jet response will depend on the jet p_{T}, it is segmented in bins of size 20 GeV in $p_T(\text{true jet})$. The resulting two-dimensional response is shown in Figure 5.3 and this is derived using the PYTHIA dijet Monte Carlo samples listed in Table 5.2. The table also shows the p_{T} ranges of the leading jets in the sample.

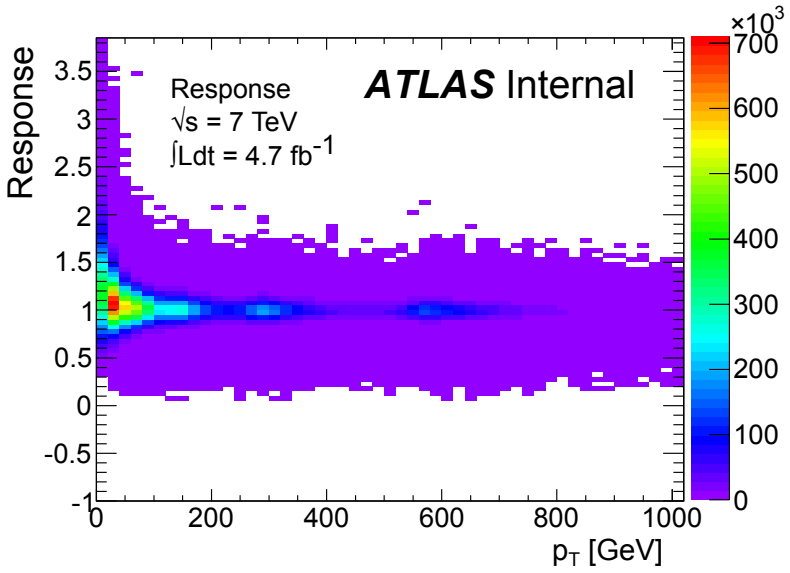

Figure 5.3: The response function, binned in true p_{T} and calculated using PYTHIA dijet samples.

Due to the fact that heavy flavour jets will in general have a different response to light jets, the response for b-tagged jets is differentiated from that of light jets. This separation is obtained using the b-tagging weight, with the exact details depending on the specific analysis. A consistent definition is used in the construction of the responses and to decide which response to use when smearing a jet. The larger

Name	p_{T} range	N(Generated)
J1	$17 < p_{\mathrm{T}} < 35$ GeV	7382565
J2	$35 < p_{\mathrm{T}} < 70$ GeV	2796084
J3	$70 < p_{\mathrm{T}} < 140$ GeV	2796879
J4	$140 < p_{\mathrm{T}} < 280$ GeV	2793179
J5	$280 < p_{\mathrm{T}} < 560$ GeV	2790576
J6	$560 < p_{\mathrm{T}} < 1120$ GeV	2790601
J7	$1120 < p_{\mathrm{T}} < 2240$ GeV	1395025
J8	2240 GeV $< p_{\mathrm{T}}$	1353250

Table 5.2: The PYTHIA Monte Carlo samples used to construct the jet response functions along with the number of events N_{gen} generated in each sample.

number of neutrinos present in heavy flavour jets results in a broader low side tail for their response. This can be seen in Figure 5.4 which shows a comparison of the response functions in different true p_{T} ranges for true b-jets, b-tagged jets and un-tagged jets.

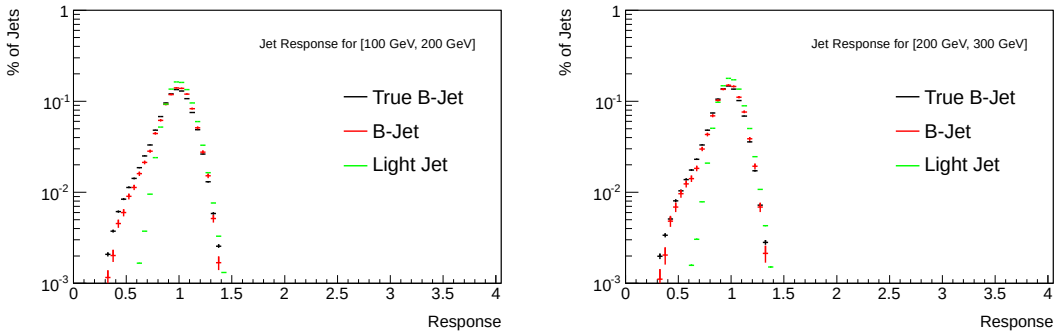

Figure 5.4: Plots of the response function for b-tagged jets (*red*), true b-jets (*black*) and un-tagged jets (*green*) as calculated using MC samples in the truth p_{T} ranges $[100, 200]$ GeV (*left*) and $[200, 300]$ GeV (*right*),

Figure 5.4 also shows that the response function itself contains two components, which have different physical origins. The central, or Gaussian, component of the response is dictated by the fact that the ATLAS calorimeters have a Gaussian resolution

and the tails, which are non-Gaussian, are either a result of real $E_{\mathrm{T}}^{\mathrm{miss}}$ in jets or large jet energy mismeasurement due to defects in the detector.

5.4 Validation in Data

In order to constrain the response functions so that they match the jet response in data, multijet dominated control distributions are used. Jet smearing on seed events is used to produce pseudoevents which can then be compared to the data. If disagreements are found, the response functions are corrected. Two techniques are used to modify the MC-derived response function, one focusing on the Gaussian component and the other on the non-Gaussian component.

Validating the Gaussian component: Dijet Balance

The Monte Carlo modelling of the width of the Gaussian component of the response, denoted σ_R, is investigated using the dijet balance $A(p_T(1), p_T(2))$, defined in Equation 5.3 for events with 2 jets with $p_{\mathrm{T}}(1)$ and $p_{\mathrm{T}}(2)$. The labels (1) and (2) indicate the p_{T} ordering of the jets.

$$A(p_T(1), p_T(2)) = \frac{p_T(1) - p_T(2)}{p_T(1) + p_T(2)} \tag{5.3}$$

This is a useful quantity as the width of $A(p_T(1), p_T(2))$, denoted σ_A, is related to σ_R. It can be shown that

$$\sigma_A \simeq \frac{\sigma_R(p_{\mathrm{T}})}{\sqrt{2}p_{\mathrm{T}}}. \tag{5.4}$$

where p_{T} is the average transverse momentum of the two jets. This means that the two widths can be related as shown in Equation 5.5.

$$\sqrt{2}\sigma_A = \frac{\sigma_{P_T}}{P_T} = \sigma_R \tag{5.5}$$

We calculate $A(p_T(1), p_T(2))$ for a selection of events having two, and only two jets. The sample is obtained using the following selection cuts:

- 2 jets with $p_T(1) > 100$ GeV and $p_T(2) > 40$ GeV
- A veto on events with a third jet of $p_T > 30$ GeV
- A cut on $\min_{i=1,2}(\Delta\varphi(E_{\mathrm{T}}^{\mathrm{miss}}, \mathrm{jet}_i)) < 0.3$ which ensures that the $E_{\mathrm{T}}^{\mathrm{miss}}$ is coming from one of the jets.

The dijet balance distribution in the data and in the pseudo-events is binned in p_T and fitted with a Gaussian. This is shown in Figure 5.5 for a particular p_{T} range. The mean of the Gaussian is set to 0 and the width and normalisation are fitted. The

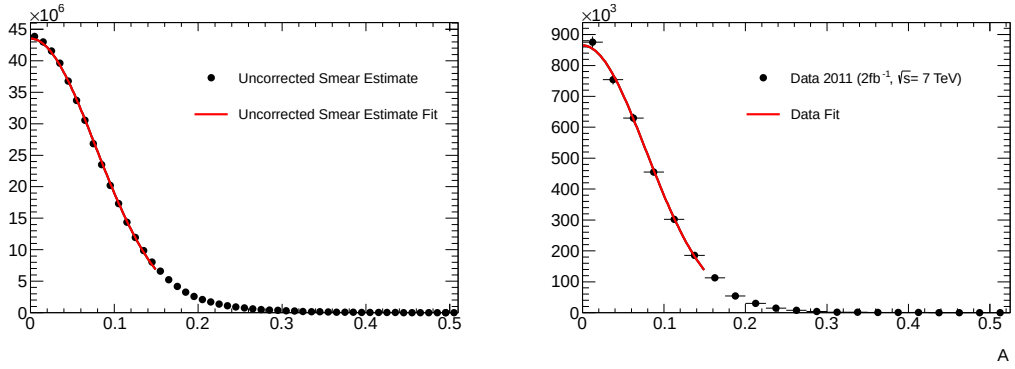

Figure 5.5: An example of the fit to the dijet balance A is shown for 140 GeV $< p_T <$ 160 GeV in the smeared pseudoevents (*left*) and the data (*right*).

values σ_A as derived using data and the pseudoevents are shown in Figure 5.6. The difference between the two is used as a p_{T} dependent correction of the MC-derived response function by convolving an additional smearing factor with the one obtained from the MC. The values of the correction run between 2% for jets with $p_T > 500$ GeV to 4% for jets with $p_T < 130$ GeV. The corrected response functions are fed through the same dijet balance analysis and the improvement can be clearly seen in Figure 5.6.

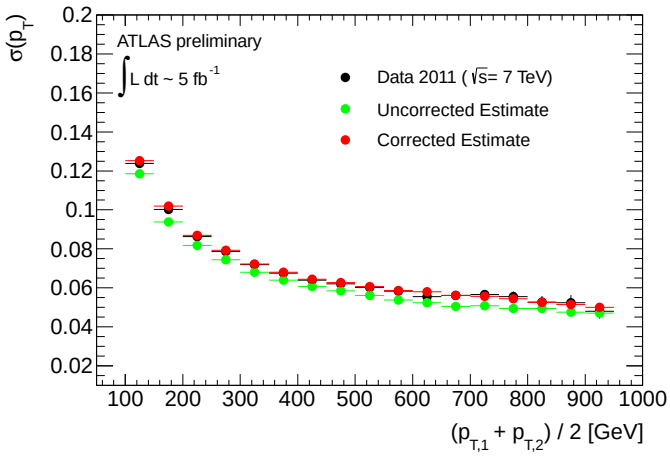

Figure 5.6: The widths σ_A of the balance distribution as derived from the data (*black*) and the smeared events before (*green*) and after (*red*) corrections.

Validating the non-Gaussian Component: The Mercedes Analysis

The tails of the smearing function are also validated on data. To do this, a sample of three jet events is used, where the $E_{\mathrm{T}}^{\mathrm{miss}}$ is unambiguously aligned with one of the jets. This allows the $E_{\mathrm{T}}^{\mathrm{miss}}$ to be attributed to the fluctuation of a single jet. In these cases one can estimate the true transverse momentum vector of the jet by adding back the $E_{\mathrm{T}}^{\mathrm{miss}}$ vector. The response of this jet, called R_2, is then given by:

$$R_2 \simeq \frac{\vec{p}_{\mathrm{T}}^{J} \cdot (\vec{p}_{\mathrm{T}}^{J} + \vec{E}_{T}^{miss})}{|\vec{p}_{\mathrm{T}}^{J} + \vec{E}_{\mathrm{T}}^{\mathrm{miss}}|^2}, \tag{5.6}$$

where $\vec{p}_{\mathrm{T}}^{J}$ is the reconstructed p_{T} of the jet associated with the $E_{\mathrm{T}}^{\mathrm{miss}}$. A cartoon showing the kind of event which needs to be selected can be seen in Figure 5.7. Such events are known as Mercedes events because of their resemblence to the three-pronged Mercedes logo. To construct the sample the following selection cuts are applied:

1 At least three jets with $p_T > 130, 40, 40$ GeV. This helps to reduce the $Z \to \nu\nu$ + jets contamination.

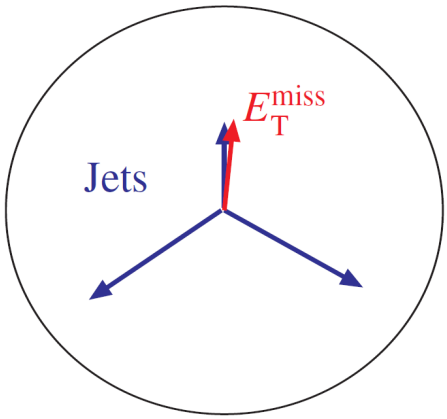

Figure 5.7: Mercedes event topology. $E_{\mathrm{T}}^{\mathrm{miss}}$ is unambiguously associated with one jet in the event. Events of this type are those used in the measurement of the non-Gaussian component of the jet response function.

2 A $E_{\mathrm{T}}^{\mathrm{miss}} > 30$ GeV which is parallel or anti-parallel to one, and only one, of the jets. To ensure this the jets are ordered in $\varphi_i = \Delta\Phi(J_i, E_{\mathrm{T}}^{\mathrm{miss}}); i = 1..n$ and two configurations are considered:

2.1 Parallel: In this case the $E_{\mathrm{T}}^{\mathrm{miss}}$ is a product of an underfluctuation and one requires that $|(\varphi_1)| < 0.1$. To rule out the cases where the source of the $E_{\mathrm{T}}^{\mathrm{miss}}$ is ambiguous one also requires that it is well separated from the jets in φ by requiring $|\varphi_1| < \pi - |\varphi_n|$, and $|\varphi_{(n-1)}| > 0.5$.

2.2 Anti-Parallel: Here the $E_{\mathrm{T}}^{\mathrm{miss}}$ is the product of a jet energy over-estimate and so is required to be on the opposite side of the event from one of the jets. This topology is enforced by requiring $\pi - |\varphi_n| < |\varphi_1|$, $\pi - |\varphi_1| < 0.1$ and $\pi - |\varphi_{(n-1)}| > 0.5$.

Figure 5.8 shows two Mercedes events in data taken by the ATLAS detector in 2010.

Figure 5.9 shows the R_2 distribution for tagged jets and un-tagged jets as measured with data and as estimated using the jet smearing method. One can see that the responses as derived using Monte Carlo responses and dijet balance corrections produce a reasonable estimate in both cases.

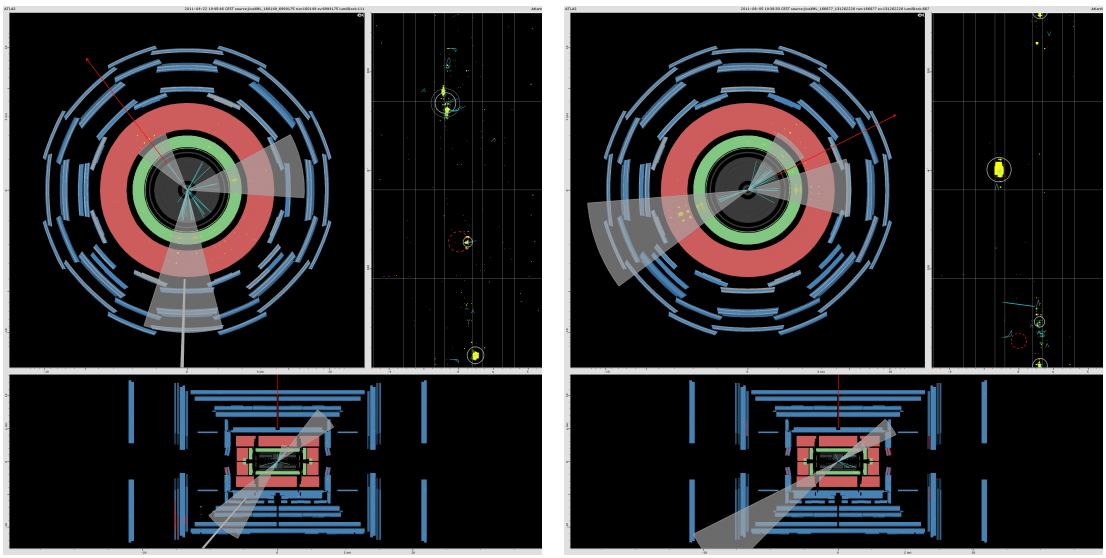

Figure 5.8: A Mercedes event in the parallel configuration (*left*) taken from Run 184169 (Event 89595740) and one in the anti-parallel configuration (*right*) taken from Run 180481 (Event 28450185).

Normalisation and Further Validation in Control regions.

Once all the modifications are put into place, the overall normalisation for the pseudoevents can be obtained using a multijet-enriched control region. This is often constructed using a selection where the $\Delta\varphi_{min}$ cut, as defined in Section 4.5, is reversed. The exact cuts applied to determine the control region are dependent on the specific analysis, but are always as similar to the signal region as possible. The control region is also used to ensure that the jet smearing method correctly reproduces the kinematics of multijet events. Issues regarding the normalisation and control regions will be shown on a per-analysis basis in the following Chapters.

5.5 Uncertainties on the Jet Smearing Method

There are a number of sources which could result in an incorrect estimate of the multijet background: these can be organised into uncertainties of a statistical or

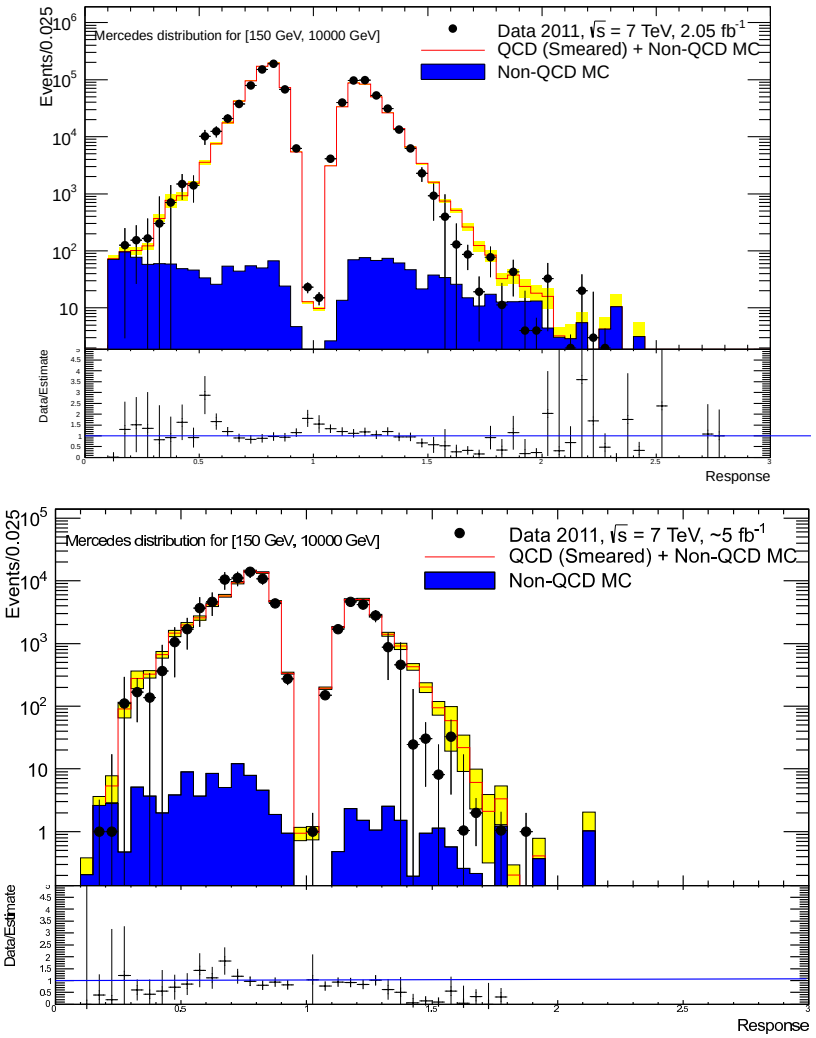

Figure 5.9: The R_2 distribution as measured in Mercedes events for un-tagged jets (*left*) and tagged jets (*right*). The multijet distributions shown are constructed using pseudoevents.

systematic nature. An overview of the major uncertainties is given here with further details and values provided in the Chapters describing the analyses where the jet smearing method is used.

5.5.1 Statistical Uncertainties

The limited number of data events in the normalisation region results in an uncertainty due to statistical fluctuations when normalizing the pseudoevents. Statistical errors are also present because of the limited smeared pseudoevents in the signal regions. This can be improved by increasing the number of smears applied and is rarely a major systematic. Finite statistics in the seed samples can also result in incorrect estimates and an uncertainty is assigned to seed fluctuations. This is estimated using a bootstrapping technique where sets of seed events are constructed by sampling with replacement from the original seed collection. These events are smeared and are passed through the analysis. The variance of the estimates is then used as a measure of the statistical uncertainty.

5.5.2 Systematic Uncertainties

Imperfect knowledge of the response function can also influence the estimate of the multijet yield in the signal region. A number of such systematic uncertainties are taken into account.

Uncertainty on the Correction to the Gaussian component

Despite the fact that the Gaussian component is validated in data, a conservative approach is taken and the size of the correction is varied up and down such that the smeared widths lie above and below the data as shown in Figure 5.5.2. For each variation, an estimate of the yield is calculated and the difference with respect to the nominal value is taken as an uncertainty.

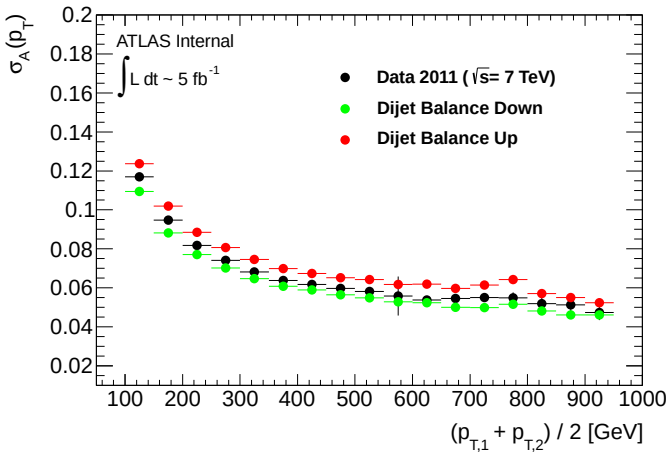

Figure 5.10: The figure shows the value of the dijet balance in the data and the two extremes taken to formulate the conservative dijet balance uncertainty.

Tagging Uncertainty

When building the response functions for light jets and b-jets in the Monte Carlo b-tagging is used. This introduces a tagging uncertainty which is taken into account by obtaining the yields but switching the b-tagged and light jet responses with the true b-jet and light jet ones.

Tail Uncertainty

To evaluate the uncertainty due to imperfect modelling of the tail component, the analysis is repeated after modifying the low side tail of the response function. The tail is scaled up and down by factors which push the smeared estimate above and below the R_2 distribution as calculated using the data. The analysis is repeated using these scaled responses and the differences obtained with respect to the nominal yield are used as systematic uncertainties.

Total Systematic Uncertainties

The total uncertainty on the jet smearing estimate of the multijet background is calculated by adding the various components in quadrature. The exact value of the uncertainty is analysis dependent, reaching to around 100% for certain searches described in this thesis. This value is fairly large: however, the estimated yield is often very small and almost always less than 5% of the total expected background. Hence such uncertainties have very little impact on the final interpretation of the results.

5.6 Treatment of a Fault in the LAr Calorimeter

During data taking in 2011 around 0.87 fb^{-1} of data were affected by problems in the LAr calorimeter where a region was not functional. The problem was localised in η and φ with a "hole" located at $-1 < \eta < 1.5$ and $-0.9 < \varphi < 0.5$. These issues imply additional complications for the multijet estimate because of the fact that the catastrophic energy loss within the hole causes extra mismeasurement over and above the standard jet response. This could be aggravated by the scenario where a jet pointing towards the LAr hole loses enough energy to no longer satisfy the definition of a jet. The event would then have substantial $E_{\text{T}}^{\text{miss}}$ pointing in the direction of the LAr hole, without a jet close by. Therefore it would pass the $\Delta\varphi_{min}$ cut and filter into the signal region.

The background arising from mismeasurement due to the LAr hole is tackled as a separate process. Response functions are derived using a Monte Carlo sample which has the LAr hole built into the simulation. Due to the limited statistics of this sample and because we expect the dominant effect to be the hole, only two p_{T} bins are used. A flat 100% uncertainty is assigned to these events. The same kind of cross-checks are applied to ensure that the modelling of the hole is accurate. Further details can be found in Appendix B.

5.7 Cross Checks of the Jet Smearing Method

When possible, the jet smearing method is corroborated by other background estimation techniques. This includes using both Monte Carlo and other data driven methods. In particular jet smearing is used as a cross-check of a data driven method in a 6 to 9 jet analysis looking for supersymmetry [7]. A relatively soft $S_{E_T^{Miss}}$ cut of 3.5 $\mathrm{GeV}^{1/2}$ is used to distinguish the signal from the background. The multijet background is the dominant background in this case, amounting to over 50% of the total Standard Model yield in the signal region. The main multijet estimation technique makes use of the fact that the $S_{E_T^{Miss}}$ shape is independent of the number of jets required. Therefore the shape of the variable can be derived in a region with a lower jet multiplicity than the signal region. The distribution is then normalised in a control region where the $S_{E_T^{Miss}}$ cut is reversed. The technique is referred to as the Template method. The jet smearing technique is used as a cross-check of the Template method. Across the various signal regions, with different numbers of jets (6-9) having different p_{T} requirements (80 GeV - 55 GeV), the two methods agree within the systematic uncertainties of the template method.

5.8 Summary

The jet smearing technique allows for the estimation of the multijet background in analyses with hard $E_{\mathrm{T}}^{\mathrm{miss}}$ requirements. It starts off with response functions derived using MC samples and validates or corrects these using the data in two specific control regions. This allows for the investigation of different regions of the response shape.

Future work on the jet smearing method involves a better use of triggers specific to analyses containg b-jets. In particular, using b-jet triggers will help to improve the statistics of events with low leading jet p_{T}, which are currently limited in later periods due to the large pre-scales on low jet p_{T} triggers. Also, a thorough study of the seed selection could help to improve statistics while keeping seed selection biases down.

Chapter 6

Sbottom Pair Production

Biex taqta' sewwa trid tisma ż-żewġ naħat

6.1 Analysis Abstract

This chapter describes a search for pair production of the scalar partners of the bottom quark in 2 fb^{-1} of pp collisions at $\sqrt{s} = 7$ TeV, using the ATLAS detector. Scalar bottoms are searched for in events with large missing transverse momentum and two b-jets in the final state. Interpretation is carried out in an R-parity conserving minimal supersymmetric scenario, assuming that the scalar bottom decays exclusively into a bottom quark and a neutralino. Upper limits at 95% confidence level are obtained in the $(m_{\tilde{b}_1}, m_{\tilde{\chi}_1^0})$ plane. For neutralino masses below 120 (60) GeV, scalar bottom masses up to 350 (390) GeV are excluded.

The analysis described here was published in [2]. The author's contributions include the study of various signal properties and systematics, the analysis optimisation, the estimation of the multijet background and the interpretation of the results. The author also cross-checked other components of the analysis, including the SM Monte Carlo expectations and systematic uncertainties as well as the observed data yields.

6.2 Introduction

This chapter focuses on direct sbottom pair production, where two sbottom quarks are produced, each decaying into a b-quark and a neutralino. While the signal process itself is relatively simple, the search for direct sbottom production is challenging for two reasons. First of all the cross sections, shown in Figure 6.1, are fairly low, especially in comparison to processes such as gluino-gluino pair production. Secondly, the signal events are not very active as they contain only 1 decay per sbottom, with just 2 visible objects per event.

Since the mass of the sbottom and the neutralino are unknown free parameters in the MSSM, they are not fixed in this search. Instead, the sbottom mass is allowed to vary between 200 Gev and 600 GeV. The neutralino mass is allowed to vary between 0 GeV and $m_{\tilde{b}_1} - m_b$. Due to restricted computational resources a grid of approximately 100 signal points in the $(m_{\tilde{b}_1}, m_{\tilde{\chi}_1^0})$ plane is generated using `HERWIG` and `SUSYHIT`. For each point 20,000 SUSY events with fixed sbottom and neutralino mass are generated. To isolate the desired production process, all supersymmetric particles other than the sbottom quark and the neutralino are set to very high mass, above the production threshold at 7 TeV.

In the signal under consideration exactly 2 b-quarks are expected, each leading to a b-jet. When $m_{\tilde{b}_1} - m_{\tilde{\chi}_1^0} > 100$ GeV, these b-jets should possess a hard p_{T} spectrum. Extra jets produced via initial and final state radiation would present softer spectra and need not be b-jets. The neutralinos in the event are expected to result in large $E_{\mathrm{T}}^{\mathrm{miss}}$ values in comparison with what one would observe in SM events.

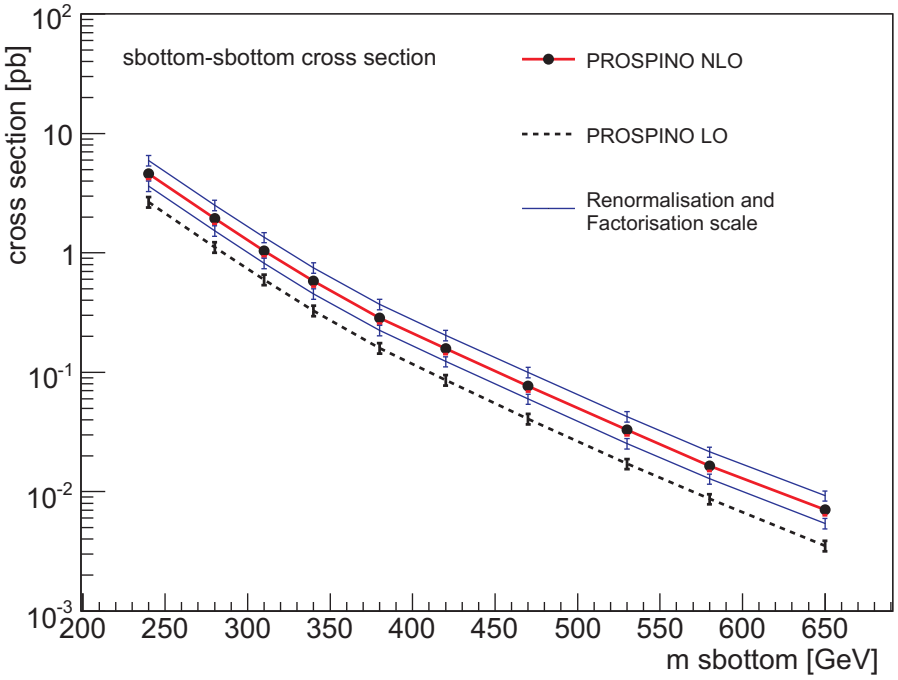

Figure 6.1: The sbottom pair production cross section as derived using PROSPINO.

6.3 Optimisation and Event Selection

The trigger chosen for this analysis uses a combination of a single jet trigger and a $E_{\mathrm{T}}^{\mathrm{miss}}$ trigger. This is seeded by a Level 1 trigger which requires a jet with $p_{\mathrm{T}} > 55$ GeV and $E_{\mathrm{T}}^{\mathrm{miss}} > 20$ GeV. The jet threshold is raised to 70 GeV at Level 2. At the Event Filter level the leading reconstructed jet is required to have a p_{T} greater than 75 GeV and the $E_{\mathrm{T}}^{\mathrm{miss}}$ must be larger than 45 GeV. The trigger thresholds drive the leading jet p_{T} and $E_{\mathrm{T}}^{\mathrm{miss}}$ offline cuts, to ensure that selections are made in the plateau of the trigger efficiency. This helps to avoid systematic uncertainties connected with the trigger turn-on curve being badly modeled by the Monte Carlo simulation. Event and jet cleaning cuts are applied to remove calorimeter noise and muons coming from cosmic rays, which might skew the event kinematics. Following the trigger selection and data quality cuts, the baseline 2-jet selection is:

- No leptons (electrons or muons). This is implemented because the signal contains no prompt leptons. Furthermore, standard model processes with real $E_{\mathrm{T}}^{\mathrm{miss}}$ often also contain leptons.

- A leading jet with p_{T} >130 GeV and sub-leading jet with p_{T} >50 GeV. These cuts are motivated by the fact that signal events are expected to contain at least two jets from the sbottom pair production process, and possibly extra jets from initial or final state radiation.

- A minimum $E_{\mathrm{T}}^{\mathrm{miss}}$ of 130 GeV, which is trigger driven.

- In order to reduce the amount of multijet background, a cut of $\Delta\varphi(\mathrm{jet}_{1,2} - E_{\mathrm{T}}^{\mathrm{miss}}) > 0.4$ is applied.

- Further reduction of the multijet background is obtained by cutting on the ratio $E_{\mathrm{T}}^{\mathrm{miss}}/m_{\mathrm{eff}}$. The value of the cut is placed at 0.25 .

- Due to the fact that the signal under study contains 2 heavy flavour quarks, at least 2 b-jets with p_{T} > 50 GeV are required. The JetFitterCOMBNN algorithm is used. The operating point selected has an efficiency of 60% and a mistag rate of $< 1\%$ in a $t\bar{t}$ MC sample.

The dominant background in events with 2 b-jets and large $E_{\mathrm{T}}^{\mathrm{miss}}$ is top pair production, with one of the W bosons from the top decaying leptonically. This will pass the selection cuts if the lepton is very soft, missed by the detector, or reconstructed as a jet. In order to suppress this background the contransverse mass (m_{CT}), as defined in Section 4.5, is used. This quantity is useful when tackling pair production because it contains a kinematic endpoint which depends on the mass of the pair produced particle and the mass of the invisible decay products. For top events the value of the endpoint can be calculated using Equation 4.11, with $m_{\mathrm{CT}}^{max}(t\bar{t})$ given by

$$m_{\mathrm{CT}}^{max}(t\bar{t}) = \frac{m^2(t) - m^2(W)}{m(t)} \approx 137 \text{ GeV} \tag{6.1}$$

where we have made the assumption that the lepton from the W boson is missed. In the signal being considered, the shape and endpoint of m_{CT} will depend on the mass

hierarchy of the $\tilde{b}_1$ and $\tilde{\chi}_1^0$. Figure 6.2 shows the m_{CT} distribution for a number of signal points. For a $\tilde{\chi}_1^0$ mass fixed at around 80 GeV and increasing $\tilde{b}_1$ masses (240 GeV, 280 GeV and 350 GeV) the endpoint gets larger. However, it is mass difference which drives the value, as per Equation 4.11, and therefore large $\tilde{b}_1$ mass and large $\tilde{\chi}_1^0$ mass results in a softer spectrum, as can be seen from the ($m_{\tilde{b}_1} = 350$ GeV, $m_{\tilde{\chi}_1^0} = 200$ GeV) mass hypothesis. In order to be sensitive to a variety of mass hierarchies, three cuts on m_{CT} are considered, with values of 100 GeV, 150 GeV and 200 GeV.

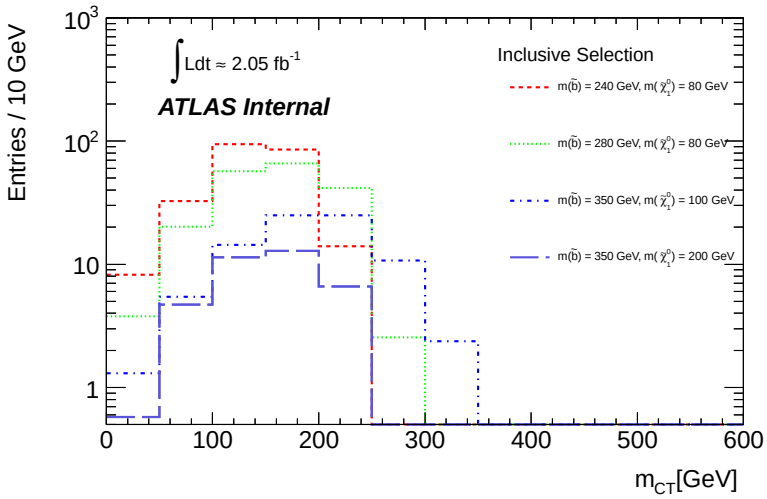

Figure 6.2: The distribution of boost-corrected contransverse mass (m_{CT}) for a number of signal points.

Initial and final state radiation could result in a relatively soft third jet in signal events. This can be seen in Figure 6.3 (top), which shows the number of jets with $p_{\mathrm{T}} > 20$ GeV, after the baseline selection for two signal points. The distributions are also shown for the expected standard model backgrounds, as estimated using Monte Carlo. Whilst both inclusive and exclusive two jet selections were initially considered, a two jet exclusive selection, where a veto on the p_{T} of the third jet is imposed, is found to result in better signal to background ratio. The cut on the third jet p_{T} was set at 50 GeV, to avoid vetoing signal events which have soft initial or final state radiation jets. Figure 6.3 (bottom) shows the expected signal yields in 2 fb^{-1}, with

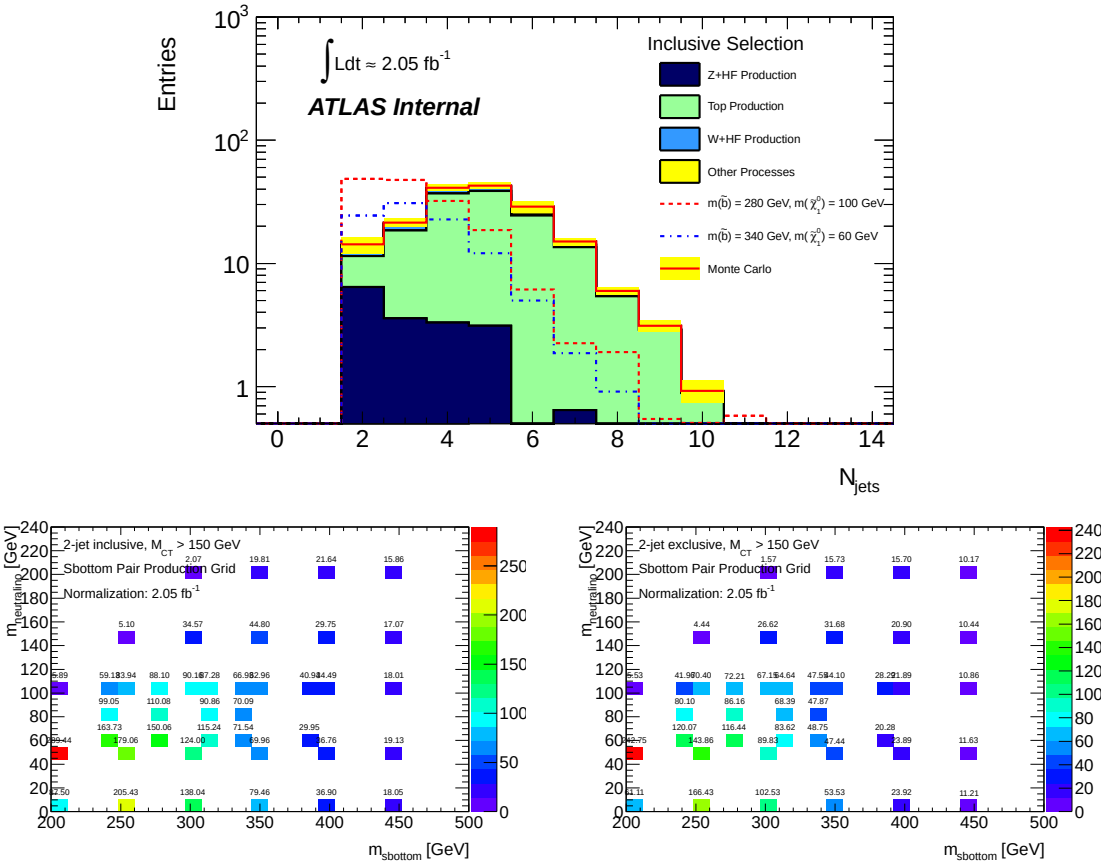

Figure 6.3: *Top*: The number of jets expected after the baseline selection. Two signal points are also shown for comparison. *Bottom*: Expected signal events across sbottom-neutralino mass planes for m_{CT} >150 GeV for the 2-jet inclusive (*left*) and 2-jet exclusive (*right*) selections.

and without the veto applied. The signal efficiencies vary between 1% and 6% as the sbottom mass increases from 200 GeV to 500 GeV.

Figure 6.4 shows the significance across the sbottom neutralino mass plane for an m_{CT} cut of 150 GeV in both the inclusive and exclusive cases. The significance is calculated using $S = \mathrm{Signal}/\sqrt{\mathrm{Background}}$. The exclusive selection cuts yield higher significances. The same conclusions hold for the softer ($m_{\mathrm{CT}} > 100$ GeV) and harder ($m_{\mathrm{CT}} > 200$ GeV) cuts. Figure 6.5 shows the effect of the same cuts, with a slightly more realistic definition of the sensitivity, given by $S/\sqrt{B + (\Delta B)^2}$, where

ΔB represents an approximate uncertainty, used solely for optimisation purposes. The value of ΔB is set to 30% for the inclusive analysis and 35% for the exclusive analysis, which is expected to be more sensitive to JES and ISR uncertainties. Again, the figure indicates that, for $m_{\mathrm{CT}} > 150$ GeV, the exclusive analysis results in higher significances across the board. Similar conclusions also apply to the other m_{CT} cuts.

Throughout this chapter the focus is on the exclusive selection: however, the resulting distributions are presented for both sets of cuts, to ensure the robustness of the background estimation.

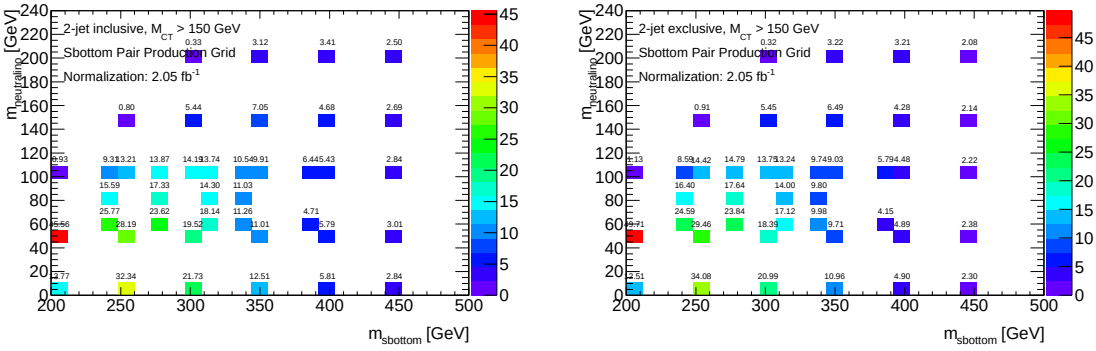

Figure 6.4: The significance across sbottom-neutralino mass plane for m_{CT} >150 GeV for 2-jet inclusive (*left*) and 2-jet exclusive (*right*) selection.

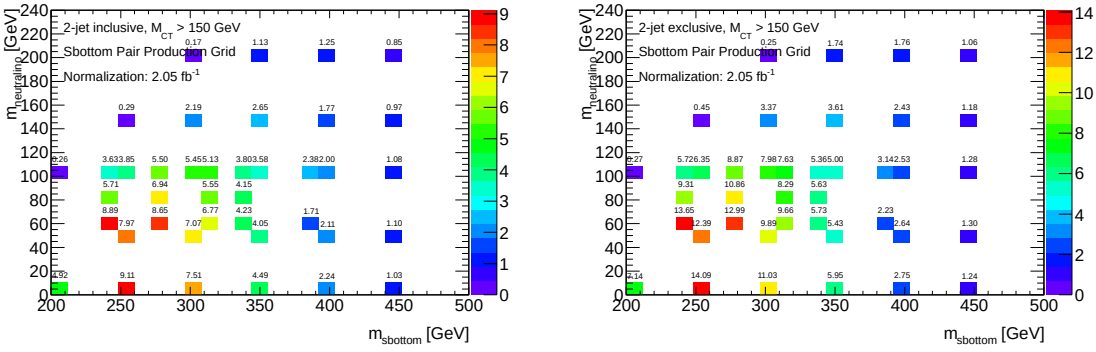

Figure 6.5: The significance, including approximate systematics, across sbottom-neutralino mass plane for m_{CT} >150 GeV for 2-jet inclusive (left) and 2-jet exclusive (right) selection.

6.4 Background Estimation

Following the signal selection described in the preceding section, the major SM processes contributing to the background are top quark pair and single top production as well as associated production of W/Z bosons with heavy flavour jets. In particular, the signal region with $m_{\mathrm{CT}} > 100$ GeV is dominated by semi-leptonic $t\bar{t}$ events as a consequence of the cut being less than the 135 GeV m_{CT} endpoint in top pair production. The signal regions with $m_{\mathrm{CT}} > 150$ and 200 GeV are dominated by the irreducible Z+$b\bar{b}$ production with $Z \to \nu\nu$ decay, and by W+$b\bar{b}$ production with $W \to \tau\nu$. These non-multijet backgrounds are estimated using a semi-data driven technique which was not the work of the author. However, for completeness, the estimates are described in Section 6.4.2. Contributions from diboson and associated production of $t\bar{t}$ with W, Z or additional b-jets are sub-dominant and are estimated using Monte Carlo. The multijet background is estimated using the jet smearing method, described in detail in Chapter 5. Details pertaining to this particular analysis are given in Section 6.4.1. Non-collision backgrounds were found to be negligible.

6.4.1 Multijet Background Estimation

The jet smearing technique is used with the response functions and data driven corrections described in Chapter 5. We discuss here the normalisation of the pseudoevents, the kinematics in a multijet-dominated control region and the actual estimation itself.

Sample Normalisation

In order to normalise the pseudoevents, a control region with reversed $\Delta\varphi_{min}$, such that $\Delta\varphi_{min}(\mathrm{jets}_{1,2} - E_{\mathrm{T}}^{\mathrm{miss}}) < 0.4$, is constructed. Since the $\Delta\varphi_{min}(\mathrm{jets}_{1,2} - E_{\mathrm{T}}^{\mathrm{miss}})$ variable is what distinguishes the signal region from the control region, it is crucial that it is well modelled by the jet smearing technique. A poor description of the shape would result in an incorrect ratio of the number of events in the signal region

to the background and this would bias the multijet estimate. Figure 6.6 shows the $\Delta\varphi_{min}(\text{jets}_{1,2} - E_{\text{T}}^{\text{miss}})$ distributions before and after the third jet veto. The figure is normalised to the control region, which dominates the plot in terms of statistics. The figure indicates good agreement within the statistical uncertainties.

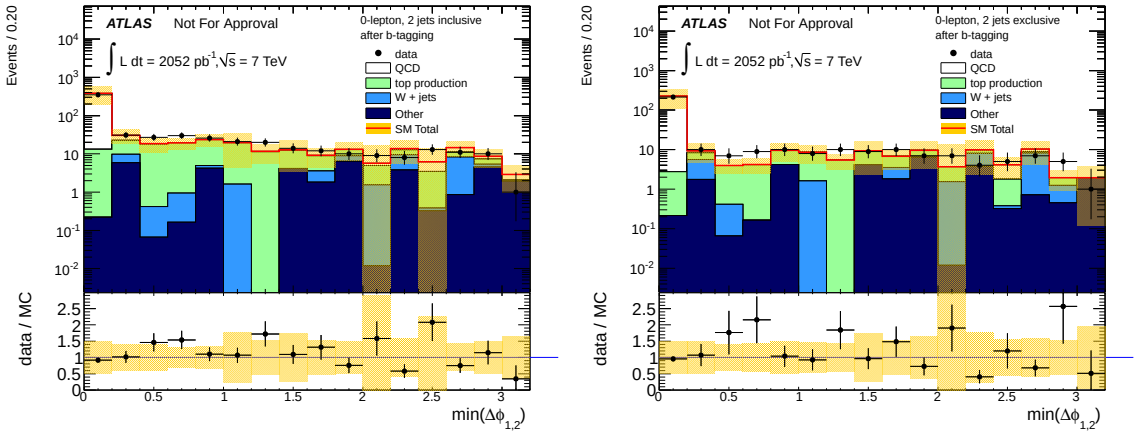

Figure 6.6: The min $\Delta\varphi(\text{jets}_{1,2} - E_{\text{T}}^{\text{miss}})$ distribution before (*left*) and after (*right*) the third jet veto. The multijet component is estimated using jet smearing pseudoevents.

Control Region Kinematics

Other variables such as $E_{\text{T}}^{\text{miss}}$ and m_{CT} are investigated in the control region to ensure that the kinematics quantities of the smeared pseudoevents match the data. Figure 6.7 shows these distributions and once again reasonable agreement between the smeared estimate and the data is observed.

Signal Region Estimate

The distribution of $\Delta\varphi(\text{j}_3 - E_{\text{T}}^{\text{miss}})$ in the smeared events is shown in Figure 6.8 with all cuts up to, but excluding, the m_{CT} cuts. The figure shows that most of the residual multijet events have a third leading jet which is aligned to the $E_{\text{T}}^{\text{miss}}$, as expected. An additional cut on $\Delta\varphi(\text{j}_3 - E_{\text{T}}^{\text{miss}}) > 0.2$ on third leading jets with $p_{\text{T}} > 30$ GeV,

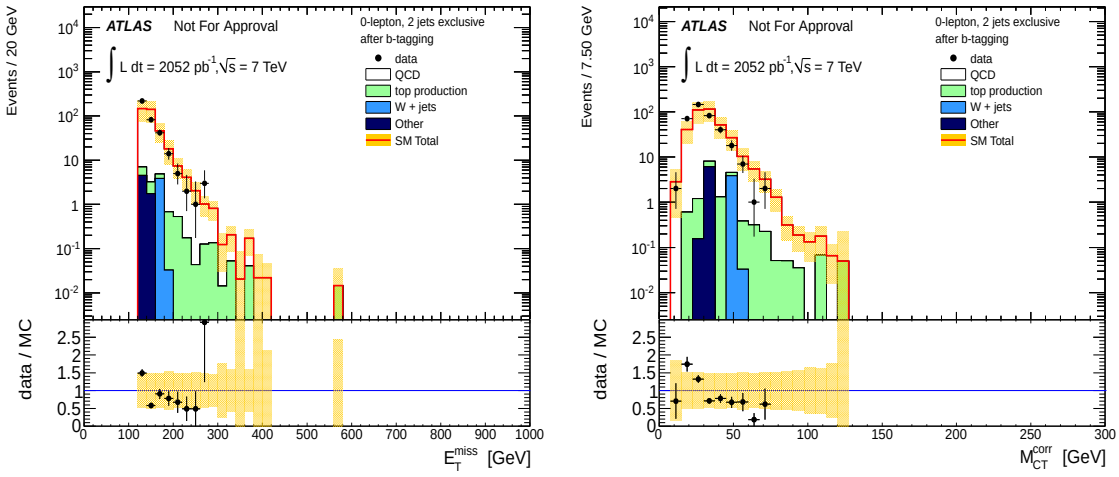

Figure 6.7: Distributions of the $E_{\mathrm{T}}^{\mathrm{miss}}$, the p_{T} of the two leading jets, and m_{CT} for $\Delta\varphi(j1, 2 - E_{\mathrm{T}}^{\mathrm{miss}}) < 0.4$ control sample after the 2-jet exclusive selection.

is found to reject these multijet events by a factor of two, with negligible ($<5\%$) impact on the yields from the signal and non-multijet backgrounds. Due to the large uncertainties associated with the multijet background, this extra cut is implemented in the analysis in order to reduce the multijet yield as much as possible.

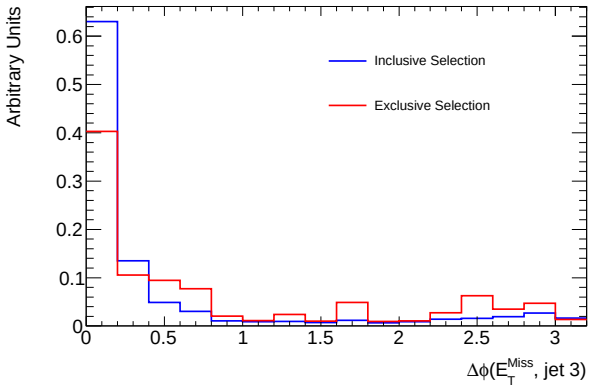

Figure 6.8: The distribution of $\Delta\varphi(\mathrm{j}_3 - E_{\mathrm{T}}^{\mathrm{miss}})$ for the QCD-multijet pseudoevents sample. Events with at least two b-tagged jets and passing all selection cuts up to, but not including, the m_{CT} cut are considered.

The final predictions of the multijet background in the three signal regions are reported in Table 6.1. Jets with p_{T} above 30 GeV are considered for the additional

$\Delta\varphi(\mathrm{j}_3 - E_{\mathrm{T}}^{\mathrm{miss}})$ selection. The table shows both the nominal multijet contribution as well as the expected number of events arising because of the LAr hole issues during part of the data taking (see Section 5.6). A conservative 100 % uncertainty is assigned in all signal regions.

Selection	Nominal Multijet	LAr Multijet	Total Events
Exclusive, 2 b-jets	1.10	0.67	1.77±1.77
Exclusive, m_{CT} >100 GeV	1.00	0.58	1.58±1.58
Exclusive, m_{CT} >150 GeV	1.00	0.40	1.40±1.40
Exclusive, m_{CT} >200 GeV	0.01	0.08	0.09±0.09

Table 6.1: The estimate of the multijet background for 2.05 fb^{-1}, as derived using the jet smearing method. The results are shown for both the normal multijet background, as well as that expected as a result of problems in the LAr hole.

6.4.2 Non-Multijet Background Estimation

A semi-data driven approach was used to estimate the major SM background contributions to the signal regions. This method works by defining data control regions where the background under study is dominant. The estimation in the signal region is then obtained by multiplying the number of events observed in the corresponding control region by a transfer factor, defined as the ratio of the MC predicted yield in the signal region to the MC predicted yield in the control region:

$$N_{\mathrm{SR}} = \frac{N_{\mathrm{SR}}^{\mathrm{MC}}}{N_{\mathrm{CR}}^{\mathrm{MC}}}(N_{\mathrm{CR}}^{\mathrm{obs}} - N_{\mathrm{CR}}^{\mathrm{others}}) = T_f(N_{\mathrm{CR}}^{\mathrm{obs}} - N_{\mathrm{CR}}^{\mathrm{others}}) \tag{6.2}$$

$N_{\mathrm{CR}}^{\mathrm{obs}}$ denotes the observed yield in the control region and $N_{\mathrm{CR}}^{\mathrm{others}}$ includes all backgrounds except for the one of direct interest. The advantage of this approach is that systematic uncertainties that are correlated between the numerator and the denominator of T_f largely cancel out, provided that the event kinematics in the corresponding signal and control regions are similar.

Top and $W+b\bar{b}$ Estimate

The contributions from top and $W+b\bar{b}$ production are estimated using a control region where events have exactly one electron or muon, $E_{\mathrm{T}}^{\mathrm{miss}}$ >80 GeV and at least two b-jets with p_{T} >130 GeV and 50 GeV. The transverse mass of the $(\ell, E_{\mathrm{T}}^{\mathrm{miss}})$ system is required to be between 40 GeV and 100 GeV to select events containing $W \to \ell\nu$. Monte Carlo simulation is used to estimate the contribution of other standard model processes to this control region. These processes amount to approximately 10% of the control region yield. Figure 6.9 shows the measured m_{CT} distribution in the 1-lepton control region, which shows that Monte Carlo models the data well in the control region.

Z+$b\bar{b}$ Estimate

The Z+$b\bar{b}$ contribution is estimated using a transfer factor from a control region where events have two opposite-sign same-flavour leptons ($\ell^+\ell^-$), $E_{\mathrm{T}}^{\mathrm{miss}}$ >50 GeV and at least two b-jets with p_{T} >80 GeV and 50 GeV. The invariant mass of the two leptons, $m_{\ell\ell}$, is required to be between 81 GeV and 101 GeV in order to ensure that the electrons are coming from a Z boson. The momenta of the leptons are added to the $E_{\mathrm{T}}^{\mathrm{miss}}$ to mimic the $Z \to \nu\nu$ decay. The contribution from top quark production in this control region accounts for about 50% of the total and is subtracted using a side-band estimate in two 40 GeV mass windows above and below the Z mass interval. Figure 6.9 shows this control region and indicates that the MC models the data well.

Other Backgrounds

Other non-multijet, sub-dominant backgrounds include diboson production, $t\bar{t}$ plus W/Z production and $t\bar{t}b\bar{b}$. These are estimated using Monte Carlo simulation and account for 1% to 5% of the total SM prediction, increasing with the m_{CT} cut.

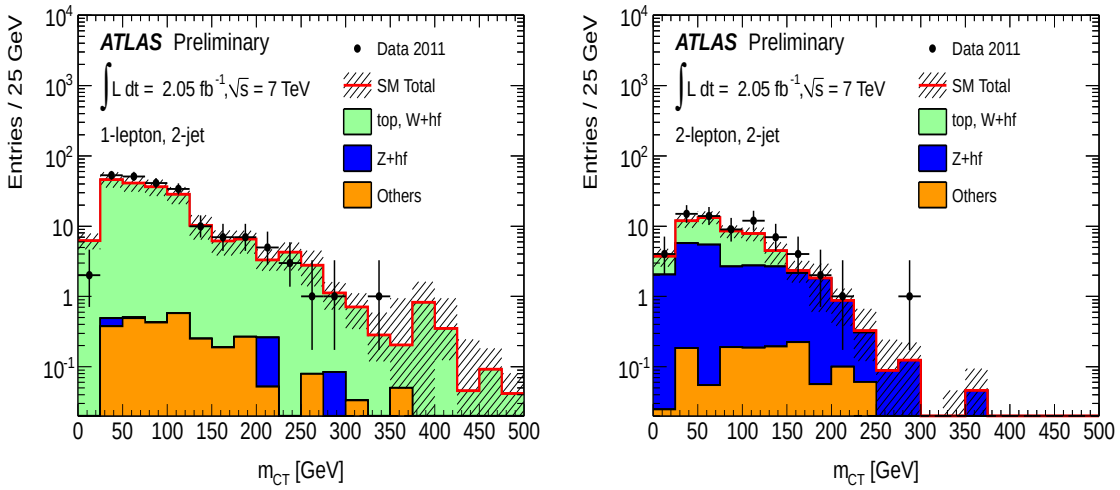

Figure 6.9: The control regions used to estimate the top and $W+b\bar{b}$ (*left*) and $Z+b\bar{b}$ (*right*) are shown. The former is estimated using a 1-lepton control region whilst the latter uses a two lepton control region.

6.5 Results

Table 6.2 reports the observed number of events and the SM predictions before the m_{CT} selection and for each of the signal regions. Both transfer factor and MC estimates are given. The data yields are in good agreement, within uncertainties, with the standard model expectations in all cases.

Figure 6.10 shows the measured m_{CT} and $E_{\mathrm{T}}^{\mathrm{miss}}$ distributions before m_{CT} selection compared to the Standard Model predictions. The distributions are shown for both the inclusive and the exclusive selections. Monte Carlo estimates are used, rescaled to match the total sum predicted by the transfer factor estimates for the Z+$b\bar{b}$ component as well as the sum of top and W+$b\bar{b}$ components. For illustrative purposes a number of possible signal distributions are also shown.

The results are translated into 95% confidence level upper limits on contributions from new physics using the CL_s prescription described in Section 4.7. At every point in the parameter space the m_{CT} cut with the best expected sensitivity is adopted as the nominal result. Figure 6.11 shows the observed and expected exclusion limits

m_{CT} GeV	top, WHF TF-es (MC)	ZHF TF-es (MC)	Others MC+DD	Total SM	Data	Signal Ref. Point
0	67 ± 10 (60 ± 23)	23 ± 8 (16 ± 9)	3.6 ± 1.5	94 ± 16 (80 ± 35)	96	
100	36 ± 10 (34 ± 16)	23 ± 9 (12 ± 7)	3.1 ± 1.6	62 ± 13 (49 ± 25)	56	85
150	12 ± 5 (13 ± 8)	12 ± 6 (8.3 ± 4.7)	2.7 ± 0.9	27 ± 8 (24 ± 13)	28	64
200	3.2 ± 1.6 (4.1 ± 3.4)	3.9 ± 3.2 (2.8 ± 1.5)	1.0 ± 0.9	8.1 ± 3.5 (8.0 ± 4.9)	10	30

Table 6.2: Expected and measured number of events for an integrated luminosity of 2.05 fb^{-1}. The Z+$b\bar{b}$ and the sum of top and W+$b\bar{b}$ are estimated using a transfer factor estimate (TF-es). The column labelled as 'Others' includes the multijet background and other sub-dominant SM backgrounds. For comparison, the numbers obtained using MC samples are shown in parentheses. The expected signal region yields for a reference signal point, with $m_{\tilde{b}_1} = 300$ GeV and $m_{\tilde{\chi}_1^0} = 100$ GeV, are shown.

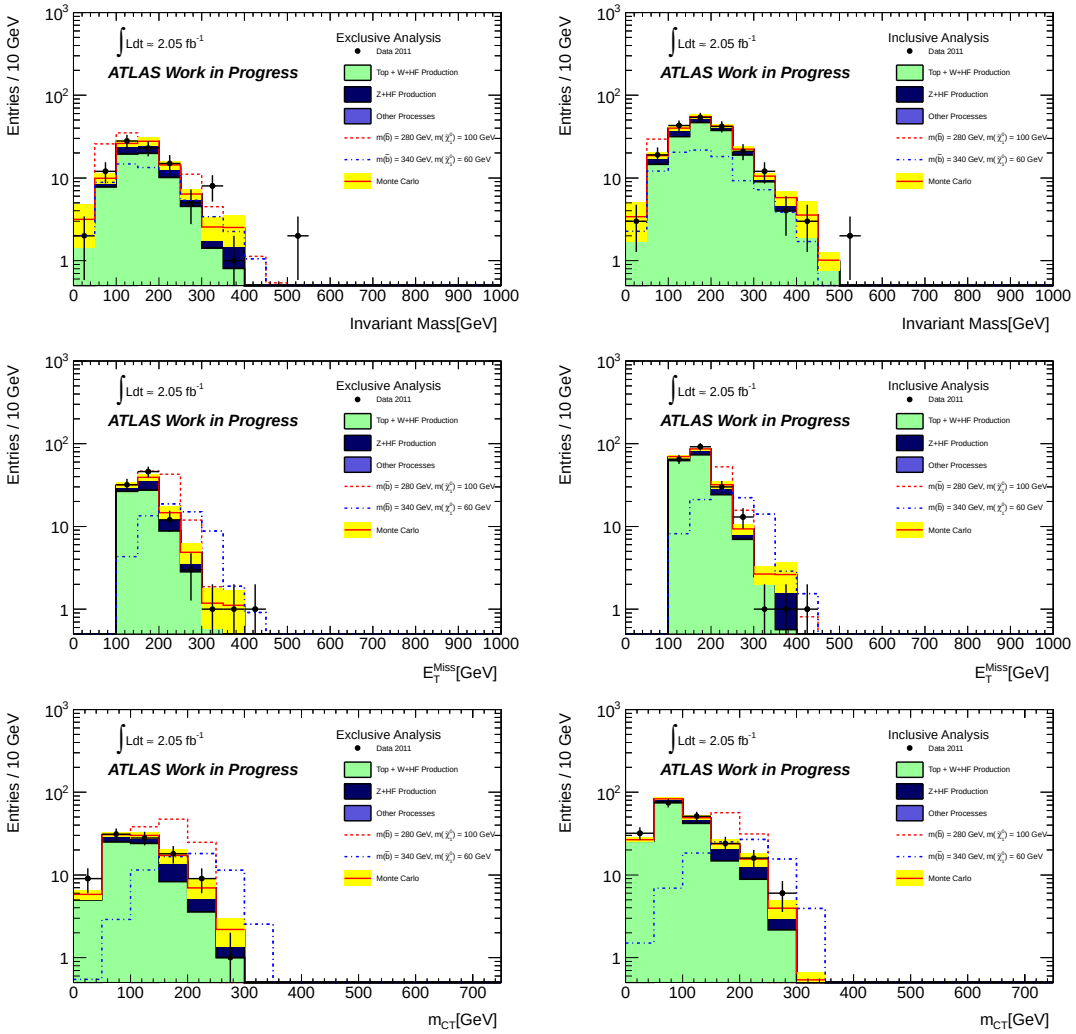

Figure 6.10: The figure shows the invariant mass of the leading two b-jets (*top*), the $E_{\mathrm{T}}^{\mathrm{miss}}$ (*middle*) and the m_{CT} (*bottom*) in the exclusive (*left*) and inclusive (*right*) analyses.

at 95% C.L. in the $(m_{\tilde{b}_1}, m_{\tilde{\chi}_1^0})$ plane. The theoretical uncertainties on the signal yield are not included in the limit calculation itself but instead represented on the limit plot by repeating the limit calculating procedure with a cross section equivalent to the nominal yield plus/minus the theoretical uncertainty. For the MSSM scenarios considered, the quoted upper limit on the sbottom masses is the one derived in the conservative hypothesis, where the expected signal yield corresponds to the nominal

cross section minus the theoretical uncertainty. The limit on $m_{\tilde{b}_1}$ is 350 GeV for a neutralino mass of 120 GeV, increasing to 390 GeV for $m_{\tilde{\chi}_1^0} = 0$. When the nominal cross section is used the limit becomes 405 GeV. The limits are also calculated with

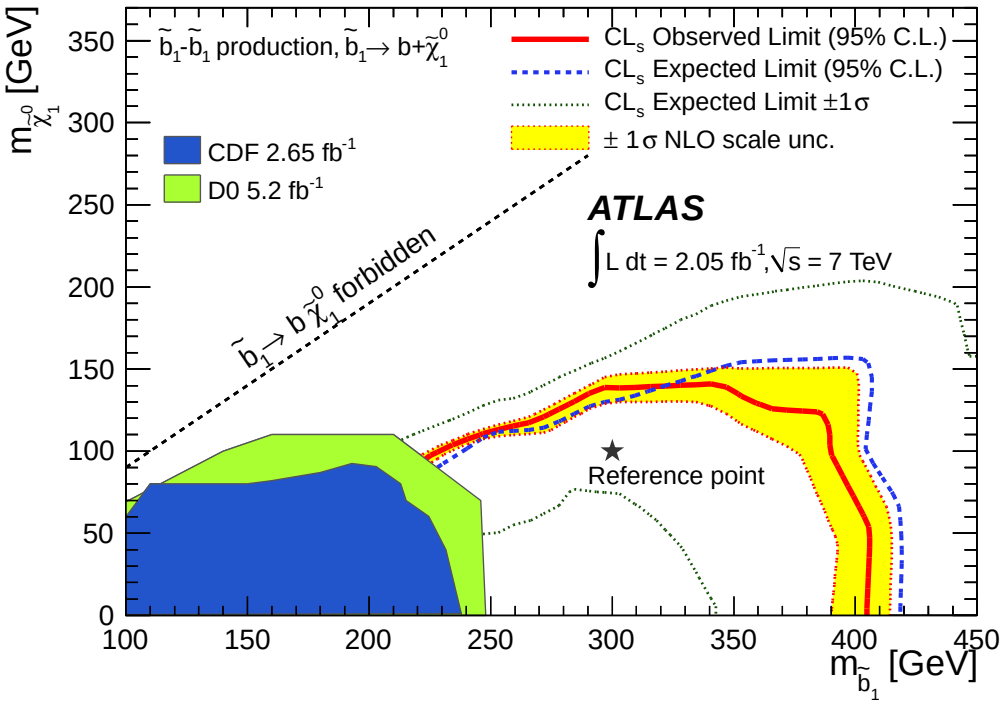

Figure 6.11: Expected and observed exclusion limits, as well as $\pm 1\sigma$ variation on the expected limit, in the $(m_{\tilde{b}_1}, m_{\tilde{\chi}_1^0})$ plane. The yellow band shows the effect of renormalisation and factorisation scale variation. The reference point indicated on the plane corresponds to the MSSM scenario with sbottom and neutralino masses of 300 GeV and 100 GeV, respectively. Results are compared to previous exclusion limits from Tevatron experiments [56, 57].

the theoretical uncertainties handled within the limit setting procedure. The result is shown in Figure 6.12 and is consistent with the conservative scenario shown in Figure 6.11. Both interpretations indicate a substantial improvement over the previous limits from the Tevatron experiments.

The three signal regions are used to set limits on the effective cross section of new physics models, σ_{eff}, including the effects of experimental acceptance and

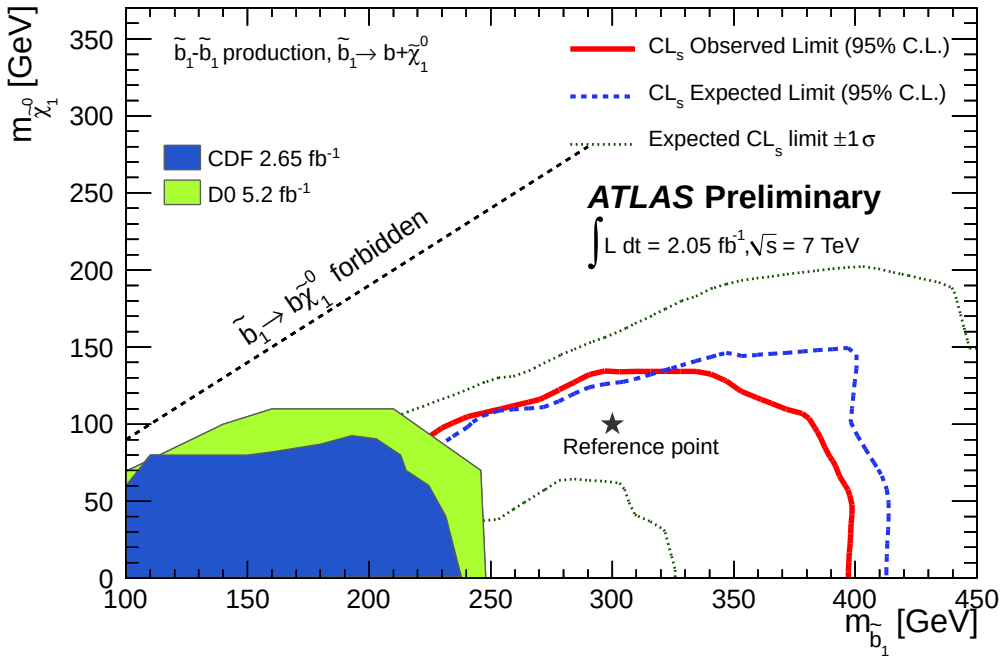

Figure 6.12: Expected and observed exclusion limits, as well as $\pm 1\sigma$ variation on the expected limit, in the $(m_{\tilde{b}_1}, m_{\tilde{\chi}_1^0})$ plane. The effect of renormalisation and factorisation scale variations are folded into the limit setting procedure. The reference point indicated on the plane corresponds to the MSSM scenario with sbottom and neutralino masses of 300 GeV and 100 GeV, respectively. Results are compared to previous exclusion limits from Tevatron experiments [56, 57].

efficiency. In this case no assumptions on the signal model are made and therefore no signal uncertainties are taken into account. The observed (expected) excluded values of the excluded effective cross section, σ_{eff}, at 95% C.L. are 13.4 fb, 9.6 fb and 5.6 fb (15.2 fb, 9.2 fb and 4.7 fb), respectively for $m_{\text{CT}} > 100$, 150, 200 GeV.

6.6 Conclusions

This chapter reports the results of a search for sbottom pair production in pp collisions at $\sqrt{s} = 7$ TeV, based on 2.05 fb^{-1} of ATLAS data. Events with large $E_{\text{T}}^{\text{miss}}$ and two jets required to originate from b-quarks in the final state are selected. The

observed counts are in agreement with SM predictions for backgrounds and translate into 95% C.L. upper limits on sbottom and neutralino masses in a given MSSM scenario for which the exclusive decay $\tilde{b}_1 \to b\tilde{\chi}_1^0$ is assumed. For neutralino masses below 120(60) GeV, sbottom masses up to 350(390) GeV are excluded, significantly extending previous results.

Chapter 7

Gluino-Mediated Sbottom Production

Fuq tlieta toqgħod il-borma

7.1 Analysis Abstract

This chapter discusses a number of searches for sbottoms in events with large missing transverse momentum and heavy flavour jet candidates, in $\sqrt{s} = 7$ TeV proton-proton collisions. In a sequence of datasets corresponding to integrated luminosities of 35 pb^{-1}, 2.05 fb^{-1} and 4.7 fb^{-1}, recorded by the ATLAS experiment, no significant excess is observed with respect to the prediction for Standard Model processes. The results are interpreted within simplified models and phenomenological MSSM scenarios where sbottoms are produced in gluino decay chains.

The work here has been published in [8],[2] and [112] for datasets with different integrated luminosity. The author's contributions include the study of various signal properties and systematics, the generation of signal samples, the analysis optimisation, the estimation of the multijet background and the interpretation of the results. The author also carried out various cross-checks of Monte Carlo background estimates. In order to avoid repetition, the analysis will be described once, with differences resulting from increasing dataset size highlighted.

7.2 Introduction

As outlined in Section 2.4.6, supersymmetry could manifest itself with low mass sbottoms and gluinos. In this case, gluino pair production will come into play along with the direct sbottom pair production described in the previous Chapter. Since the gluino pair production cross section is larger than the sbottom pair production cross section, the former will dominate these supersymmetric events. If one assumes that the sbottom decays exclusively via $\tilde{b}_1 \rightarrow b\tilde{\chi}_1^0$, then the gluinos decay to neutralinos via on-shell or off-shell sbottoms, depending on the mass hierarchy of the gluino and the sbottom. Such a decay hypothesis also means that events contain no leptons, save for those in heavy flavour semi-leptonic decays. Irrespective of whether the sbottom is heavier or lighter than the gluino, this hypothesised signal is expected to result in very busy events, containing 4 b-quarks and 2 neutralinos. The exact kinematics of the events are expected to vary with the values of the gluino, sbottom and neutralino masses.

These considerations are put in the context of a simple phenomenological MSSM model containing only gluinos, sbottoms and neutralinos. The gluino mass is varied between 350 GeV and 1.3 TeV and the sbottom mass runs between 200 GeV and $m_{\tilde{g}} - m_b$. The neutralino mass is fixed to 60 GeV, just above the bounds set by LEP [63]. All other sparticles are set to very high mass, above the production threshold at 7 TeV. The resultant phenomenology is dominated by $\tilde{g}$ pair production but also contains $\tilde{b}_1$ pair production and $\tilde{g}\,\tilde{b}_1$ associated production. Approximately 200

signal points with 20,000 events each are generated using SUSYHIT and HERWIG. This pMSSM model is referred to as the gluino-sbottom model and results are presented in a $(m_{\tilde{g}}, m_{\tilde{b}_1})$ plane.

7.3 Optimisation and Event Selection

A number of preliminary selection cuts can be enforced to increase the signal to background ratio. The exact values of these cuts vary with the integrated luminosity used but in general they include the following:

- Various data quality requirements to ensure that all the detectors are running smoothly and functioning properly.
- Events are triggered using a jet trigger combined with a $E_{\mathrm{T}}^{\mathrm{miss}}$ trigger. This allows for the use of un-prescaled triggers without extremely high leading jet p_{T} thresholds.
- Event and jet cleaning cuts are applied to reduce the effect of calorimeter noise and muons coming from cosmic rays.
- Events containing electrons or muons are vetoed.
- In the first, 35 pb^{-1} analysis, a leading jet with $p_{\mathrm{T}} > 130$ GeV and $E_{\mathrm{T}}^{\mathrm{miss}} > 100$ GeV are required, in order to be in the plateau of the trigger turn on curve. These two cuts were increased in the 2 fb^{-1} and 4.7 fb^{-1} analyses because of higher thresholds on the softest un-prescaled trigger. In the first analysis the leading jet is restricted to be within the η range $|\eta| < 2.5$. This was extended to $|\eta| < 2.8$ in the subsequent analyses. In the 2 fb^{-1} analysis the $E_{\mathrm{T}}^{\mathrm{miss}}$ cut was increased to 130 GeV and in the 4.7 fb^{-1} analysis the cut was placed at 160 GeV.
- At least one sub-leading jet with $p_{\mathrm{T}} > 25$ GeV and $|\eta| < 2.5$. The exact number required was optimised and this procedure is described below. The η

cut was loosened to 2.8 in the 2 fb^{-1} and 4.7 fb^{-1} analyses. In the first analysis the jets are restricted to be within the η range $|\eta| < 2.5$. This was extended to $|\eta| < 2.8$ in the subsequent analyses.

- Cuts on the $\Delta\varphi_{min}$ and the $E_{\mathrm{T}}^{\mathrm{miss}}/m_{\mathrm{eff}}$ ratio are introduced to reduce the multijet contribution.

- At least one b-jet with $p_{\mathrm{T}} > 25$ GeV and $|\eta| < 2.5$. The cut on the b-jet p_{T} was raised to 50 GeV in later analyses to avoid effects coming from pile-up. The b-jet multiplicity required was also increased. The tagger used in the 35 pb^{-1} analysis is SV0, which is switched to JetFitterCOMBNN in the 2 fb^{-1} analysis and MV1 in the 4.7 fb^{-1} analysis.

Table 7.1 shows the breakdown of the different Standard Model contributions after the baseline cuts listed above. Selections with one, two and three sub-leading jets are shown. The yields are normalised to 35 pb^{-1} and all the predictions are based on Monte Carlo samples. The uncertainties include only the statistical component coming from the limited Monte Carlo sample size.

SM process	2-jet	3-jet	4-jet
multijet (PYTHIA MC)	80±30	7.8±4.0	7.7±4.0
W+jets	37.±4.	16.2±1.6	6.3±1.0
Z+jets	18.±3.	6.7±1.5	2.3±0.4
top production	79.±2.	59.8±0.8	40.±0.5
Total	214	90.5	56.3

Table 7.1: Breakdown of SM process background contributions for 2-jet, 3-jet and 4-jet selections. The yields are normalised to 35 pb^{-1} of integrated luminosity. Systematic uncertainties on each SM process type include only statistical uncertainties because of the finite Monte Carlo sample size.

The number of background events is reduced by more than a factor of two when going from a two jet analysis to a three jet analysis. This is mostly driven by a much better rejection of the multijet background, which is dominated by dijet production. Other backgrounds are reduced by around 25% to 50%. Figure 7.1 shows the expected efficiencies for the pMSSM signal considered. The drop in signal efficiency is far lower

than that in the background and hence further optimisation for the 35 pb^{-1} and 2 fb^{-1} analyses is carried out using the three jet selection only.

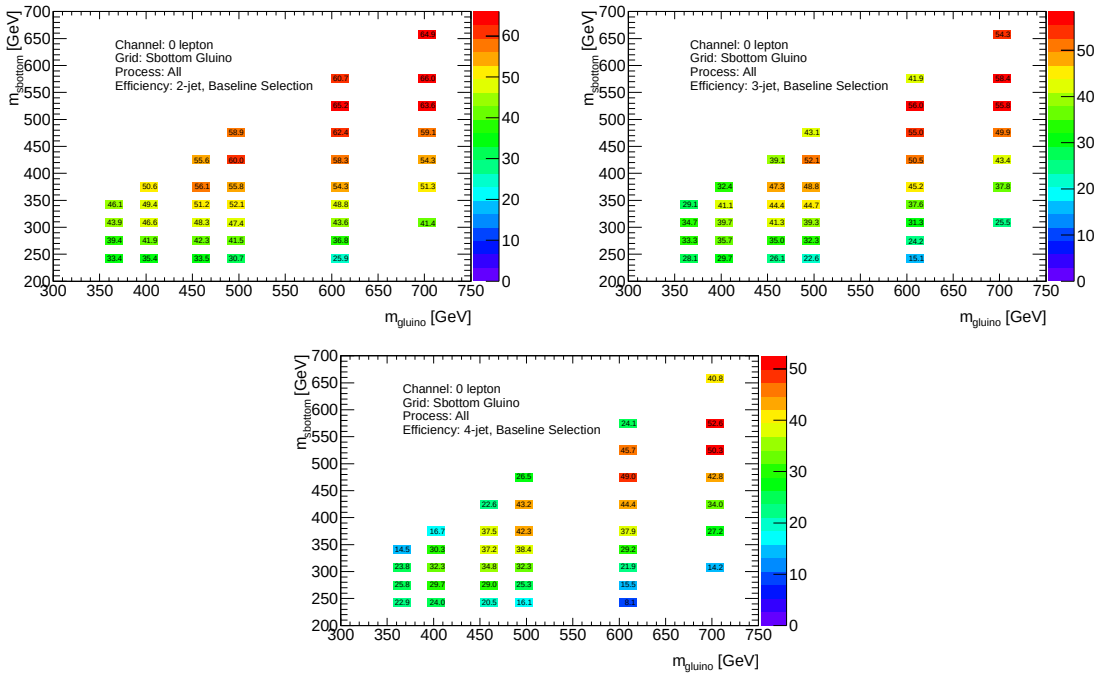

Figure 7.1: Signal Efficiency (in percentage) in the plane of gluino and sbottom masses, after baseline selections requiring two (*top left*), three (*top right*) and four (*bottom*) jets.

The expected distributions of various interesting kinematic quantities, after the three jet baseline selection cuts are applied, are shown in Figure 7.2. These include the jet and b-jet multiplicities, $E_{\mathrm{T}}^{\mathrm{miss}}$, and m_{eff}. The backgrounds are modelled using Monte Carlo and the distributions scaled to 35 pb^{-1} of data. Four different SUSY pMSSM models are shown for reference. As expected, the dominant background is top pair production. This is unchanged throughout the various analyses described in this thesis.

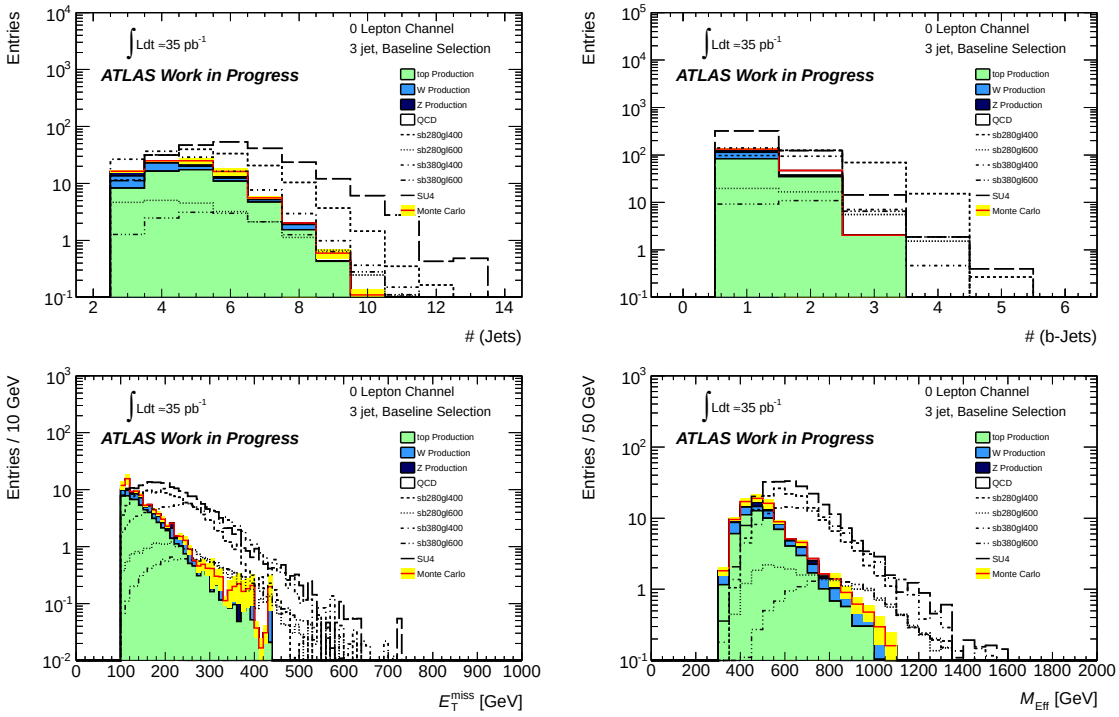

Figure 7.2: Number of jets N_{jets} with p_{T} >20 GeV (*top left*), the number of tagged jets N_{tag} (*top right*), the $E_{\mathrm{T}}^{\mathrm{miss}}$ distribution (*bottom left*), and the m_{eff} (*bottom right*) for SM background processes as estimated from Monte Carlo samples, after the 3-jet baseline selection. Four samples from the signal grid are superimposed for illustration. Also shown is SU4, which is a point in mSUGRA, just outside the Tevatron bounds.

Optimising with m_{eff}

In order to further optimise the analysis, a number of cuts on effective mass are tested. These are applied over and above the baseline three jet selection. To investigate the utility of the various cuts, the expected limits are constructed using preliminary estimates of the uncertainties, with correlations as described in Section 4.6. Figure 7.3 shows that the exclusion limit improves when increasing the m_{eff} threshold from 400 to 700 GeV. Beyond 700 GeV, low statistics and large systematic uncertainties are expected for the first analysis using 35 pb^{-1}, so $m_{\text{eff}} = 600$ GeV is chosen as the optimal cut. Later analyses, with more integrated luminosity, allow for the increase of this cut to higher values.

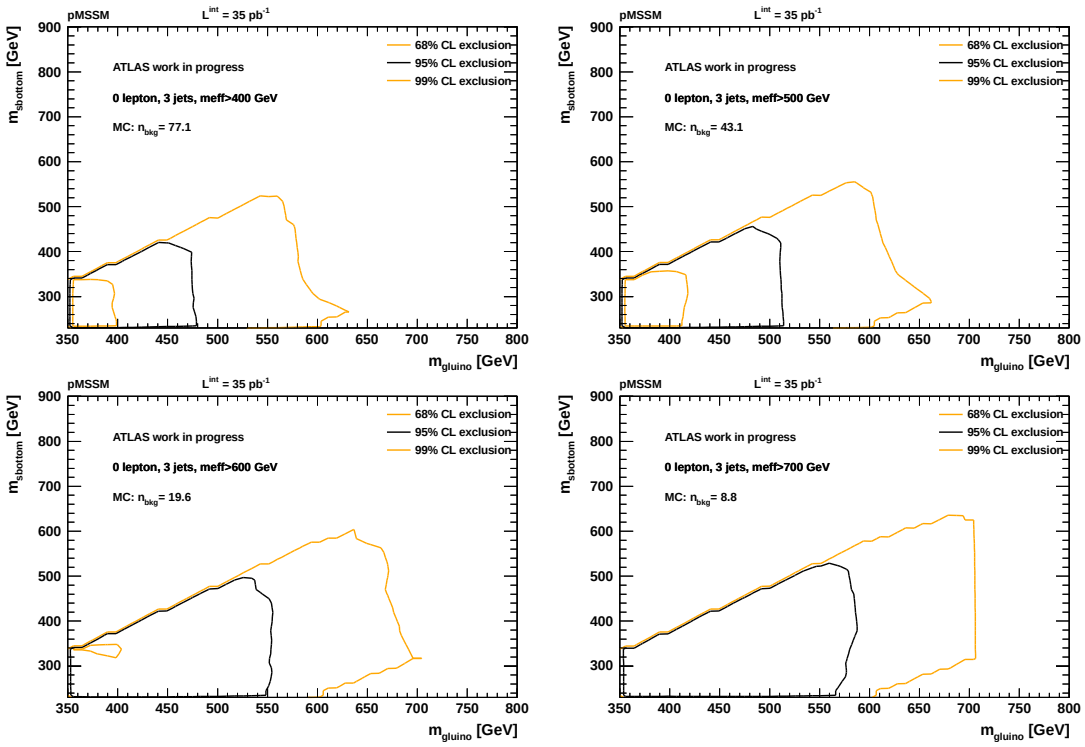

Figure 7.3: Expected exclusion limit plots for gluino-sbottom mass plane for different selections on m_{eff}.

These conclusions are corraborated using a toy discovery significance of $S = \text{Signal}/\sqrt{\text{Background}}$. Figure 7.4 shows the significance for four different m_{eff} cuts

as a function of the gluino (sbottom) mass for a fixed sbottom (gluino) mass. For $m_{\tilde{b}_1}$ =280 GeV, S decreases as the gluino mass increases, because the falling cross section dominates over the harder kinematics. Hard m_{eff} cuts of 600 GeV and 700 GeV are favoured at large $m_{\tilde{g}}$. On the other hand, S is found to be largely independent of the sbottom mass value, since it is the gluino pair production which drives the sensitivity.

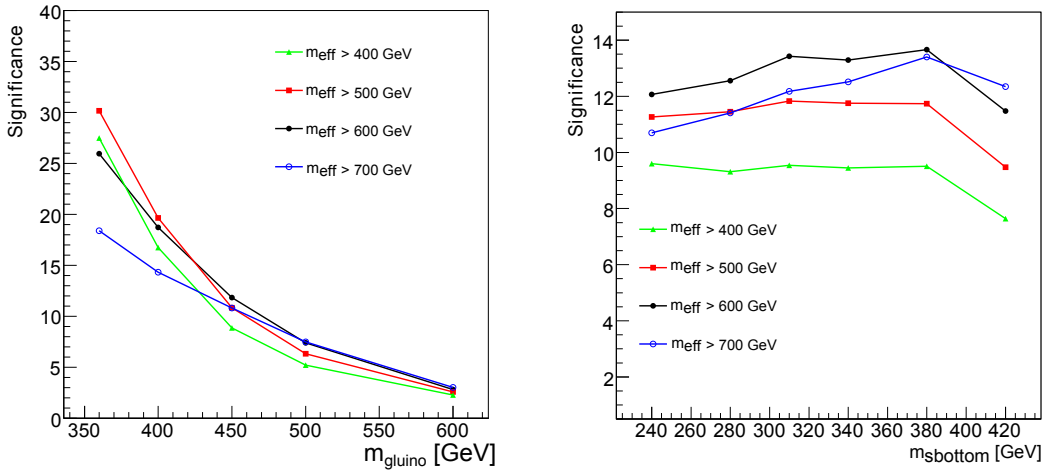

Figure 7.4: $S/\sqrt{B}$ for four different m_{eff} selections are presented at a constant sbottom mass (280 GeV) as a function of the gluino mass (*left*), and at a constant gluino mass (450 GeV) as a function of the sbottom mass (*right*).

The signal efficiencies in the $(m_{\tilde{g}}, m_{\tilde{b}_1})$ plane, after the 600 GeV m_{eff} cut, are reported in Figure 7.5. They are shown separately for the two most relevant processes, gluino pair production and sbottom pair production, and as the sum weighted by each process' NLO cross section. As expected, the analysis is most sensitive to gluino-mediated sbottom production. In this case, efficiencies between 15% and 50% are found, increasing as a function of the gluino mass. For a constant $m_{\tilde{g}}$, lowest efficiency values are found for very large or very small $\Delta M = m_{\tilde{g}} - m_{\tilde{b}_1}$. Efficiencies for sbottom pair production are lowest at low sbottom mass values, mostly due to the fact that such events contain only 2 soft jets.

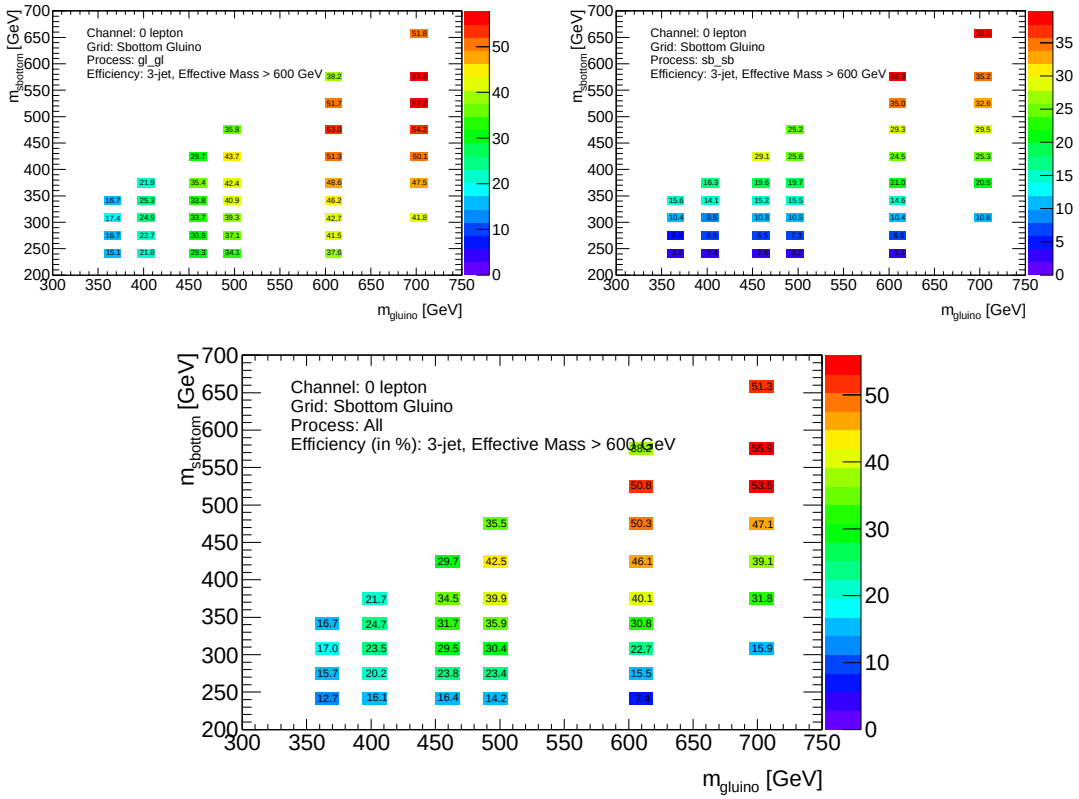

Figure 7.5: Efficiencies (in percentages) for three jet selection and a m_{eff} cut at 600 GeV. The efficiency is shown separately for gluino pair production (*top left*) and sbottom pair production (*top right*). A combined efficiency, weighted by NLO cross section is also shown (*bottom*).

Modifications for Higher Luminosities

The optimisation of the 35 pb^{-1} analysis formed the basis for subsequent, higher luminosity analyses. However, larger datasets allow for tighter cuts, resulting in better signal to background ratios. The approach taken when designing the higher luminosity analyses was to modify the m_{eff} and b-jets multiplicity cuts. Increasing the number of b-jets is clearly beneficial since the signal contains 4 b-quarks, which is more than the SM backgrounds, save for processes such as $t\bar{t}$ produced in association with $b\bar{b}$, which have very small cross sections. In the 2 fb^{-1} analysis, signal regions with at least 2 b-jets are introduced and in the 4.7 fb^{-1} analysis this was increased to 3 b-jets. These larger b-jet multiplicities are feasible in the later datasets because of the higher statistics and the increased understanding of the performance of the b-tagging algorithms. The harder m_{eff} cuts are motivated by the fact that as one explores the higher end of the gluino-mass space, the signal has a progressively harder effective mass spectrum. Due to increasingly higher thresholds on un-prescaled triggers, the $E_{\text{T}}^{\text{miss}}$ and leading jet p_{T} cuts are also increased.

In order to be sensitive to a wider range of spectra in higher luminosity analyses, the softer cuts are retained as separate signal regions. These could be crucial in the regions of the mass plane with low mass splitting, since such areas tend to have less high p_{T} jets. When an analysis makes use of more than one signal region, then for each point on the signal grid the selection resulting in the best expected limit is used. The cuts pertaining to the different analyses will be listed explicitly in the relevant sections. Appendix C contains a table summarising and comparing the cuts used for different integrated luminosities.

7.4 Background Estimation

The background estimation for the 35 pb^{-1} analysis was performed using Monte Carlo. The multijet background was normalized in a multijet enriched control region whilst all other backgrounds were normalized to NLO cross sections. The uncertainties described in Section 4.6 were taken into account.

A transfer factor approach, described in Chapter 6, was used to estimate the dominant top background in 2 fb^{-1} and 4.7 fb^{-1} analyses. This is a semi-data driven approach which uses control regions with low expected yields from the targeted SUSY signals. The method is the same as discussed in Section 6.4.2 and is explained here for completeness. The background estimation in each signal region is obtained by multiplying the number of events observed in the corresponding control region by a transfer factor, defined as the ratio of the MC predicted yield in the signal region to that in the control region:

$$N_{\mathrm{SR}} = \frac{N_{\mathrm{SR}}^{\mathrm{MC}}}{N_{\mathrm{CR}}^{\mathrm{MC}}}(N_{\mathrm{CR}}^{\mathrm{obs}} - N_{\mathrm{CR}}^{\mathrm{res}}) = T_f(N_{\mathrm{CR}}^{\mathrm{obs}} - N_{\mathrm{CR}}^{\mathrm{res}}) \tag{7.1}$$

where $N_{\mathrm{CR}}^{\mathrm{obs}}$ denotes the observed yield in the control region and $N_{\mathrm{CR}}^{\mathrm{res}}$ includes contributions from processes other than $t\bar{t}$ production. The advantage of this approach is that systematic uncertainties that are correlated between the numerator and the denominator of T_f largely cancel out, provided that the event kinematics in the corresponding signal and control region are similar. The multijet component, which makes up a very minor part of the expected background, is estimated using the jet smearing method. Other non-multijet backgrounds are estimated using Monte Carlo.

7.5 Results with 35 pb^{-1}

Table 7.2 gives the expected and observed yields for 35 pb^{-1} in the signal region with m_{eff} larger than 600 GeV. The systematic uncertainties on the non-multijet background are dominated by the Jet Energy Scale uncertainties, which are about 30%

for the $t\bar{t}$ background. The b-tagging uncertainty is the second largest uncertainty and is around 15% for $t\bar{t}$ and 25% for boson plus jets. The b-tagging uncertainty is mostly influenced by fakes, which is why it is less of an issue for top events which contain two real b-quarks. The observed data count is in good agreement with the Standard Model expectation, falling within 1 sigma of the nominal expected yield.

Background	Expected & Observed Yields
$t\bar{t}$ and single top	12.2 ± 5.0
W and Z	6.0 ± 2.0
Multijet	1.4 ± 1.0
Total SM	19.6 ± 6.9
Data	15

Table 7.2: Summary of the expected and observed event yields in the analysis performed using 35 pb^{-1} of data. The multijet background is normalised within a multijet-dominated control region and all other backgrounds are normalised to NLO cross sections.

These results can be interpreted in terms of 95% C.L. exclusion limits in the pMSSM scenario used to optimise the analysis. For this analysis the PCL technique is used. Subsequent analyses described in this chapter use CL_s. In Figure 7.6 the observed and expected exclusion regions are shown in the $(m_{\tilde{g}}, m_{\tilde{b}_1})$ plane of the gluino-sbottom model. All systematic uncertainties on the expected signal and background counts are considered in the construction of the limits. These include the fully correlated detector-type uncertainties as well as the theoretical uncertainties on the signal. Gluino masses below 590 GeV are excluded for sbottom masses up to 500 GeV. The result is compared to previous results from CDF searches [58] which assume the same gluino-sbottom decay hypotheses, a neutralino mass of 60 GeV and $m_{\tilde{q}_{1,2}} = 500$ GeV, which is much larger than the gluino mass in the Tevatron's kinematic range. Exclusion limits from the CDF and D0 experiments on direct sbottom pair production [56, 57] are also reported. These limits depend weakly, via the dependence of the production cross section for $\tilde{g}\tilde{g}$ production, on the masses of the first and second generation squarks. This dependence is highlighted is Figure 7.7. Variations of these masses in the range between $\sim$3 TeV and $2 \cdot m_{\tilde{g}}$ reduce the excluded mass region by less than 20 GeV, as shown in Figure 7.8. This is in fact a conservative

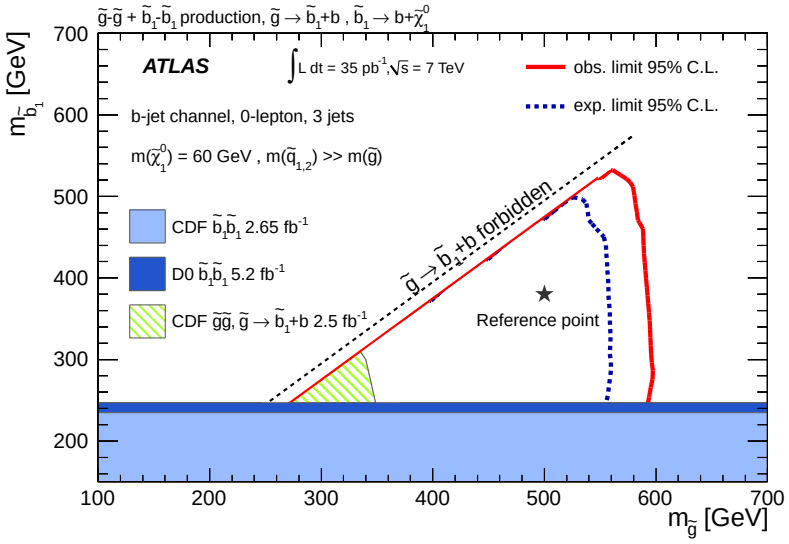

Figure 7.6: Observed and expected 95% C.L. exclusion limits obtained using 35 pb^{-1} in the $(m_{\tilde{g}}, m_{\tilde{b}_1})$ plane. The neutralino mass is assumed to be 60 GeV and the NLO cross sections are calculated in the hypothesis of $m_{\tilde{q}_{1,2}} \gg m_{\tilde{g}}$. The result is compared to previous results from CDF [58] searches which assume the same gluino-sbottom decay hypotheses. Exclusion limits from the CDF [56] and D0 [57] experiments on direct sbottom pair production are also shown.

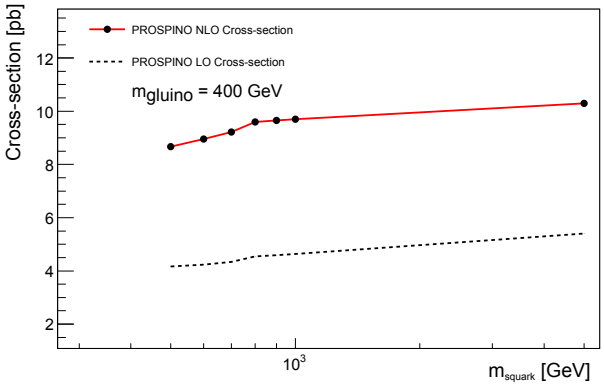

Figure 7.7: Dependence of the gluino cross section on the mass of the first and second generation squarks.

number, as such a reduction of the squark mass would also result in $\tilde{q} - \tilde{q}$ pair production contributing to the signal yield. Due to this weak dependence, all subsequent results are shown in the $m_{\tilde{q}_{1,2}} \gg m_{\tilde{g}}$ hypothesis only.

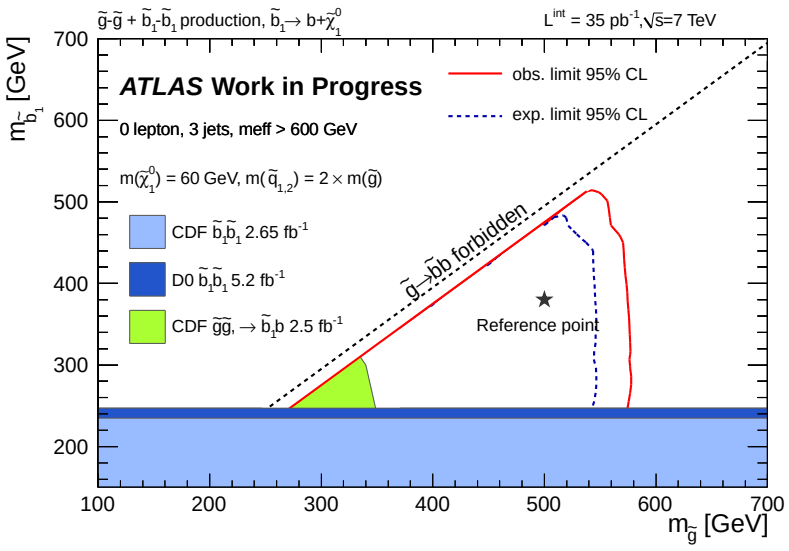

Figure 7.8: Observed and expected 95% C.L. exclusion limits, as obtained using 35 pb^{-1}, in the $(m_{\tilde{g}}, m_{\tilde{b}_1})$ plane. The neutralino mass is assumed to be 60 GeV and the NLO cross sections are calculated in the hypothesis of $m_{\tilde{q}_{1,2}} = 2 \cdot m_{\tilde{g}}$. The result is compared to previous Tevatron limits, as per Figure 7.6.

7.6 Results with 2 fb^{-1}

7.6.1 Signal Regions

The instantaneous luminosity increased drastically in 2011 and by July ATLAS had collected around 2 fb^{-1} of data, 60 times more than what was recorded in 2010. The increased dataset size allowed for the introduction of harder cuts on the number of b-jets and the m_{eff}. Figure 7.9 shows the significance, defined as Signal/$\sqrt{\text{Background}}$, in the gluino-sbottom pMSSM model, calculated using a variety of m_{eff} and b-jet multiplicity cuts. The figure shows selections with ≥ 1 and ≥ 2 b-jets as well as m_{eff} cuts of 500 and 900 GeV. The introduction of tighter signal regions is justified by the increase in sensitivity obtained using a ≥ 2 b-jet requirement and higher m_{eff}.

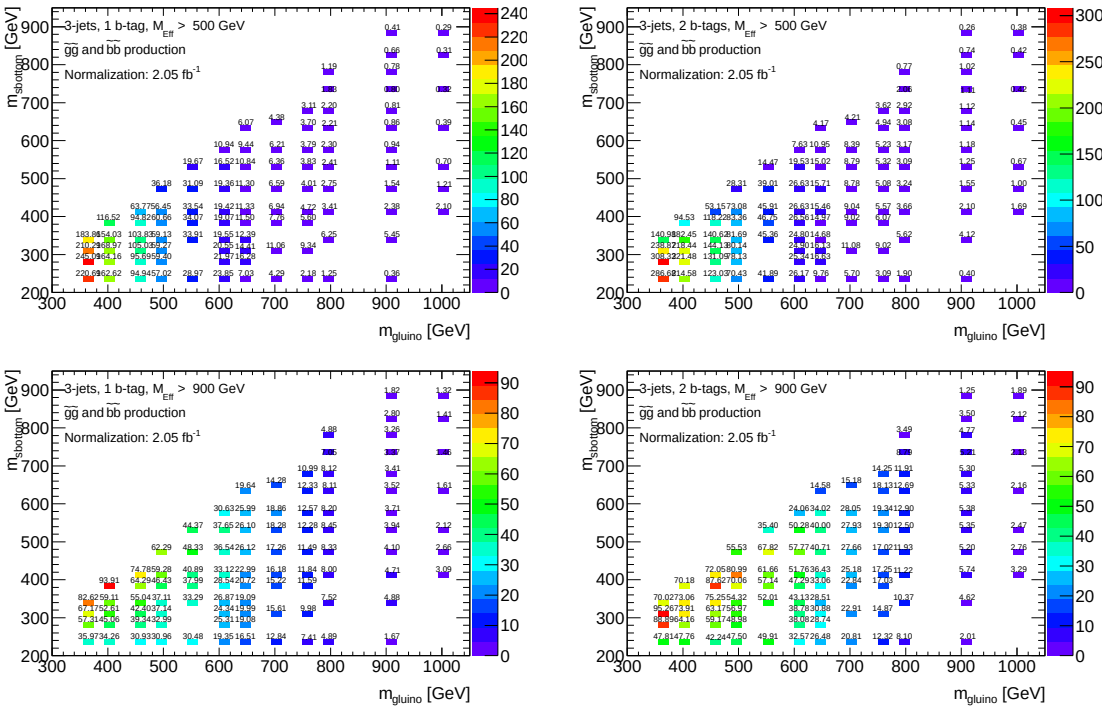

Figure 7.9: Significance in the Sbottom-Gluino grid of the 1 b-tag (*left*) and 2 b-tags (*right*) with $m_{\text{eff}} > 500$ GeV (*top*) and $m_{\text{eff}} > 900$ GeV (*bottom*).

The same conclusions hold when using a signal sample where the $\tilde{b}_1$ quark is

heavier than the gluino. In this case sbottom pair production is completely negligble and gluino pair production is the only allowed production mode. Gluinos decay into three-body final states ($b\bar{b}\tilde{\chi}_1^0$) via an off-shell sbottom. This hypothesis, having only one production process, is considered a simplified model. A plane in $(m_{\tilde{g}}, m_{\tilde{\chi}_1^0})$ is defined, with a fixed large sbottom mass. This can be considered complementary to the pMSSM model defined in the $(m_{\tilde{g}}, m_{\tilde{b}_1})$ plane with fixed $\tilde{\chi}_1^0$ mass. This model is henceforth referred to as the gluino-neutralino simplified model. Validating the conclusions in this scenario ensures that we minimise the dependence of the analysis on the mass hierarchy of the gluinos and sbottoms. In all, six signal regions are retained and are labelled as shown in Table 7.3. The numerical index reflects the number of b-jets required and the letters A, B and C represent tightening m_{eff} cuts of 500 GeV, 700 GeV and 900 GeV.

# b-jets	$m_{\text{eff}} > 500$ GeV	$m_{\text{eff}} > 700$ GeV	$m_{\text{eff}} > 900$ GeV
$\geq$1 b-tag	SR-A1	SR-B1	SR-C1
$\geq$2 b-tag	SR-A2	SR-B2	SR-C2

Table 7.3: The signal region definitions used for the 2 fb^{-1} analysis. The numerical index reflects the number of b-jets required and the letters A, B and C represent tightening m_{eff} cuts of 500 GeV, 700 GeV and 900 GeV.

7.6.2 Background Estimation

Non-Multijet Background

The non-multijet background is estimated using control regions and transfer factors. Two control regions with ≥ 1 b-jet (CR-1) and ≥ 2 b-jets (CR-2) are defined to estimate the top background, differing only in the number of b-jets required. They are obtained by applying the same thresholds on the three jets and $E_{\text{T}}^{\text{miss}}$ as in the signal region, but also require exactly one isolated electron or muon. The transverse mass constructed using the lepton and the $E_{\text{T}}^{\text{miss}}$ is required to be in the range 40 GeV$<$ $m_{\text{T}} < 100$ GeV and the effective mass m_{eff} cut is set at 600 GeV. The region CR-1 is

used to estimate the top background in SR-A1, SR-B1 and SR-C1 and CR-2 is used in the signal regions requiring ≥ 2 b-jets. All other non-multijet backgrounds are estimated using Monte Carlo simulation, normalised to NLO cross sections.

Multijet Background

The multijet background was estimated using the jet smearing method. The details of the method are given in Chapter 5. Points relevant to this particular analysis are outlined below.

Recall that the pseudoevents need to be normalised in a control region. In this analysis, the control region is constructed by reversing the $\Delta\varphi_{min}$ cut so that $\Delta\varphi_{min}(\text{jets}_{1,2,3} - E_{\text{T}}^{\text{miss}}) < 0.4$. A single b-jet is required for the control region used to normalise the estimates in the 1 b-tag regions, whilst 2 b-jets are required for the control region used to normalise the estimates in the 2 b-tag regions. The kinematics of the data are reasonably well reproduced in these control regions, and this can be seen in Figure 7.10.

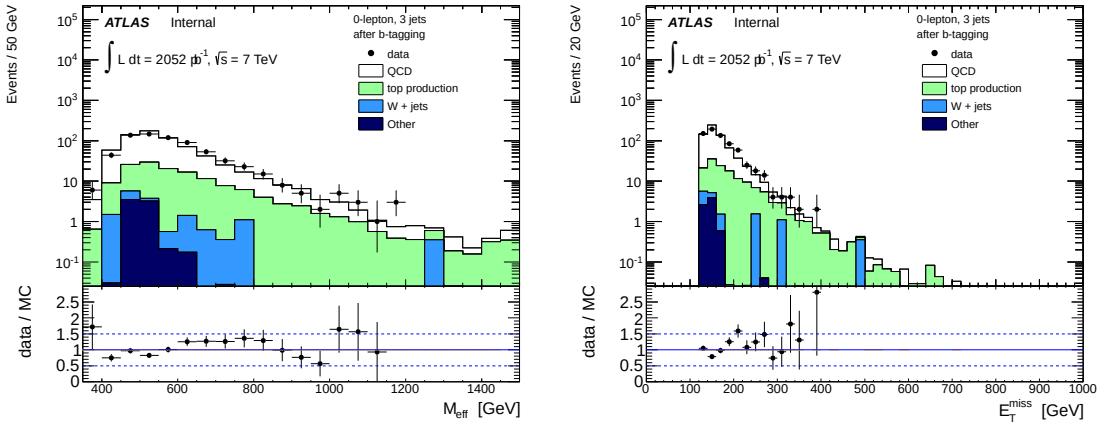

Figure 7.10: The effective mass (*left*) and the $E_{\text{T}}^{\text{miss}}$ (*right*) in the 1 b-tag control region used to normalise the smeared events.

Table 7.4 shows the estimates of the multijet background in the various signal regions, including both the nominal and the LAr multijet contributions. The total

multijet estimate is always less than 5% of the total expected background in the signal region.

Selection	Nominal Multijet	LAr Multijet	Total
1 b-tag, $m_{\text{eff}} > 700$ GeV	48.7	1.0	49.7
1 b-tag, $m_{\text{eff}} > 700$ GeV	3.8	0.2	4.0
1 b-tag, $m_{\text{eff}} > 900$ GeV	0.4	0.04	0.44
2 b-tags, $m_{\text{eff}} > 500$ GeV	14.0	0.5	14.5
2 b-tags, $m_{\text{eff}} > 700$ GeV	1.3	0.04	1.34
2 b-tags, $m_{\text{eff}} > 900$ GeV	0.2	0.01	0.21

Table 7.4: Estimate of the multijet background for 2 fb^{-1} using the jet smearing method. Both the nominal and LAr multijet contributions are shown.

7.6.3 Results

The m_{eff} and $E_{\text{T}}^{\text{miss}}$ distributions are shown in Figure 7.11 for SR-A1 and SR-A2, which are inclusive of the regions which cut tighter on m_{eff}. The shape of the $t\bar{t}$ background is taken from Monte Carlo but is normalised to the yield given by the transfer factor method. Table 7.5 shows the Standard Model background predictions and the observed number of events in all the signal regions. The total number of predicted Standard Model events is in good agreement with the number of observed data in all six signal regions.

7.6.4 Interpretation

Figure 7.12 shows the exclusion limits at 95% C.L. in the gluino-sbottom pMSSM model. For the expected and observed exclusion limits, at each point, the signal region providing the best expected exclusion limit is used. The selection SR-2C, being the tightest, provides the best sensitivity in most cases. If $\Delta M = m_{\tilde{g}} - m_{\tilde{b}_1} < 100$ GeV, softer signal regions are preferred, due to the lower number of expected b-jets above

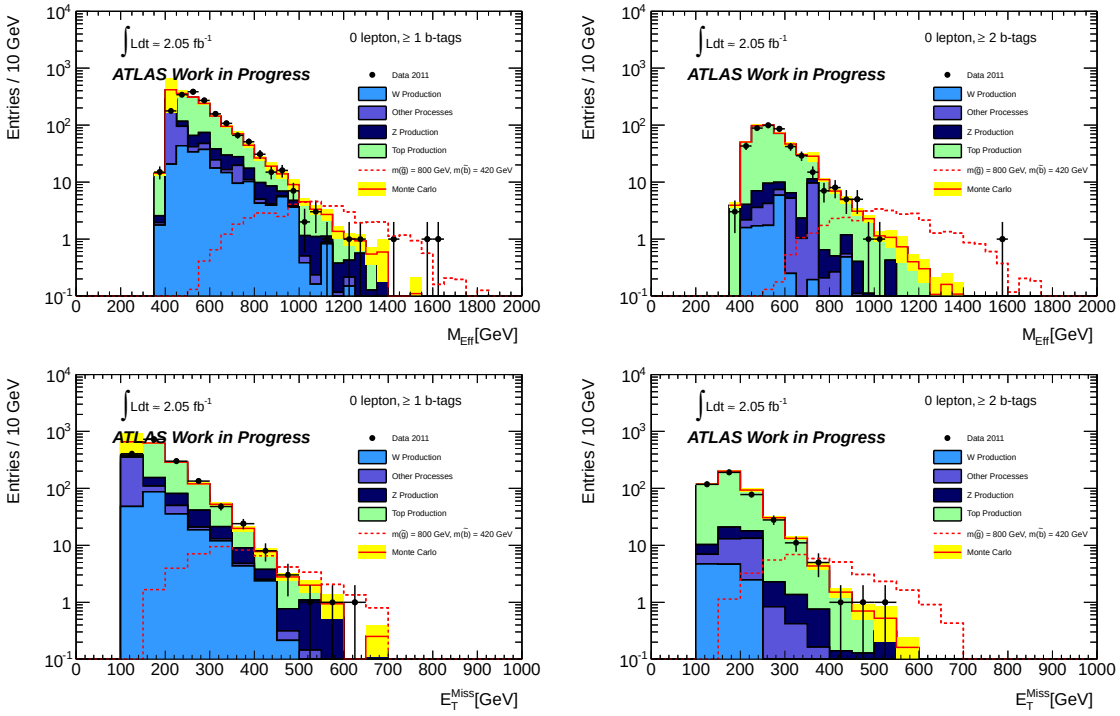

Figure 7.11: Distribution of the effective mass (*top*) and $E_{\mathrm{T}}^{\mathrm{miss}}$ (*bottom*) in $\geq 1\,b$-tag region (*left*) and the $\geq 2\mathrm{b}-tag$ region (right). Only statistical uncertainties are shown. A signal point from the gluino-sbottom grid is shown for comparison.

p_{T} thresholds. Regions SR1-A and SR2-A provide the best sensitivity for MSSM scenarios where $m_{\tilde{g}} \gg m_{\tilde{b}_1}$. Here sbottom pair production plays a more important role due to the lower gluino cross sections at very high gluino masses. Gluino masses below 910 GeV are excluded for sbottom masses up to 800 GeV. The exclusion is less stringent in the region with small mass splitting because of lower signal efficiency in this area of the plane. These values constitute a significant improvement over the previous results derived by ATLAS, discussed in the previous section, as is clear from the figure.

Results are also interpreted in the gluino-neutralino simplified model. Figure 7.13 shows the expected and observed exclusion limits at 95% C.L. for this topology. Since gluino pair production is the only allowed supersymmetric production mode in this model, we also show the maximum allowed cross section for this pro-

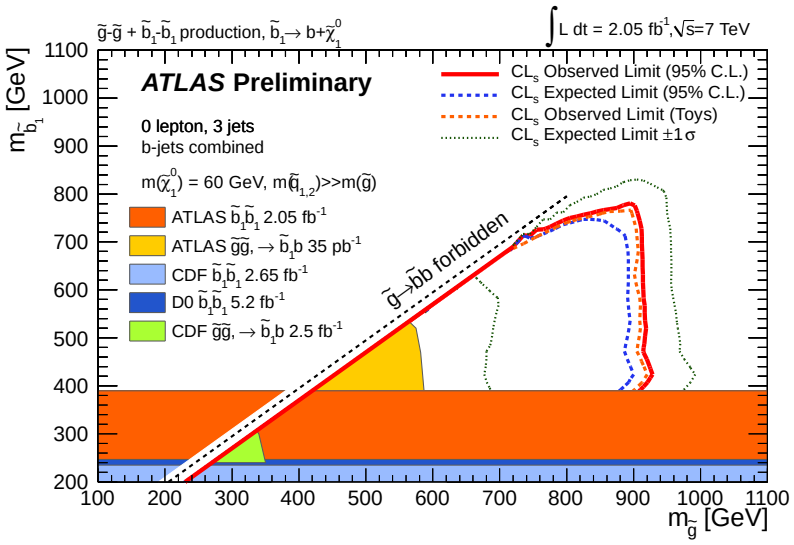

Figure 7.12: Observed and expected 95% C.L. exclusion limits in the $(m_{\tilde{g}}, m_{\tilde{b}_1})$ plane. For each scenario, the signal region providing the best expected limit is chosen. The neutralino mass is assumed to be 60 GeV. The result is compared to previous results from ATLAS [8] and CDF [58] searches which assume the same gluino-sbottom decay hypotheses. Exclusion limits from the CDF [56], D0 [57] and ATLAS [3] experiments on direct sbottom pair production are also shown.

SR	Top	W/Z	multi-jet/ di-boson	Total	Data
SR0-A1	705 ± 110 (725)	248 ± 150	53 ± 21	1000 ± 180	1112
SR0-B1	119 ± 26 (122)	67 ± 42	7.3 ± 4.7	190 ± 50	197
SR0-C1	22 ± 8 (22)	16 ± 11	1.5 ± 1	39 ± 14	34
SR0-A2	272 ± 65 (212)	23 ± 15	21 ± 12	316 ± 72	299
SR0-B2	47 ± 10 (37)	4.5 ± 3	2.8 ± 1.7	54 ± 11	43
SR0-C2	8.5 ± 3 (6.6)	0.8 ± 1	0.5 ± 0.4	9.8 ± 3.2	8

Table 7.5: Summary of the expected and observed event yields corresponding to 2 fb^{-1} in the six signal regions. The errors quoted for all background processes include all the systematic uncertainties discussed in the text. The numbers in parentheses in the "Top" column are the yields predicted by the MC simulation.

cess at each point $(m_{\tilde{g}}, m_{\tilde{\chi}_1^0})$ mass plane. Assuming the gluino pair production cross sections of the MSSM, gluino masses of up to 920 GeV are excluded for neutralino masses of around 300 GeV. The limit is fairly flat in $\tilde{\chi}_1^0$ mass, as falling gluino cross section is countered by an increase in the $\tilde{g}$-$\tilde{\chi}_1^0$ mass splitting. Contours of equal allowed cross section are diagonal, along the lines of equal mass splitting. This reflects the fact that the mass splitting is the strongest driver of kinematics and signal efficiencies.

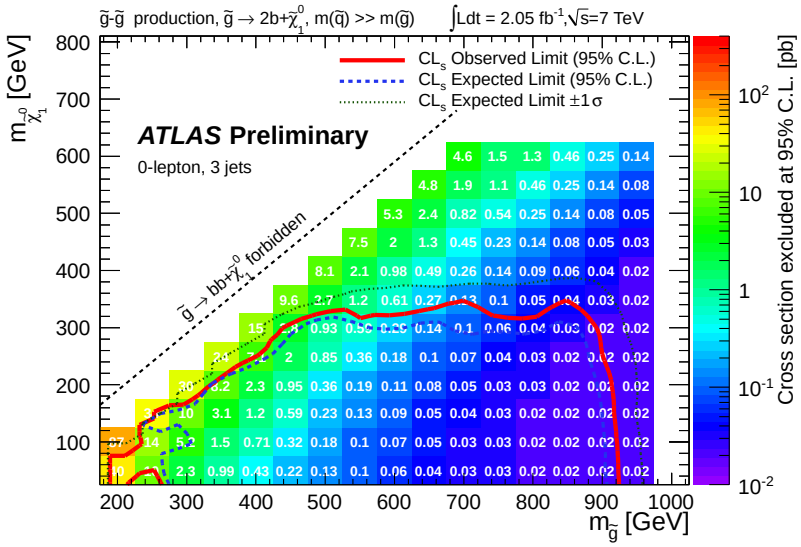

Figure 7.13: Observed and expected 95% C.L. exclusion limits in the gluino-neutralino simplified model. The limit curves assume MSSM cross sections calculated at NLO. The upper limits at each point indicate the maximum allowed cross section for any new physics process with kinematics similar to the gluino-neutralino model.

7.7 Results with 4.7 fb^{-1}

7.7.1 Signal Regions

When analysing the full 2011 dataset, comprising 4.7 fb^{-1}, two major changes were made in the definitions of the signal regions. The $E_{\mathrm{T}}^{\mathrm{miss}}$ cut was increased to 160 GeV, to cope with the larger threshold on the lowest un-prescaled trigger, and the required b-jet multiplicity was increased to 3 b-jets. Three signal regions, referred to as loose, medium and tight, are defined. The MV1 tagger is used and the operating point used to define a b-jet is set to either 60% or 70%, depending on the signal region. The various cuts pertaining to each of the 3 regions are shown in Table 7.6.

Common selection: 4j,$p_T > 50$ GeV, lepton veto, $E_{\mathrm{T}}^{\mathrm{miss}}, p_T^{j_1} > 160$ GeV $E_{\mathrm{T}}^{\mathrm{miss}}/m_{eff} > 0.2$, $\Delta\varphi(E_{\mathrm{T}}^{\mathrm{miss}}, j_{1,2,3}) > 0.4$		
Signal Region	b-jets	m_{eff} cut
loose	≥ 3 b-jets, $p_T > 30$ GeV, OP = 60%	500 GeV
medium	≥ 3 b-jets, $p_T > 30$ GeV, OP = 70%	700 GeV
tight	≥ 3 b-jets, $p_T > 30$ GeV, OP = 70%	900 GeV

Table 7.6: Definition of the signal regions in the three b-jet analysis, carried out with 4.7 fb^{-1}.

7.7.2 Background Estimation

Multijet Background

The multijet background is again estimated using the jet smearing technique. The normalisation of the smeared events is carried out in a reversed $\Delta\varphi_{min}$ region. To increase the statistics the $E_{\mathrm{T}}^{\mathrm{miss}}/m_{\mathrm{eff}}$ cut is relaxed. Figure 7.14 shows the m_{eff} and $E_{\mathrm{T}}^{\mathrm{miss}}$ in the control region. Despite the low statistics, the kinematics of the jet smearing reproduces the observed data fairly well.

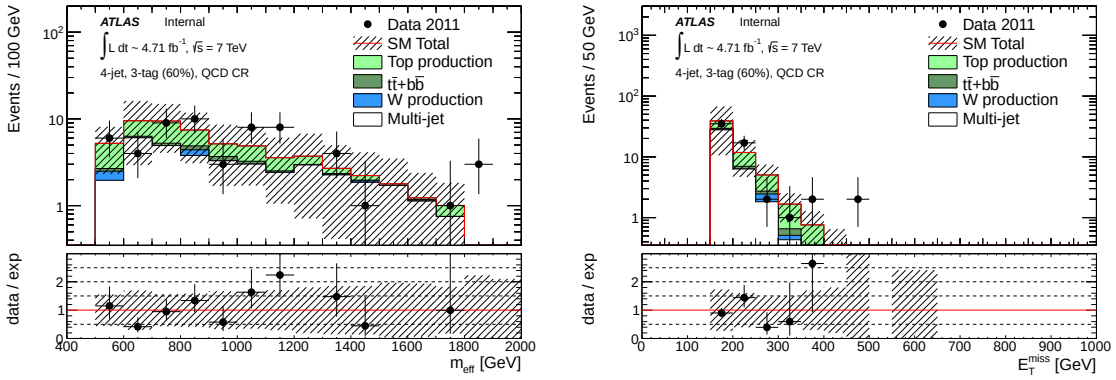

Figure 7.14: The effective mass (*left*) and the $E_{\mathrm{T}}^{\mathrm{miss}}$ (*right*) in the 3 b-tag control region used to normalise the smeared events.

Non-Multijet Background

The dominant reducible background process in the 3 b-jets signal regions is $t\bar{t}$ production in the semi-leptonic channel where a c-quark or a τ arising from a W boson decay is mistagged as a b-jet. This background is estimated using control regions and transfer factors. Since different operating points are used to define what constitutes a b-jet in the signal regions, two control regions are defined, varying only in the operating point used to tag b-jets. The control regions are constructed by applying the same jet requirements as in the signal regions, but requiring exactly two b-jets. The m_{eff} requirement is also reduced to 500 GeV, in order to minimize the signal contamination. The definition of the control regions is summarised in Table 7.7. The main systematic uncertainty on the predicted number of top events is the b-tagging uncertainty. This is because the additional b-jet required when counting events in the numerator of the transfer factor results in a discrepancy between the signal and control region composition, which reduces the amount of systematic uncertainty cancellation obtained.

In the 4.7 fb^{-1} analysis, the yield in the top control regions is incorporated into the likelihood used to calculate the limit. A free parameter, μ_{Top}, is introduced into the fit as a $t\bar{t}$ strength parameter. The top content in the signal region is estimated by simultaneously fitting the control and signal regions within the profile likelihood

calculation. The expected counts for the other backgrounds are fixed. The statistical and systematic uncertainties on the expected values in the control region are included in the likelihood as nuisance parameters, in the same way the uncertainties on the signal region expectations are handled. The correlations between uncertainties in the control and signal regions are taken into account where necessary. The fitted value of μ_{Top} is consistent with 1 and the main impact of the data-driven estimate is a reduction in the uncertainty by approximately a factor of two.

Common selection: 4j,$p_T > 50$ GeV, lepton veto, $E_{\mathrm{T}}^{\mathrm{miss}}, p_T^{j_1} > 160$ GeV $E_{\mathrm{T}}^{\mathrm{miss}}/m_{eff} > 0.2$, $\Delta\varphi(E_{\mathrm{T}}^{\mathrm{miss}}, j_{1,2,3}) > 0.4$, $m_{eff} > 500$ GeV		
CR cuts	b-jets	corresponding SR
CR-4j-OP60	=2 b-jets, $p_T > 30$ GeV, OP = 60%	loose, medium
CR-4j-OP70	=2 b-jets, $p_T > 30$ GeV, OP = 70%	tight

Table 7.7: Definition of the control regions used to estimate the $t\bar{t}$ background.

The major irreducible background is $t\bar{t}$ production in association with heavy flavour jets. This and other non-multijet backgrounds are estimated using Monte Carlo simulation, normalised to NLO cross sections.

7.7.3 Results

Figure 7.15 shows the distribution of the m_{eff} in the loose and tight signal regions and Table 7.8 shows the expected and observed yields. Good agreement is found between the observed data counts and the expected Standard Model predictions.

7.7.4 Interpretation

The expected and observed 95% C.L. exclusion limits in the gluino-sbottom and gluino-neutralino models are shown in Figure 7.16. All uncertainties, including the theoretical uncertainties on the signal, are folded into the limit calculation. In the

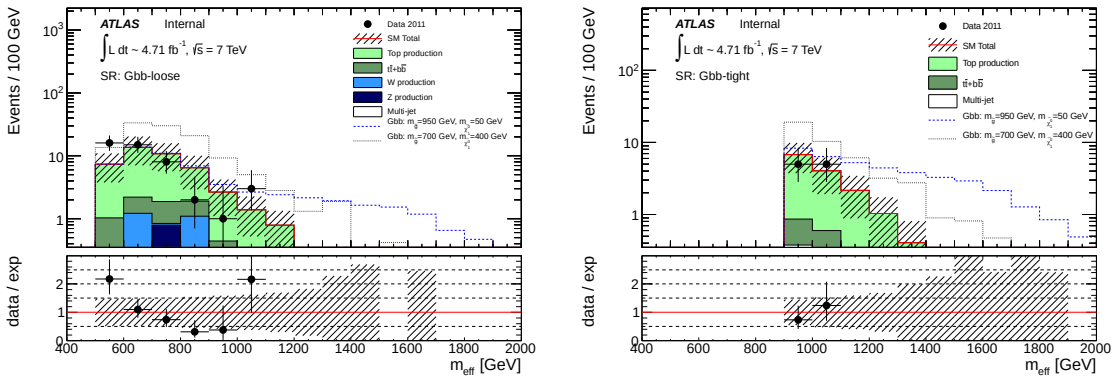

Figure 7.15: Distribution of m_{eff} for the loose (*left*) and tight (*right*) signal regions. The hatched band shows the systematic uncertainty on the MC prediction. The label "others" includes the contributions from single top, $t\bar{t}+b\bar{b}$, $t\bar{t}+W/Z$, W/Z+jets and multi-jet processes. Two signal points, taken from the gluino-neutralino simplified models grid, are overlaid.

Signal region.	$t\bar{t}$	others	SM prediction	data (4.7 fb^{-1})
loose	33.3 ± 8.0	11.2 ± 5.1	44.5 ± 9.7	45
medium	16.4 ± 4.1	6.7 ± 3.0	23.1 ± 5.4	14
tight	9.7 ± 2.1	3.7 ± 1.9	13.3 ± 2.8	10

Table 7.8: Comparison of the expected background yield for 4.7 fb^{-1} in the 3 signal regions. The column "others" includes the contributions from single top, $t\bar{t}$ $+b\bar{b}$, $t\bar{t}$ +EW, W/Z+jets and multi-jets processes.

gluino-sbottom model, gluino masses below 1060 GeV are excluded for sbottom masses up to about 880 GeV. In the gluino-neutralino model, gluino masses below 1060 GeV are excluded for neutralino masses up to 500 GeV. In both cases the limit gets weaker closer to the diagonal, where smaller mass differences result in softer events.

The interpretation can also be repeated with the theoretical uncertainties on the signal removed from the limit calculation, as described in Section 6.5. Three limit curves are shown, corresponding to the the nominal signal cross section and the variations around this nominal using $\pm\sigma^{\text{SUSY}}_{\text{Theory}}$. These results can be seen in Figure 7.17 For the gluino-sbottom model, gluino masses below 1000 GeV are excluded for sbottom masses up to about 870 GeV using the most conservative $-1\sigma^{\text{SUSY}}_{\text{Theory}}$ hypothesis. Taking the conservative curve in the gluino-neutralino model results in an exclusion of gluino masses below 1020 GeV for neutralino masses up to about 400 GeV .

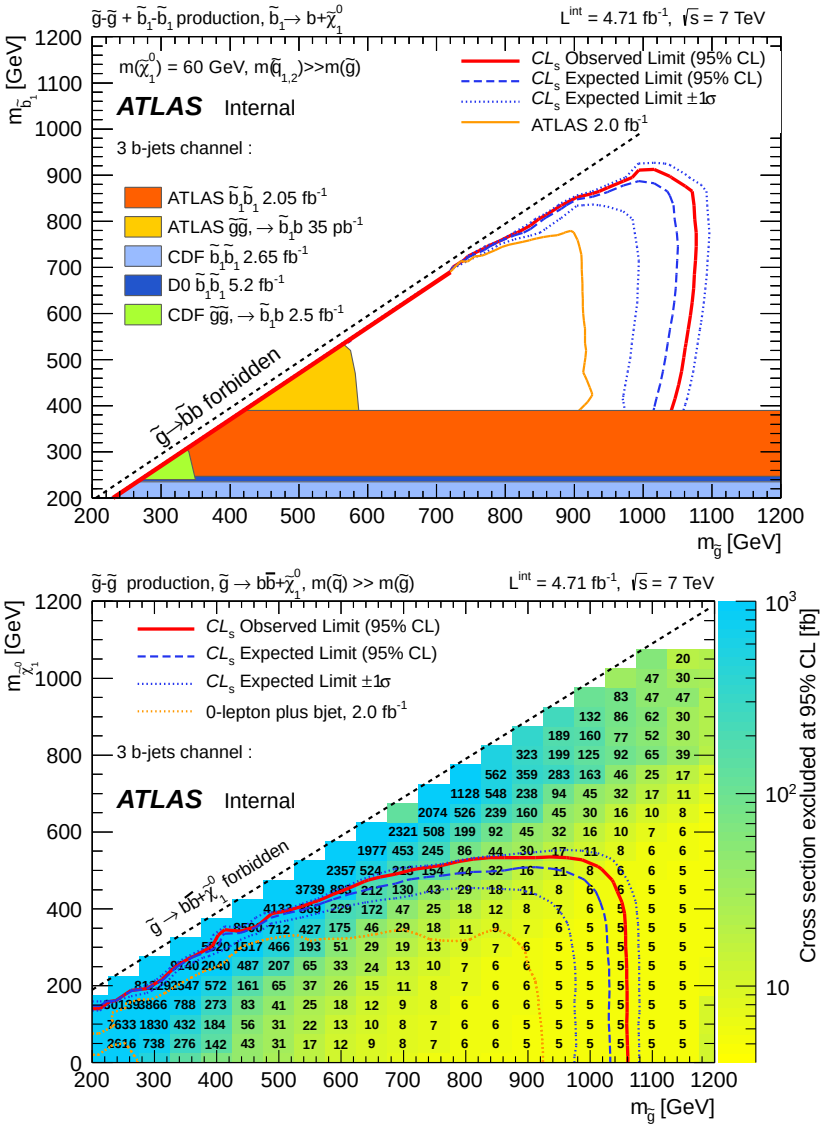

Figure 7.16: Expected and observed exclusion limits at 95% C.L. in the $(m_{\tilde{g}}, m_{\tilde{b}_1})$ plane (*top*) and in the $(m_{\tilde{g}}, m_{\tilde{\chi}_1^0})$ plane (*bottom*). The theoretical uncertainties are folded into the limit calculation.

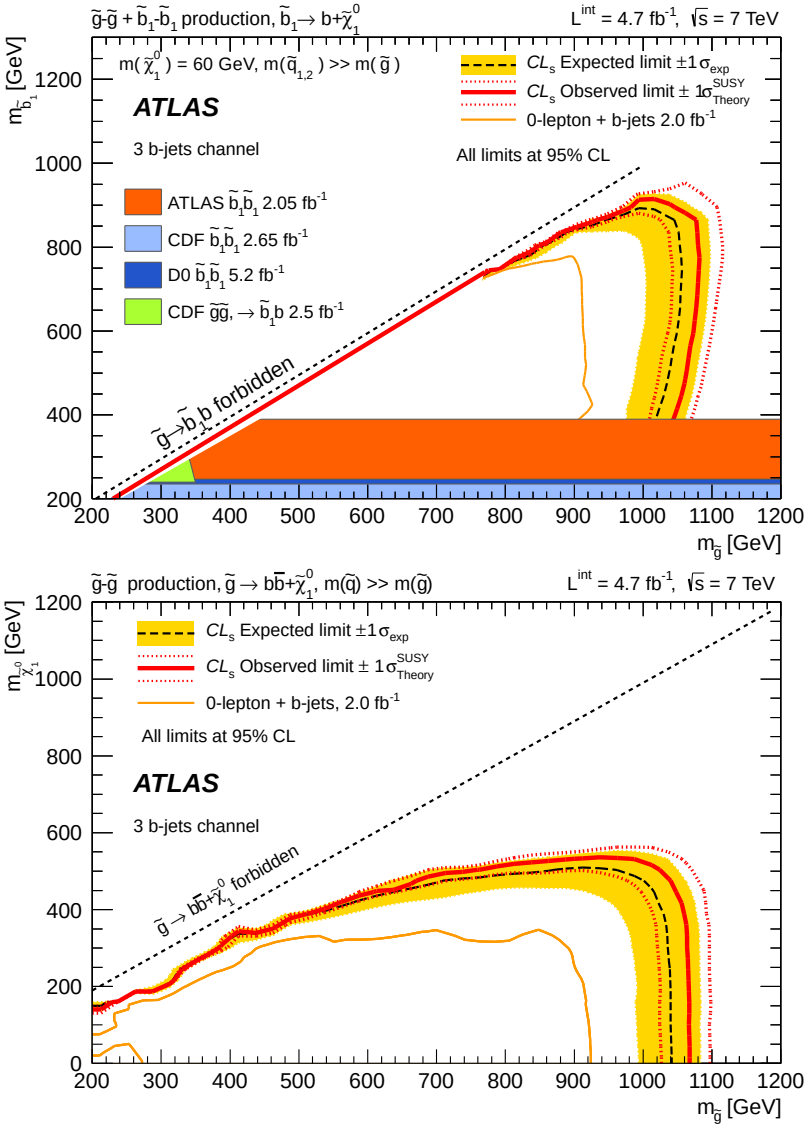

Figure 7.17: Expected and observed exclusion limits at 95% C.L. in the $(m_{\tilde{g}}, m_{\tilde{b}_1})$ plane (*top*) and in the $(m_{\tilde{g}}, m_{\tilde{\chi}_1^0})$ plane (*bottom*). The impact of the theoretical uncertainties are shown using three different limit curves, calculated using the nominal cross section and variations of it.

7.8 Summary

A number of searches for supersymmetry in final states with $E_{\mathrm{T}}^{\mathrm{miss}}$ and b-jets in proton-proton collisions at 7 TeV have been presented. The results are based on data corresponding to integrated luminosities of 35 pb^{-1}, 2.05 fb^{-1} and 4.7 fb^{-1}, collected during 2010 and 2011. In each of the three analyses no excesses over and above the Standard Model expectations are observed. Interpretations are carried out in MSSM scenarios containing gluino-mediated sbottoms, with sbottoms both heavier and lighter than the gluino considered. In both cases gluinos masses around 1 TeV are excluded at 95% C.L. by these searches.

Chapter 8

Searches for Stops and mSUGRA

Bil-qatra l-qatra timtela l-ġarra

8.1 Chapter Abstract

This chapter discusses two searches for the supersymmetric partner of the top quark. A search for gluino-mediated stops in 35 pb^{-1} of data, using leptons, is first described. This search is then combined with the zero lepton search described in Chapter 7 to search for different minimal supergravity models. We also discuss a search for direct stop pair production in the zero lepton channel, carried out using 4.7 fb^{-1} of data.

The one lepton analysis described here has been published in [8] and the contribution of the author was in optimisation, the derivation of the 95% C.L. upper limits in the gluino-stop model, mSUGRA sample generation and the combination of the

zero and one lepton analyses to carry out an exclusion in mSUGRA. The zero lepton direct stop pair production search has been made public by the ATLAS collaboration [5]. The author contributed to the estimation of the multijet background, the optimisation and the derivation of the exclusion limits.

8.2 Gluino-mediated Stop Production

The requirement of naturalness in supersymmetry favours the existence of a light stop quark [113, 114]. If the gluino is also light, but heavier than the stop, stops can be produced in gluino decay chains. Since both the gluino and the stop quark are light we allow for contributions from both $\tilde{g}\tilde{g}$ and $\tilde{t}_1\tilde{t}_1$ pair production. This assumption makes the search easier because the large gluino pair production cross section results in large signal yields. In this section we assume that the stop decay channel $\tilde{t}_1 \to b\tilde{\chi}_1^{\pm}$ dominates completely, with subsequent $\tilde{\chi}_1^{\pm} \to \tilde{\chi}_1^0 l^{\pm}\nu$ decays resulting in high p_{T} leptons. The chargino is assumed to have a mass $m_{\tilde{\chi}_1^{\pm}} \simeq 2 \cdot m_{\tilde{\chi}_1^0}$, with $m_{\tilde{\chi}_1^0} = 60$ GeV, and to decay through a virtual W boson. The branching ratio for $\tilde{\chi}_1^{\pm} \to \tilde{\chi}_1^0 l^{\pm}\nu$ is set to 11%, as in the Standard Model. This scenario, with varying gluino and stop masses, is henceforth referred to as the gluino-stop model and is used for interpretation purposes as well as to optimise the analysis.

8.2.1 Analysis Outline

The presence of leptons in the signal final state allows for events to be selected if they contain at least one isolated muon or one isolated electron. This reduces the amount of multijet background significantly. Furthermore, two jets with $p_{\mathrm{T}} > 60$ GeV and $p_{\mathrm{T}} > 30$ GeV are required, $E_{\mathrm{T}}^{\mathrm{miss}} > 80$ GeV and $m_T > 100$ GeV, where m_T is the transverse mass constructed using the highest p_{T} lepton and $E_{\mathrm{T}}^{\mathrm{miss}}$. This cut rejects events with a W boson in the final state. At least one jet is required to be b-tagged and finally an effective mass cut of 500 GeV is applied. In this analysis the m_{eff} definition includes the p_{T} of the leading lepton.

The efficiency of gluino-stop SUSY signals varies between 0.4% and 3% across the $(m_{\tilde{g}}, m_{\tilde{t}_1})$ plane and depends on $\Delta M = m_{\tilde{g}} - m_{\tilde{t}_1}$. The expected background yield, which is dominated by $t\bar{t}$ production, is estimated using a fully data driven background technique which exploits the lack of correlation between the m_{T} and m_{eff} variables. Four regions in the $(m_{\mathrm{T}}, m_{\mathrm{eff}})$ plane are defined and an ABCD method is implemented. This method is similar to the semi data-driven technique described in Section 6.4. In this case however the transfer factor is derived from data, by taking the ratio of events with $m_{\mathrm{eff}} > 500$ GeV to those with $m_{\mathrm{eff}} < 500$ GeV in events with $m_{\mathrm{T}} < 100$ GeV. The results are corraborated using a pure Monte Carlo estimate. Figure 8.1 shows the distributions of m_{eff} and of $E_{\mathrm{T}}^{\mathrm{miss}}$ in 35 pb^{-1} of data. For the $E_{\mathrm{T}}^{\mathrm{miss}}$ distribution all the cuts described are applied. The m_{eff} distribution is shown after the application of all cuts, except for the m_{eff} cut. Table 8.1 shows the expected

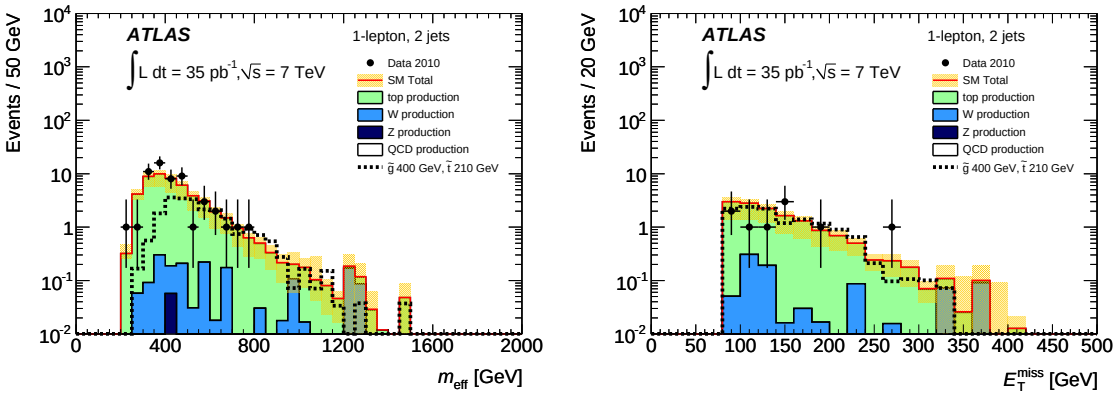

Figure 8.1: Distributions of the effective mass, m_{eff}, (*left*) and the $E_{\mathrm{T}}^{\mathrm{miss}}$, (*right*) for data and for SM expectations. The $E_{\mathrm{T}}^{\mathrm{miss}}$ distribution is shown for events with $m_{\mathrm{eff}} > 500$ GeV. For illustration, the distributions for one reference SUSY signal are superimposed.

and observed yields in the signal region. Both the data driven and MC estimates of the background are shown. No excess is observed in this channel.

The results were interpreted as exclusion limits on the $(m_{\tilde{g}}, m_{\tilde{t}_1})$ plane. In this section PCL is used to evaluate the limit curves. Figure 8.2 shows the observed and expected exclusion limits. Gluino masses below 520 GeV are excluded for stop masses in the range between 130 and 300 GeV.

	Monte Carlo	data-driven
$t\bar{t}$ and single top	12.3 ± 4.0	14.7 ± 3.7
W and Z	0.8 ± 0.4	-
QCD	0.4 ± 0.4	$0^{+0.4}_{-0.0}$
Total SM	13.5 ± 4.1	14.7 ± 3.7
Data	9	9

Table 8.1: Summary of the expected and observed event yields in the one-lepton channel. The results for both the Monte Carlo and the data-driven approach are given. Since the data-driven technique does not distinguish between top and W/Z backgrounds, the total background estimate is shown in the top row. The errors are systematic for the expected Monte Carlo prediction and statistical for the data-driven technique.

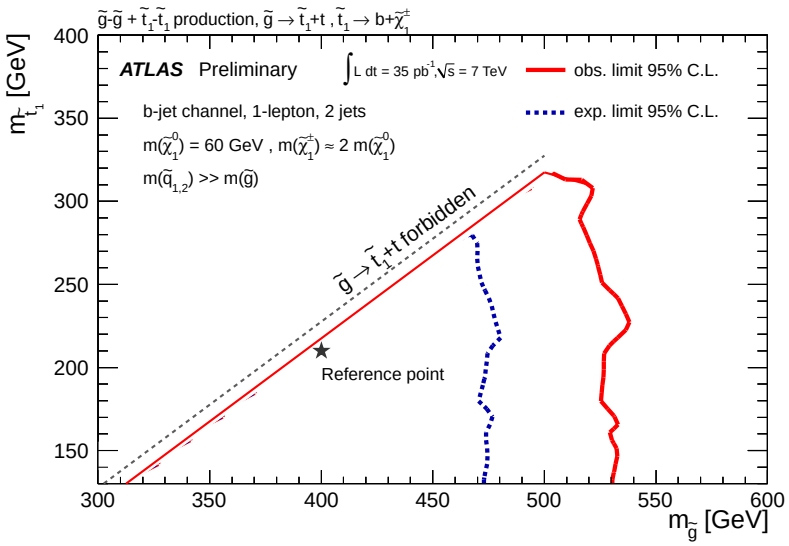

Figure 8.2: The observed and expected 95% C.L. exclusion limits, as obtained with the one-lepton analysis, in the $(m_{\tilde{g}}, m_{\tilde{t}_1})$ plane. The theoretical uncertainties are included in the limit calculation.

8.3 Minimal Supergravity

Minimal supergravity, or mSUGRA, is one of the most commonly studied SUSY-breaking models, partially due to the reduced number of parameters which define it. It is described in Chapter 2, with further details pertinent to this analysis provided here. The exact kinematics of mSUGRA signals depend on the mass hierarchy of the particular model under consideration. The hierarchy depends on the five mSUGRA parameters. In particular, large $\tan\beta$ and $A_0 < 0$ scenarios favour large mass splitting between the two mass-eigenstates of the third generation squarks, possibly resulting in lower stop and sbottom masses. In this section we explore the $(m_0, m_{1/2})$ parameter space while fixing $\tan\beta$ and A_0 to three different sets of values. In all cases $\mu > 0$ is assumed.

8.3.1 Combination

The rich phenomenology in mSUGRA models implies that the signal should contain a wide variety of final states. This means that both the zero lepton analysis described in Chapter 7, as well as the one-lepton analysis, outlined in Section 8.2.1, offer some sensitivity within the $(m_0, m_{1/2})$ plane. This motivates the combination of the two analyses, which is facilitated by the fact that they are statistically orthogonal since the zero(one)-lepton cut uniquely defines events into either of the two catagories. Combining the two orthogonal datasets is expected to result in stronger limits. The combination is carried out by using a likelihood which is a product of the individual zero-lepton and one-lepton likelihoods. The rest of the statistical procedure is equivalent to what is done for the individual analyses.

8.3.2 Interpretation

As discussed earlier, both the zero and one lepton analyses do not show any excesses and therefore 95% C.L. exclusion limits are constructed in three mSUGRA signal

grids, which are described below. The grids are generated using ISAJET and HERWIG.

Tevatron Grid (Low $\tan\beta$)

The first mSUGRA grid considered corresponds to that used in the Tevatron tri-lepton searches [60, 59]. The m_0 and $m_{1/2}$ parameters are varied, $\tan\beta$ is set to 3 and A_0 is set to 0 GeV. Other ATLAS analyses carried out with 35 pb^{-1}, which do not require b-jets, have also performed searches in this scenario [115, 115]. The resultant exclusion limit significantly extends those from the Tevatron experiments. For m_0 up to 450 GeV, $m_{1/2}$ up to 280 GeV is excluded. Beyond $m_0 = 450$ GeV, where the one-lepton analysis does not offer any sensitivity, the limit is dominated by the zero lepton analysis and decreases in $m_{1/2}$ as m_0 increases. [1]

Large $\tan\beta$

A second mSUGRA grid also explores the $(m_0, m_{1/2})$ parameter space. The value of $\tan\beta$ is set to 40 while A_0 is retained at 0 GeV. All other parameters being equal, larger values of $\tan\beta$ lowers the mass of the sbottom in relation to other sparticles. The observed and expected 95% C.L. limits are shown in Figure 8.4. The one lepton search has the same impact as in the low $\tan\beta$ scenario but the zero lepton analysis, which is sensitive to sbottom production, improves in sensitivity and the overall combined limit is about 20 GeV stronger in $m_{1/2}$ at $m_0 > 450$ GeV.

[1] Recent results from the LHCb collaboration [116] on the decay rate of $B_S \to \mu\mu$ have an impact on the limits shown here at high $\tan\beta$. This region of the phase space has been significantly constrained by the new limits, and the results supersede those shown in the mSUGRA models in this Chapter. The decay is suppressed at tree level in the Standard Model and is therefore very rare. The existence of supersymmetry would result in additional Feynman diagrams enhancing the production rate. This makes the decay a powerful way to look for or constrain new physics. Further details about how the LHCb result can be used to constrain supersymmetry at high $\tan\beta$ can be seen in [117].

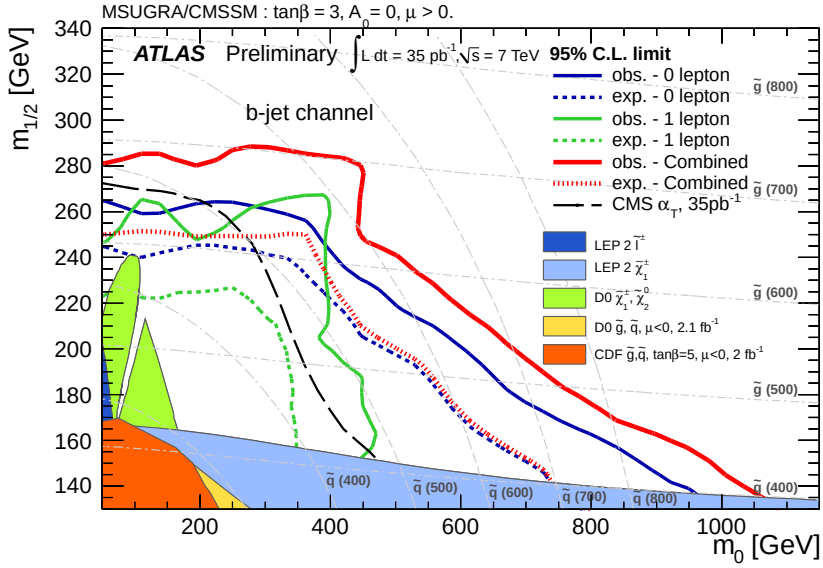

Figure 8.3: The observed and expected 95% C.L. exclusion limits, as obtained with the zero- and one-lepton analyses in the MSUGRA/CMSSM scenario with $\tan\beta$=3, A_0=0 GeV, $\mu > 0$.

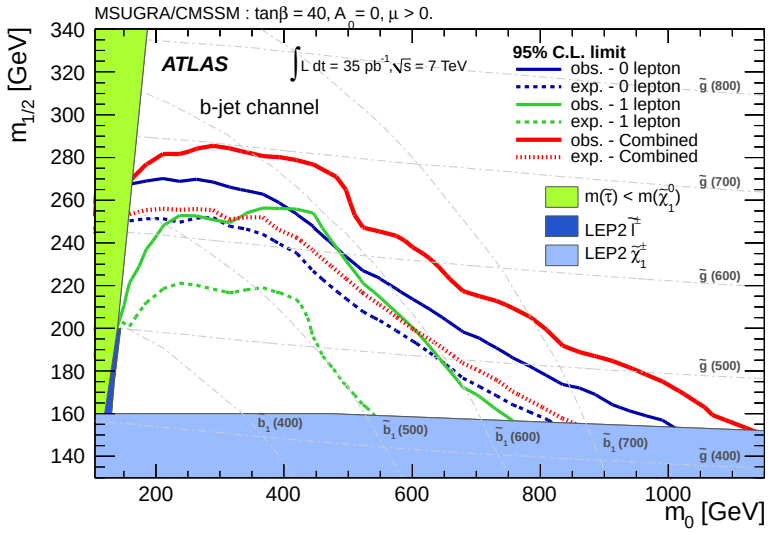

Figure 8.4: Observed and expected 95% C.L. exclusion limits as obtained from the zero- and one-lepton analyses, separately and combined, on MSUGRA/CMSSM scenario with $\tan\beta = 40$, $A_0 = 0$, $\mu > 0$. The light-grey dashed lines are the iso-mass curves for gluinos and sbottoms. Stop masses are 15% lower than sbottom masses.

Large $\tan\beta$ and low A_0

The final mSUGRA grid is generated with $\tan\beta = 40$ and $A_0 = -500$ GeV. Large, negative A_0 results in mixing which further reduces the mass of third generation squarks [118]. Figure 8.5 shows the values of $m_{\tilde{t}_1}$ and $m_{\tilde{b}_1}$ as a function of A_0 for two sets of fixed m_0 and $m_{1/2}$. The value of $m_{\tilde{t}_1}$ can decrease by up to 100 GeV at low

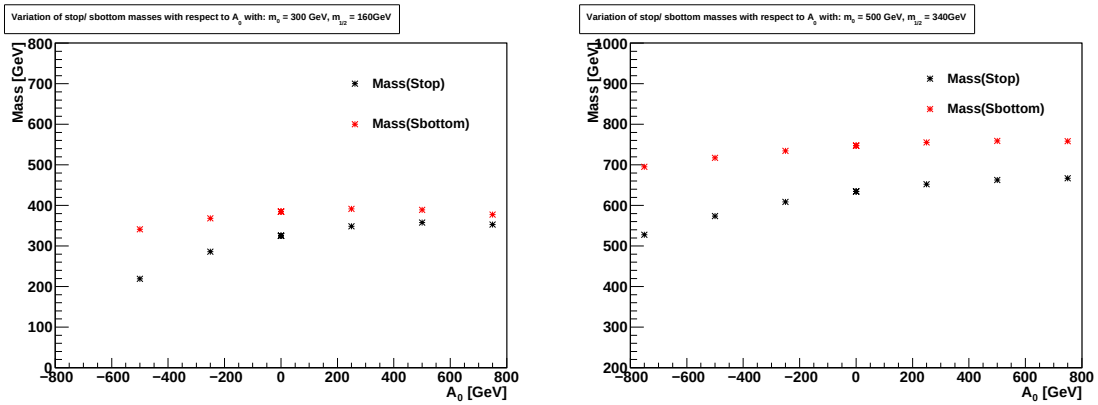

Figure 8.5: Variation of stop and sbottom masses with A_0 in mSUGRA with $\tan\beta = 40$ and $\mu > 0$. The values of m_0 and $m_{1/2}$ are set to 300 and 160 GeV (*left*) and 500 and 340 GeV (*right*).

A_0 in comparison to $A_0 = 0$ GeV. For $m_{\tilde{b}_1}$ the reduction is of the order of 50 GeV. With the chosen parameters a number of configurations at low m_0 are theoretically excluded because the Renormalisation Group Equations fail to converge to physically allowed values or because the neutralino is no longer the lightest supersymmetric particle.

Figure 8.6 shows the expected and observed 95% C.L. limits. For m_0 up to 1 TeV, $m_{1/2}$ up to 180 GeV is excluded. At lower m_0, below 550 GeV, values of $m_{1/2}$ up to 290 GeV are excluded. The improvement in the limit in both the one and zero lepton channels comes about because both the stop and sbottom masses are lower and this drives up their cross sections.

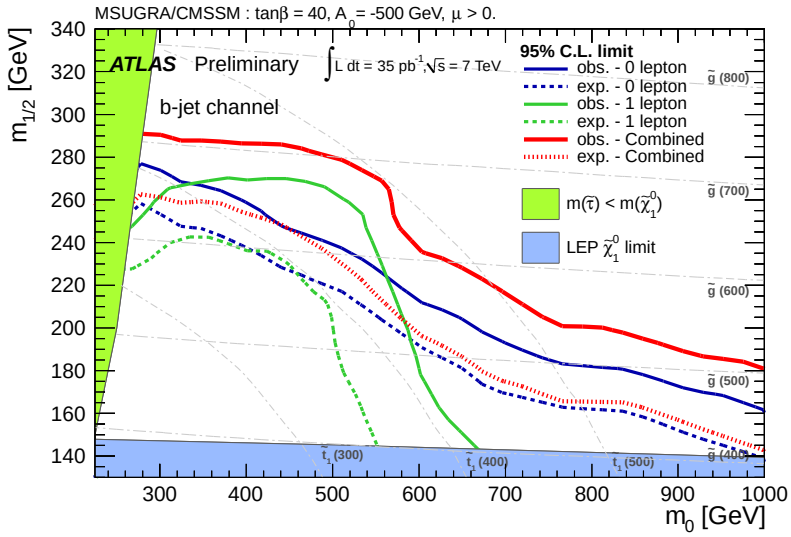

Figure 8.6: The observed and expected 95% C.L. exclusion limits, as obtained with the zero- and one-lepton analyses in the MSUGRA/CMSSM scenario with $\tan\beta$=40, $A_0 = -500$ GeV, $\mu > 0$. The contour of the observed 95% C.L. exclusion limit resulting from the combination of the two channels is also shown. The light-grey dashed lines are the iso-mass curves for gluinos and stops. Sbottom masses are 30% higher than stop masses.

8.4 Direct Scalar Top Production

The stop searches described in Section 8.2.1 are dependent on the gluino also being light enough to be produced at the LHC. Here we discuss a search for direct stop pair production [5] which does not take into account any gluino-mediated contributions. The relatively low stop pair production cross sections means that the analysis can only carried be out using the full 4.7 fb^{-1} of the 2011 data set.

The work in this section was published in [5]. The author contributed to the estimation of the multijet background, the optimisation and the derivation of the exclusion limits.

8.4.1 Analysis Outline

In this particular search stop quarks are assumed to decay into top quarks and neutralinos, i.e. $\tilde{t}_1 \to t\tilde{\chi}_1^0$. The search is geared to select events where both W bosons coming from the top quarks decay hadronically. This results in a final state with six high p_{T} jets from the $t\bar{t}$ final state and substantial $E_{\text{T}}^{\text{miss}}$ from the two neutralinos. The SM background from all-hadronic $t\bar{t}$ is suppressed as it contains no significant intrinsic $E_{\text{T}}^{\text{miss}}$. Instead, the dominant background consists of leptonic $t\bar{t}$ that contains a $W \to \ell\nu$ decay where the lepton, ℓ, is either lost or mis-identified as a jet. These events contain real $E_{\text{T}}^{\text{miss}}$ coming from the neutrino. The multijet background is suppressed by requiring that the $\Delta\varphi_{min}$ for the leading 3 jets is larger than $\pi/3$. Additionally, the angle between the $E_{\text{T}}^{\text{miss}}$ and the missing p_{T} calculated with the tracking system alone is required to be less than $\pi/3$.

To ensure full trigger efficiency, events are required to have at least one jet with $p_{\text{T}} > 130$ GeV and $E_{\text{T}}^{\text{miss}} > 150$ GeV. Events with electrons or muons are rejected, since the all hadronic decay mode of the stop pair system does not contain any leptons. At least five sub-leading jets having $p_{\text{T}} > 30$ GeV must be present. A jet with 1 to 4 tracks and $\Delta\varphi(p_{\text{T},miss}, \text{jet}) < \pi/5$ indicates a likely τ from a $W \to \tau\nu$ decay. Events with τ-like jets that have transverse mass $m_{\text{T}} = \sqrt{2p_{\text{T}}E_{\text{T}}^{\text{miss}}(1 - \cos\Delta\varphi)} < 100$ GeV

are rejected. The MV1 tagger is used to select b-jets and events are retained if they contain either 1 tight b-jet or 2 loose b-jets. Here tight and loose refer to different operating points used for the tagger. Tight b-jets are selected with an efficiency of 60 % and loose b-jets are selected with an efficiency of 75 % in a $t\bar{t}$ MC sample.

Since the $\tilde{t}_1\,\tilde{t}_1$ system contains high-p_{T} top quarks that decay via $t \to bW \to bjj$, a cut on m_t can be used to further reduce SM backgrounds. To estimate m_t a basic clustering technique is used. The method works by combining the three closest jets, using ΔR as a metric. These jets are removed from the event and the second closest triplet of jets is selected to form the second top quark. A requirement on the invariant mass m_{jjj} of $80 < m_{jjj} < 270$ GeV is placed on each reconstructed triplet in the event. The kinematics of $t \to bW \to b\ell\nu$ decay is also used to reduce the dominant ℓ+jets $t\bar{t}$ background, as the m_{T} distribution of the $E_{\mathrm{T}}^{\mathrm{miss}}$ vector with the b-jet, denoted $m_{\mathrm{T}}^{\mathrm{jet}}$, has an endpoint at m_t. When there are ≥ 2 loose b-jets, the $m_{\mathrm{T}}^{\mathrm{jet}}$ for the b-jet closest to the $p_{T,miss}$ is required to be > 175 GeV. The $m_{\mathrm{T}}^{\mathrm{jet}}$ of the four highest-p_{T} jets is required to be > 175 GeV when only one tight b-jet is present in the event.

In order to be sensitive to a variety of different stop-neutralino mass differences, two signal regions are defined. A signal region with $E_{\mathrm{T}}^{\mathrm{miss}} > 150$ GeV (SRA) is devised to target low $m_{\tilde{t}_1}$ and a second signal region, with $E_{\mathrm{T}}^{\mathrm{miss}} > 260$ GeV (SRB), is used for higher $m_{\tilde{t}_1}$. As per other analyses described in this thesis, at each point in the stop-neutralino mass plane, the signal region resulting in the best expected limit is used. Figure 8.7 shows which analysis provides the strongest limit at each point.

Non-Multijet Background Estimation

Following the selection cuts, the dominant source of SM background is $t\bar{t} \to \tau$+jets events where the τ lepton is reconstructed as a jet. Additional, smaller, backgrounds include other $t\bar{t} \to \ell$+jets final states, $t\bar{t} + W/Z$, single top quark production, W/Z plus jets, diboson plus jets and multijet backgrounds.

A transfer factor approach, described earlier in Section 6.4.2, is used to estimate

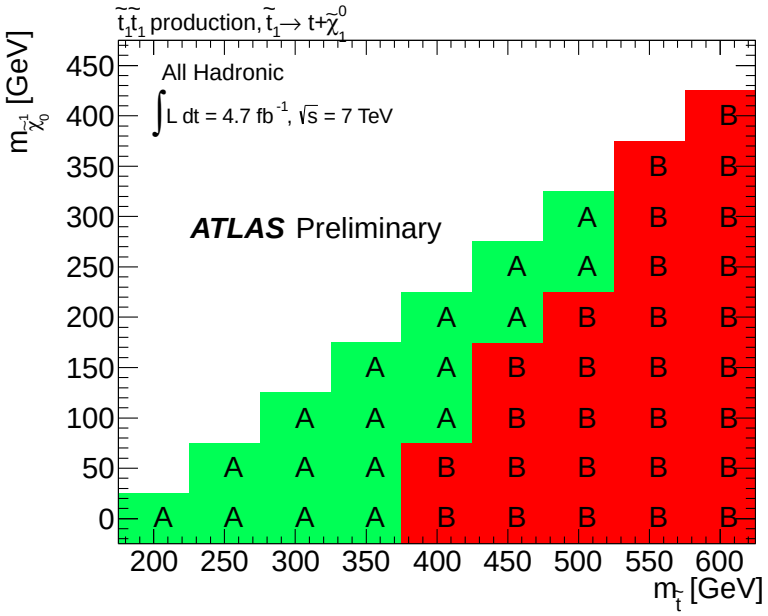

Figure 8.7: A map of $m_{\tilde{\chi}_1^0}$ vs. $m_{\tilde{t}_1}$ that illustrates which signal region (SRA or SRB) is used for the limit extraction. The choice of signal region for a given point was chosen based on the best expected limit.

the top contribution to the signal region. For this analysis the control region is constructed from events containing one isolated muon or electron consistent with $40 < m_{\mathrm{T}} < 120$ GeV and ≥ 5 jet. The jet, b-jet, and $E_{\mathrm{T}}^{\mathrm{miss}}$ requirements remain the same as the standard signal selection. Some constraints are relaxed (the cut on m_{jjj} is relaxed to $m_{jjj} < 600$ GeV) and others removed entirely ($m_{\mathrm{T}}^{\mathrm{jet}}$) to gain statistics. Other non-multijet backgrounds are estimated using Monte Carlo.

Multijet Background Estimation

The jet smearing method, described in Chapter 5, is used to estimate the multijet background in this search. Since this analysis makes use of a number of complex variables constructed using jets, it is crucial to estimate the validity of the smearing method in reproducing these variables. As per usual, pseudoevents are compared to data in a multijet-enriched control region. The cuts applied in the control region, summarised in Table 8.2, are designed to enhance the multijet contributions.

Leading jet $p_T > 130$ GeV, ≥ 6 jets $p_T > 30$ GeV
$E_{\mathrm{T}}^{\mathrm{miss}} > 150$ GeV
1 tight b-tagged jet or 2 loose b-tagged jets
$E_{\mathrm{T}}^{\mathrm{miss,track}} > 30$ GeV
$\left\lvert\Delta\varphi\left(E_{\mathrm{T}}^{\mathrm{miss}}, E_{\mathrm{T}}^{\mathrm{miss,track}}\right)\right\rvert > \frac{\pi}{3}$ **or** $\Delta\varphi_{min} < 0.2\pi$

Table 8.2: Selection criteria for the multijet control region.

Figure 8.8 shows the distributions of kinematic variables in the control region. The $E_{\mathrm{T}}^{\mathrm{miss}}$ is well reproduced, as are both the first and second reconstructed top quark masses. In both cases the discrepancies are well within the conservative 100% uncertainty applied to the estimate in the signal region.

8.4.2 Results and Interpretation

The expected and observed yields for SRA and SRB are summarised in Table 8.3. The data is in good agreement with the Standard Model expectation in both regions. Since no significant excesses are observed, 95% C.L. upper limits are constructed using the CL_s procedure. Figure 8.9 shows the expected and observed limits in the plane. Due to the low number of background events expected in the signal region, the limit was calculated using toy MC simulations. For the observed limits, three curves are shown, each with different cross sections used. These include the nominal NLO cross section as derived using `PROSPINO` as well as the $\pm\sigma_{\mathrm{Theory}}^{\mathrm{SUSY}}$ theory variations. In the most conservative scenario stop masses between 370 and 465 GeV are excluded for neutralino masses of 0 GeV while stop masses of 445 GeV are excluded for neutralino masses of 50 GeV. In the nominal theory scenario, stop masses between 340 GeV and 500 GeV are excluded for massless neutralinos. For stop masses of 445 GeV, neutralino masses of 90 GeV are excluded. The maximum allowed cross section not excluded for each stop and neutralino mass is also shown.

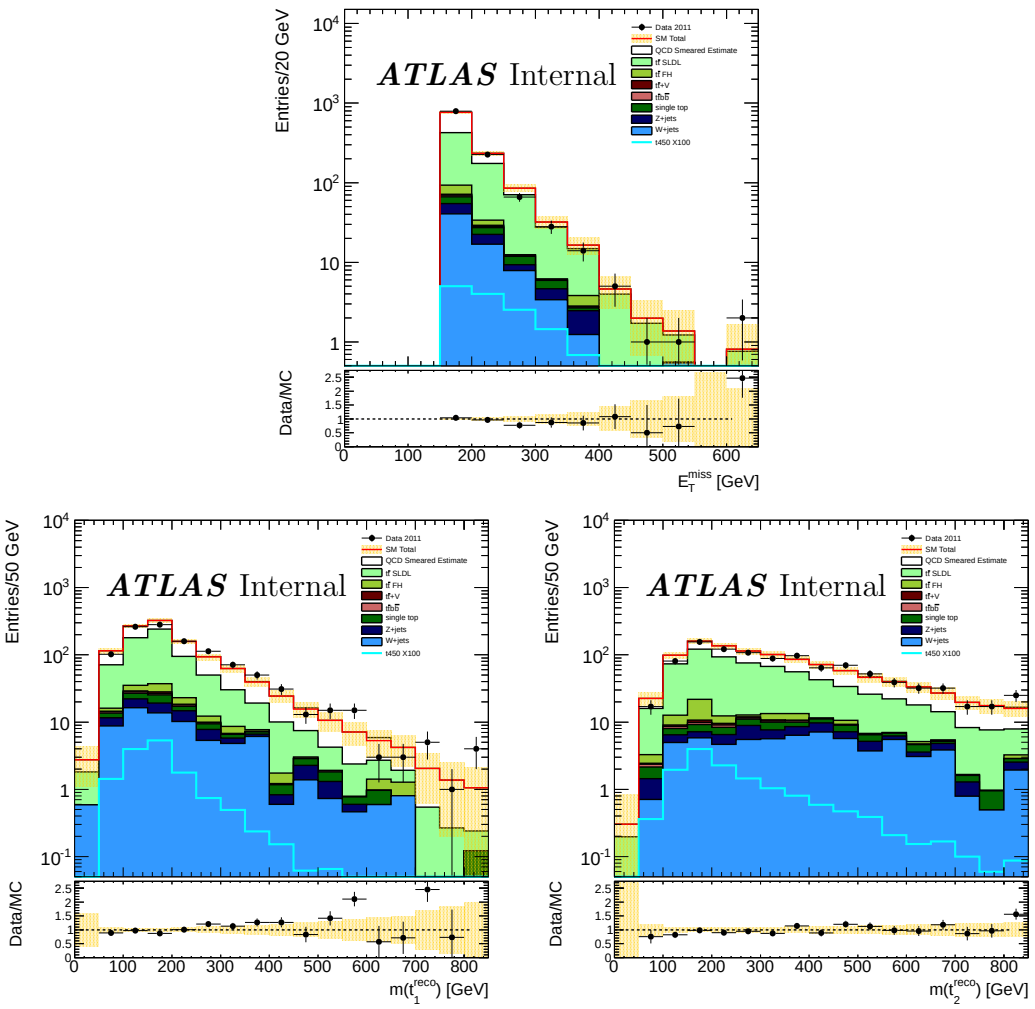

Figure 8.8: The $E_{\mathrm{T}}^{\mathrm{miss}}$ (*top*) and the reconstructed top masses, $m_{t,1}$ (*bottom left*) and $m_{t,2}$ (*bottom right*) are shown in the multijet dominated control region.

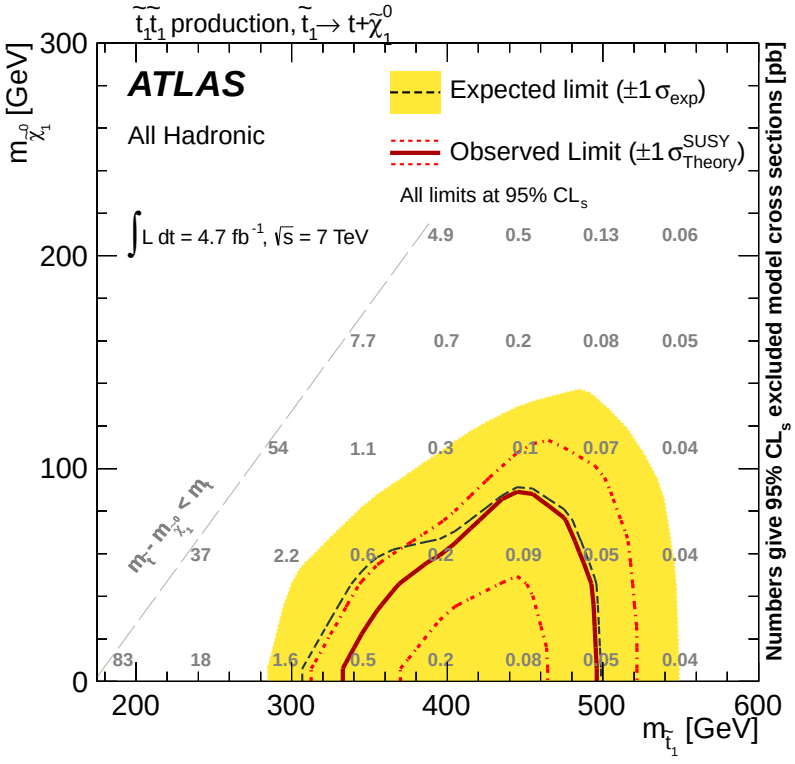

Figure 8.9: Expected and observed 95% CL$_s$ exclusion limits in the $(m_{\tilde{t}_1}, m_{\tilde{\chi}_1^0})$ plane. The numbers overlaid on the plot represent the 95% CL$_s$ excluded model visible cross sections in pb.

	SRA	SRB
	$E_{\mathrm{T}}^{\mathrm{miss}} > 150$ GeV	$E_{\mathrm{T}}^{\mathrm{miss}} > 260$ GeV
$t\bar{t}$	9.2 ± 2.7	2.3 ± 0.6
$t\bar{t} + W/Z$	0.8 ± 0.2	0.4 ± 0.1
Single top	0.7 ± 0.4	$0.2^{+0.3}_{-0.2}$
Z+jets	1.3	
W+jets	$1.2^{+1.4}_{-1.0}$	0.5 ± 0.4
Diboson	$0.1^{+0.2}_{-0.1}$	$0.1^{+0.2}_{-0.1}$
Multi-jets	0.2 ± 0.2	0.02 ± 0.02
Total SM	$13.5^{+3.7}_{-3.6}$	$4.4^{+1.7}_{-1.3}$
Data (observed)	16	4

Table 8.3: The number of expected events for the SM backgrounds and the observed number of events in data.

8.5 Summary

An overview of two searches for scalar top quarks was given. A one-lepton analysis searching for gluino-mediated stops in 35 pb^{-1} of ATLAS data excludes gluino masses of 520 GeV for stop masses between 130 and 300 GeV. This analysis is combined with the zero-lepton analysis from the previous Chapter to set various limits in minimal supergravity models. Finally an exclusion limit is set in the scenario of top pair production, where the gluino is very heavy and therefore does not contribute towards the signal acceptance. No excess is found and stop masses between 370 GeV and 465 GeV are excluded for neutralino masses of 0 GeV, while stop masses of 445 GeV are excluded for neutralino masses of 50 GeV.

Chapter 9

Conclusions

Alla jagħlaq bieb u jiftaħ mija

The Standard Model of physics works incredibly well, and the recent discovery of the Higgs boson lends further credence to this mathematical framework used to describe fundamental physics. However, the hierarchy problem and the lack of understanding of what dark matter is indicate that it is an incomplete theory. Supersymmetry is one possible extension and, by introducing a symmetry between fermions and bosons, solves both these issues. It is expected that supersymmetry should produce new observable particles at the Large Hadron Collider at CERN, which could be detectable by the ATLAS detector. This thesis focuses on the search for these particles, in particular in cases where the supersymmetric partners of the top quark and the bottom quark are amongst the lightest supersymmetric particles, with only the neutralino being lighter. Due to the large number of b-quarks in the signal final states, these searches make use of b-tagged jets to enhance the signal to background ratio.

A multijet background estimation technique, which is validated using data, is discussed in Chapter 5 and shown to reproduce observed distributions in control regions. Chapter 6 describes a search for scalar bottom production and for neutralino masses below 120 (60) GeV; scalar bottom masses up to 350 (390) GeV are excluded. In Chapter 7 , gluino masses below 1060 GeV are excluded for sbottom masses up to about 880 GeV. When the sbottom mass is heavier than the gluino, gluino masses below 1060 GeV are excluded for neutralino masses up to 500 GeV. Chapter 8 describes a search for gluino-mediated stop using a one-lepton analysis. This is combined with a zero-lepton search to extract interpretations in scenarios where supersymmetry breaking is mediated by gravity. A search for direct stop pair production is also described and stop masses between 370 GeV and 465 GeV are excluded for neutralino masses of 0 GeV.

The exclusion limits presented have significantly extended previous bounds and while supersymmetry has not yet been discovered, the work described here forms the basis of on-going searches for physics beyond the Standard Model. The experience gained and the methods devised have helped to increase the sensitivity of ATLAS searches, which could turn out to be crucial should supersymmetry be there to be found.

Appendix A

First Comparisons of Data to Monte Carlo

Bniedem avżat nofsu armat

A.1 Introduction

This appendix describes a first analysis of variables sensitive to supersymmetry final state events with b-jets and missing transverse energy. The focus is on events without any leptons (electrons, muons). The measurements are based on 305 nb^{-1} of data collected with the ATLAS detector in 2010 and allow for a validation of the first data. This was crucial to ensure that the detector, general object definitions and analysis tools were in good shape prior to the recording of larger datasets. General good agreement is found between data and Standard Model expectations as estimated

with Monte Carlo simulations.

The work here was presented in [89]. The candidate's contributions to this analysis include the multijet normalisation, the estimation of the b-tagging uncertainties and the comparisons of data with MC.

A.2 Event Selection

For the purpose of this analysis, in which a first comparison of data to Monte Carlo is made for key observables, a relatively loose set of selections is employed. Selections with 2 jets and 3 jets are investigated, as such final states are used in the analyses described in the main body of the thesis. No optimisation procedure is carried out to maximize the signal to background at this stage. A number of pre-selection requirements are made and these include the removal of misidentified jets and the rejection of events with reconstructed electrons pointing to the calorimeter barrel–endcap transition region ($1.37 < |\eta| < 1.52$). A trigger which requires a hard jet is used, with events retained if they have an offline $p_{\mathrm{T}} > 70$ GeV, in order to be within the plateau of the trigger turn-on curve. At least one additional jet with $p_{\mathrm{T}} > 30$ GeV is also required. All jets are required to have $|\eta| < 2.5$. Events with electrons (muons) with $p_{\mathrm{T}} > 10$ GeV and $|\eta| < 2.47$ ($|\eta| < 2.4$) are rejected, the vast majority being multijet events. This allows for the construction of an orthogonal selection which requires leptons. This is not discussed here but further details are available in [89]. A 3-jet topology is also considered, where the p_{T} of the third leading jet is required to be above 30 GeV.

The signal region is defined by selecting events with $E_{\mathrm{T}}^{\mathrm{miss}}$-significance ($S_{E_T^{Miss}}$) larger than 2 $\mathrm{GeV}^{1/2}$, implemented to reject part of the Standard Model background. The variable is defined as the ratio between the $E_{\mathrm{T}}^{\mathrm{miss}}$ and the square root of the sum of the transverse energy deposited in the calorimeter cells at the electromagnetic scale energy.

$$S_{E_T^{Miss}} \equiv E_{\mathrm{T}}^{\mathrm{miss}} / \sqrt{\sum E_T} \tag{A.1}$$

An event selection based on $S_{E_T^{Miss}}$, rather than on $E_{\mathrm{T}}^{\mathrm{miss}}$, reduces the dependence on the energy scale. Initially, this choice was preferred since, in the dataset used in this analysis, $E_{\mathrm{T}}^{\mathrm{miss}}$ is calibrated at EM scale whilst the jets are corrected to the hadronic energy scale. The correlation between the $S_{E_T^{Miss}}$ and $E_{\mathrm{T}}^{\mathrm{miss}}$ is such that a threshold on $S_{E_T^{Miss}}$ of 2 GeV$^{1/2}$ approximately corresponds to a cut on $E_{\mathrm{T}}^{\mathrm{miss}}$ of about 30 GeV. The correlation can be seen in Figure A.1. The low $S_{E_T^{Miss}}$ region is

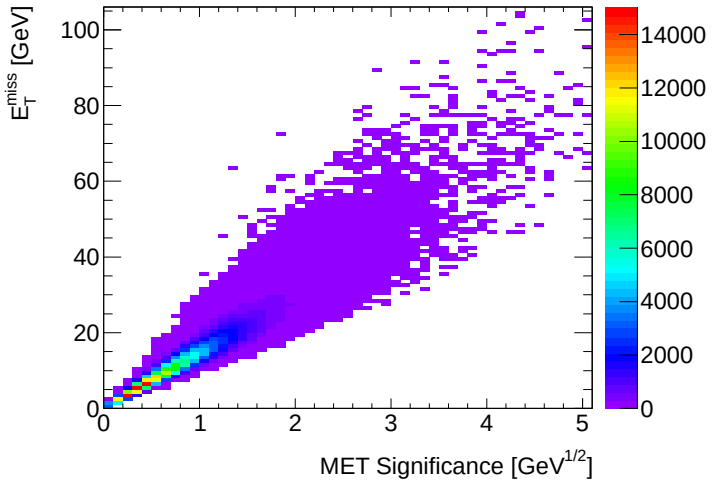

Figure A.1: $E_{\mathrm{T}}^{\mathrm{miss}}$ versus $S_{E_T^{Miss}}$ in first 205 nb^{-1} of data.

retained as a "control" sample and used to estimate the normalisation of the multijet predictions from Monte Carlo simulation, as described in Section A.3. To complete the selection, at least one b-tagged jet is required among all jets with p_{T} above 30 GeV. The tagging algorithm used is the SV0 algorithm, described in Section 4.4.6. The selection cuts are summarised in Table A.1.

A.3 Normalisation of the Multijet Background

Multijet events constitute the dominant Standard Model background for this analysis, due to the large cross section. Within this appendix these processes are estimated use `PYTHIA` Monte Carlo samples. This generator evaluates only diagrams which

Selection Cuts
Pre-selection cuts: data quality, trigger requirements clean up for misidentified jets; electron fiduciality; $\geq$1 primary vertex with $\geq$5 tracks
No lepton ($p_{\mathrm{T}} > 10$ GeV)
2-jet: jet $p_{\mathrm{T}} > (70, 30)$ GeV 3-jet: 3rd jet $p_{\mathrm{T}} > 30$ GeV
$E_{\mathrm{T}}^{\mathrm{miss}}/\sqrt{\sum E_T} > 2$ GeV$^{1/2}$
At least 1 b-tagged jet ($L/\sigma(L)$ >6, $p_{\mathrm{T}} > 30$ GeV)

Table A.1: Event selection for the first data Monte Carlo comparison.

are leading order in the strong coupling constant and therefore is not expected to correctly describe the absolute normalisation of the cross section. To counter for this, a dedicated multijet-enriched control region is constructed and used to normalize the number of events. The shapes of distributions are however still taken from the Monte Carlo.

The control region is identified by requiring events to pass the dijet selection with a reversed $S_{E_T^{Miss}}$ cut at $S_{E_T^{Miss}} <2$ GeV$^{1/2}$. This region is indeed dominated by multijet production and negligible contributions from other processes such as top and W/Z bosons plus jets production are expected. This is because of the large multijet cross section which is orders of magnitude larger than other processes, as shown in Table A.2. Furthermore dijet events are mostly devoid of any real missing transverse energies and will thus have low $S_{E_T^{Miss}}$. Table A.2 also shows the cross section of a signal point in the mSUGRA plane called SU4.

Table A.3 summarizes the number of events from the data and the `PYTHIA` multijet Monte Carlo prediction before and after requiring at least 1 b-tag jet with p_{T} above 30 GeV and $|\eta| <2.5$. The former case is referred to as the "inclusive" sample and the latter as the "b-tag" sample. Due to the relatively soft cuts used, the statistical uncertainties are negligible. The normalisation factor obtained in the inclusive sample, 0.61, is consistent with other ATLAS SUSY results which calculated

Physics process	Cross-section × BR (nb)
Multijet ($\hat{p}_T > 8$ GeV)	10.57×10^6
$W \to \ell\nu$(+jets)	31.4
$Z \to \nu\bar{\nu}$(+jets)	5.82
$Z \to \ell^+\ell^-$(+jets)	2.97
$t\bar{t}$	0.164
Single top	0.076
SU4 SUSY point	0.060

Table A.2: Cross sections of the Standard Model and SUSY benchmark Monte Carlo samples used in this analysis. The cross sections reported are given at NNLO for $W \to \ell\nu$, $Z \to \ell^+\ell^-$ and $Z \to \nu\bar{\nu}$, at NLO+NLL for $t\bar{t}$, at NLO for single top and at leading order for multijet. The cross section for the SU4 point is given at NLO.

the normalisation in a similar way [119]. In a scenario where the b-tagging performance was perfectly modelled by the simulation, the "b-tag" sample would give the same result. However, as can be seen in Table A.3, they do differ and this could be due to inaccurate modelling of the b-tagging in the MC. Such differences might also arise from discrepancies in the modelling of heavy flavour production in the `PYTHIA` multijet Monte Carlo simulation, an effect which is taken into account as a systematic uncertainty (see Section A.4).

Selection	Data	Multijet MC	Data/MC
$S_{E_T^{Miss}} < 2$ GeV$^{1/2}$ (inclusive)	463180	752913	0.61
$S_{E_T^{Miss}} < 2$ GeV$^{1/2}$ (≥ 1 b-tag jet)	28638	42562	0.67

Table A.3: Normalisation with and without tagging in 305 nb^{-1} of data taken in 2010.

Analysis of Control Region Kinematics

Further checks were performed to better understand the adequacy of an average absolute normalisation for an inclusive sample and one with at least one tagged jet. Figure A.2 shows the effective mass and the p_{T} of all jets in the data and MC.

Events are required to pass dijets selection and have $S_{E_T^{Miss}} < 2$ GeV$^{1/2}$. The data/MC normalisation obtained using the inclusive control sample and reported in Table A.2 is applied. For each distribution, the top plots show data and PYTHIA Monte Carlo superimposed, as well as the true b-jet[1] content in the MC. The middle plot shows the data/MC ratio and the lower plot is the fraction of true b-jets in the MC.

Good agreement is found between data and MC, showing that an average normalisation factor can indeed be used for the multijet production samples. One can also see that the kinematic properties of events under study are well reproduced by the simulation in the control region, before and after b-tagging.

[1]In Monte Carlo simulated events, a jet is labelled as true b-jet if a b-quark is found within a cone of $\Delta R < 0.3$ with respect to the jet axis.

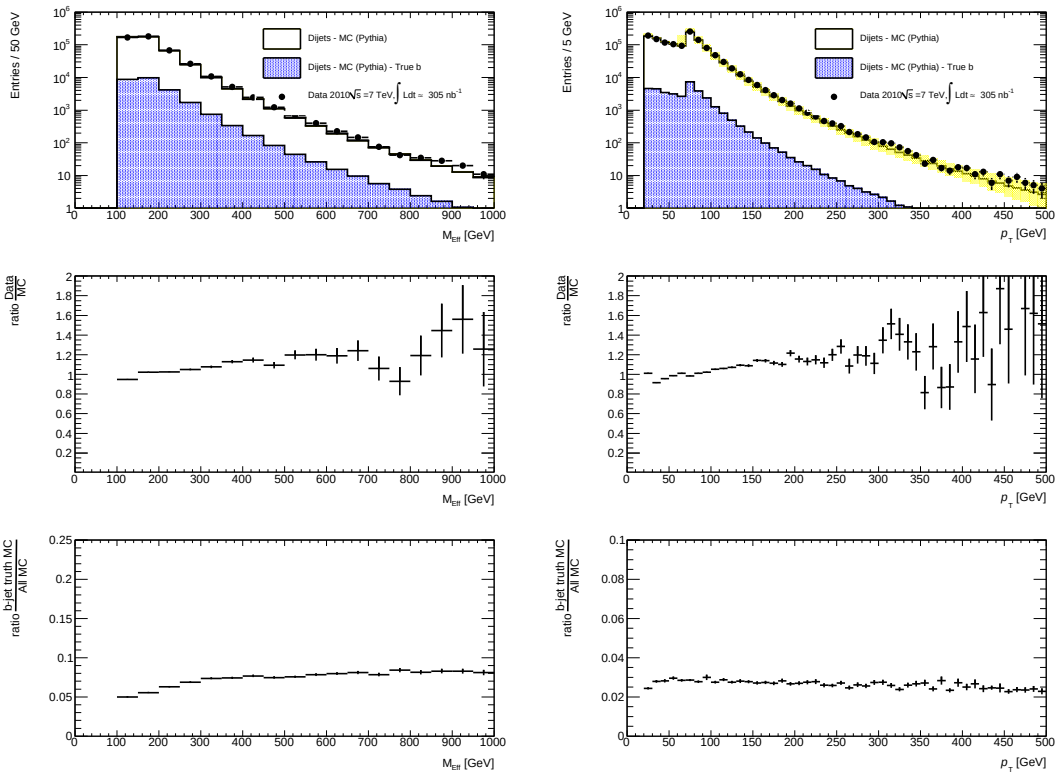

Figure A.2: *Left:* Effective Mass for events passing dijet event preselection cuts and $S_{E_T^{Miss}} < 2$ GeV$^{1/2}$. *Right:* Transverse momentum for all jets in events passing dijet event preselection cuts and $S_{E_T^{Miss}} < 2$ GeV$^{1/2}$.

A.4 Systematic Uncertainties

Several sources of systematic uncertainties on the Standard Model prediction have been studied, and are added in quadrature for the estimation of the total uncertainty.

A.4.1 Tagging Uncertainty

b-tagging Efficiency

The difference between the tagging algorithm performance in data and in Monte Carlo simulation is taken as a systematic uncertainty, using the large statistics of the "inclusive" and "b-tag" control samples. These differences are quantified using the signed $L/\sigma(L)$ distribution, the variable used for tagging jets. Figure A.3 shows the distribution of $L/\sigma(L)$ for all jets with $p_{\mathrm{T}} > 30$ GeV after the inclusive dijets selection for data and Monte Carlo in the control sample, after applying the global normalisation factor 0.61. For jets which qualify as b-jets, i.e. having a weight larger than 6, the Monte Carlo reproduces the data to within 10% in the control region. Thus a systematic uncertainty of 10% is assigned to the MC modelling of the tagging performance.

Mistag Rates

In the negative $L/\sigma(L)$ region of Figure A.3 deviations of the order of 30% can be observed. This region is dominated, as one would expect, by light jets with the true b-jet content below 10%. An estimate of the mistagging uncertainty can be obtained by considering the rate of events with at least one negatively signed weight in the signal and control regions for both data and MC. The resulting numbers can be seen in Table A.4.1. Since one expects the mistag rate to be similar in the control and signal regions, the difference between the two is taken as a systematic uncertainty on the mistag rate. The light jets tagging rate is found to be 16% larger in the signal

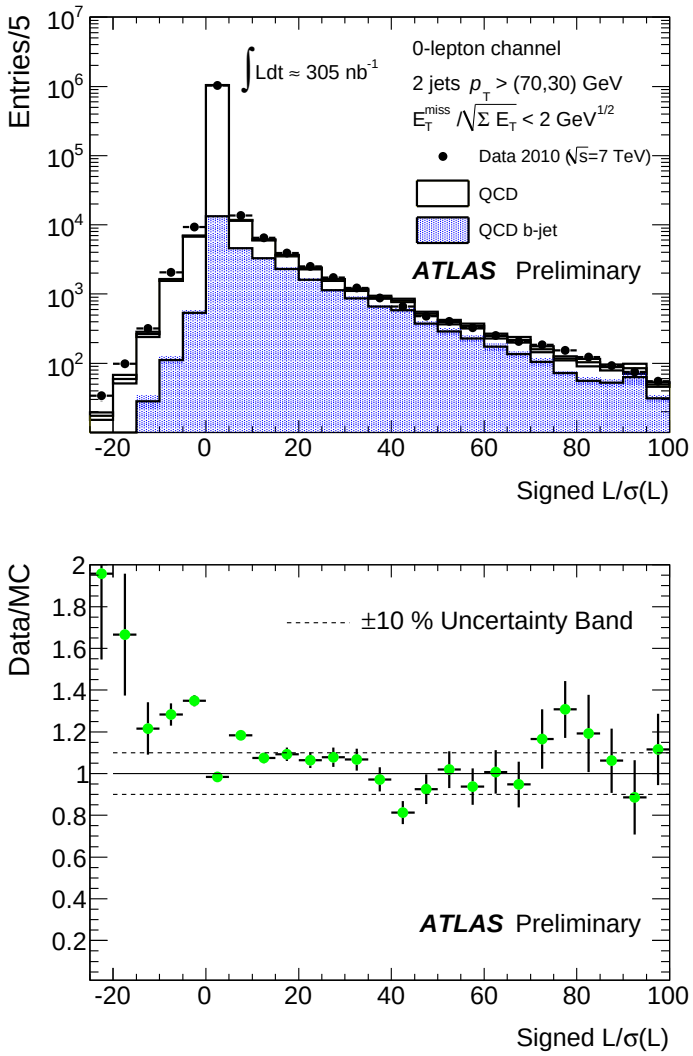

Figure A.3: Signed decay length significance $L/\sigma(L)$ of the reconstructed secondary vertex for all jets in events passing the dijet event selection cuts and $S_{E_T^{Miss}} < 2$ GeV$^{1/2}$, for data and Monte Carlo (MC) expectations. The ratio data/MC is also shown on the bottom.

region with respect to the control region.

	low $S_{E_T^{Miss}}$	high $S_{E_T^{Miss}}$
Data	0.0252±0.001	0.029±0.01
MC	0.0189±0.001	0.0185±0.005

Table A.4: Fraction of events with at least one negative tag jet in the control and signal region as estimated from Data and MC samples (multijet contribution only). The uncertainty is only statistical.

True b-jet content in Control and Signal Regions

The aforementioned systematic uncertainties do not take into account possible differences in the b-jet content between control and signal regions, which might bias the results. The fraction of true b-jet in the high $E_{\mathrm{T}}^{\mathrm{miss}}$ significance region is estimated using MC and is reported in Table A.5. As expected, signal samples are enriched in heavy flavour component, and b-jet content is found to be almost doubled with respect to the b-jet content in control regions. This is because b-jets are more likely to contain real $E_{\mathrm{T}}^{\mathrm{miss}}$, which means there is a correlation between an event passing the $E_{\mathrm{T}}^{\mathrm{miss}}$ cut and the event containing real b-quarks.

region	low $S_{E_T^{Miss}}$	high $S_{E_T^{Miss}}$
b-jet fraction	5.2%	11%

Table A.5: Fraction of events with at least one b-jet in control and signal region as estimated from MC samples (multijet contribution only). Only events passing the dijets preselection are considered.

Taking into account the SV0-based 10% uncertainty and assuming that the uncertainty is mainly driven by the b-jets and not by the light/c-jets content, the 10% uncertainty previously estimated is multiplied by a factor of 2 to account for the truth difference. Therefore a total uncertainty of 20% is assigned to the b-tagging.

Tagging Performance on Key Observables

To better quantify the impact of b-tagging over the entire kinematic range considered in this analysis, the ratios between data and MC for key observables before and after b-tagging are compared in control regions. To isolate the effect of the b-tagging a *double ratio* is devised as shown in Equation A.2. This allows effects like jet energy scale and luminosity to factor out and subsequent effects are solely due to b-tagging.

$$\text{Double Ratio} = \frac{\frac{\text{Data(after tagging cut)}}{\text{MC(after tagging cut)}}}{\frac{\text{Data(before tagging cut)}}{\text{MC(before tagging cut)}}} \tag{A.2}$$

Figure A.4 shows the jet p_{T} distribution for events in the low $E_{\mathrm{T}}^{\mathrm{miss}}$ significance control sample, before (top-left) and after tagging (top-right). The middle plot shows the usual data/MC ratio and the bottom plot shows the double ratio. The plots indicate that there is no residual dependence of the jet p_{T} on the b-tagging performance and the double ratio value lies well within the 20% value assigned as a systematic uncertainty. Similar conclusions can be drawn for other key variables such as the m_{eff} and $E_{\mathrm{T}}^{\mathrm{miss}}$.

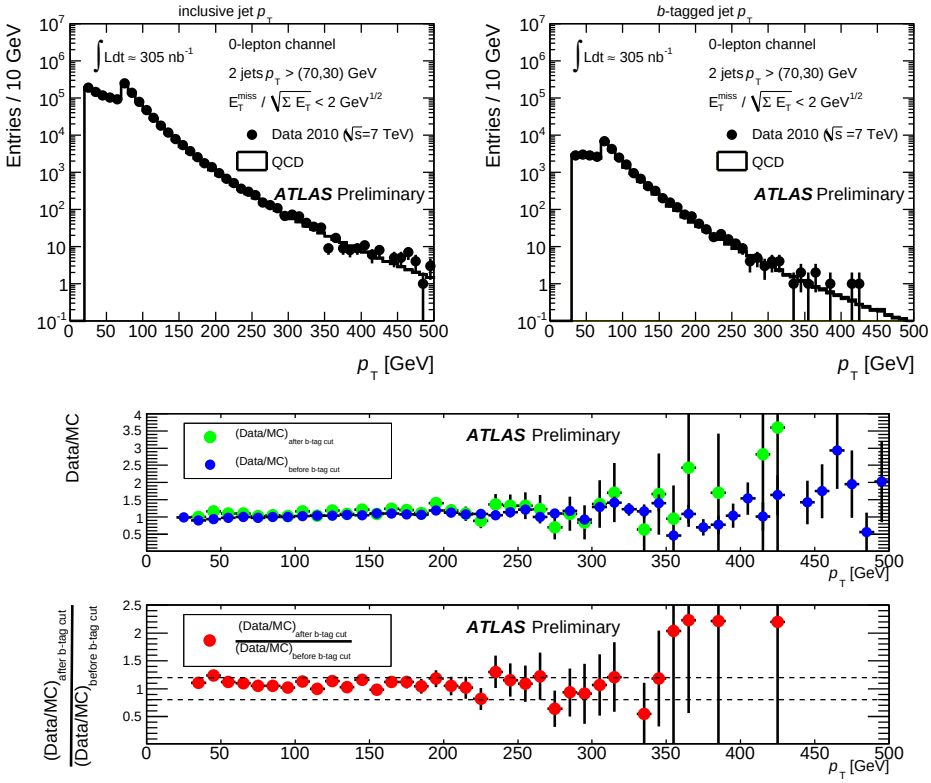

Figure A.4: Jet p_{T} distributions for events in low $S_{E_T^{Miss}}$ control sample, for inclusive and b-tagged jets. The middle plot shows the data/MC ratio and the bottom plot shows the double ratio.

Other Uncertainties

A number of other uncertainties were also taken into account, which were not derived by the author. They are listed in Table A.4.1 and briefly described here. The uncertainty on the unclustered energy is calculated by comparing a variety of PYTHIA samples with different numbers of partonic interactions. A luminosity uncertainty of 11% is considered for all non-multijet backgrounds. For non-multijet processes, including $t\bar{t}$, W and Z production, a conservative value of 60% is used as a theoretical uncertainty.

Source of uncertainty	Value
Jet Energy Scale (including pile-up)	$\sim \pm$ 30%
Unclustered Energy	$\pm$20%
Tagging Performance	$\pm$20%
Lepton Identification Performance	–
Luminosity	$\pm$11%
Theory	$\pm$60%

Table A.6: Relative systematic uncertainties on the Standard Model expected number of events after all selections are applied. Uncertainties on lepton identification performance are applied to the multijet background only via normalisation factors. Uncertainties on the theory refer to W/Z boson plus jets production as explained in the text.

A.5 Results and Distributions

In this section, distributions and yields observed in data are compared to the Standard Model expecation. A possible SUSY model, SU4, is shown for comparison purposes.

A.5.1 2-jet Selection

The number of events in the data and the overall expectation from Standard Model processes are shown in Table A.7 after each event selection step for the dijet selection. The corresponding expectations from the supersymmetry scenario chosen as reference are also given. The statistical and systematic uncertainties described in Section A.4 are added in quadrature. The percentage of reconstructed events that fulfill the b-tagging requirements after the $S_{E_T^{Miss}} > 2$ GeV$^{1/2}$ cut is 12%. The percentage of the Monte Carlo events with a b-tagged jet matched to a true b-quark is 75%. The breakdown of the different Standard Model contributions is presented in Table A.8. As expected, because of the relatively low $E_{\mathrm{T}}^{\mathrm{miss}}$ selection ($\simeq$ 30 GeV), multijet production processes dominate the signal region.

2-jet selection	Data	Standard Model expectation	SU4
p_{T}(jets) $> (70, 30)$ GeV	474243	$(4.7^{+2.1}_{-1.9}) \cdot 10^5$	9.95±0.06
$S_{E_T^{Miss}} > 2$ GeV$^{1/2}$	11190	$(1.1^{+0.5}_{-0.6}) \cdot 10^4$	8.71±0.06
$\geq$1 b-tagged jet	1253	1190 ± 430	4.23±0.04

Table A.7: Number of events observed in the data and expected contributions of the different Standard Model processes for the 2-jet event selection. The expectations for the reference SU4 supersymmetry scenario are also given.

2-jet selection	Multijet	W+jets	Z+jets	top
p_{T}(jets) $> (70, 30)$ GeV	(4.72 ± 0.01)·10^5	71.1 ± 0.3	28.6 ± 0.2	26.4 ± 0.07
$S_{E_T^{Miss}} > 2$ GeV$^{1/2}$	(1.11 ± 0.02)·10^4	47.4 ± 0.2	19.3 ± 0.2	6.73 ± 0.02
$\geq$1 b-tagged jet	1181 ± 36	2.18 ± 0.04	0.74 ± 0.03	4.51 ± 0.02

Table A.8: Breakdown of the different processes contributing to the Standard Model expectation for the 2-jet event selection. Only statistical uncertainties are given.

The SV0 weight and the b-tagged jet multiplicity are shown in Figure A.5 for data, the Standard Model contributions and SU4. Generally, good agreement is found between data and Standard Model expectations estimated from Monte Carlo, for all these quantities. At high p_{T} (>200 GeV), the b-tagged jet spectrum shows that

the PYTHIA multijet prediction slightly underestimates the data, as is expected for PYTHIA.

Data and Monte Carlo expectations are also in good agreement for complex variables like $E_{\mathrm{T}}^{\mathrm{miss}}$ significance and effective mass m_{eff}, as shown in Figure A.6.

The multijet background with large $E_{\mathrm{T}}^{\mathrm{miss}}$ originates from misreconstruction of the jet energies in the calorimeters. In such events the $E_{\mathrm{T}}^{\mathrm{miss}}$ direction tends to be aligned, in the transverse plane, with one of the leading jets in the event. A high suppression of the multijet background can be achieved by requiring a minimum azimuthal distance between the leading jets and the $E_{\mathrm{T}}^{\mathrm{miss}}$ direction, $\Delta\varphi_{\mathrm{min}}(E_{\mathrm{T}}^{\mathrm{miss}}, \mathrm{jet})$. Figure A.7 shows the $\Delta\varphi_{\mathrm{min}}(E_{\mathrm{T}}^{\mathrm{miss}}, \mathrm{jet})$ distribution, where the first three leading jets with p_{T} >20 GeV are considered, and the m_{eff} distribution for events passing the requirement $\Delta\varphi_{\mathrm{min}}(E_{\mathrm{T}}^{\mathrm{miss}}, \mathrm{jet}) > 0.2$: 446 events are found in data, in good agreement with the expectation of 410^{+150}_{-180}. About 65% of the events are rejected by this selection.

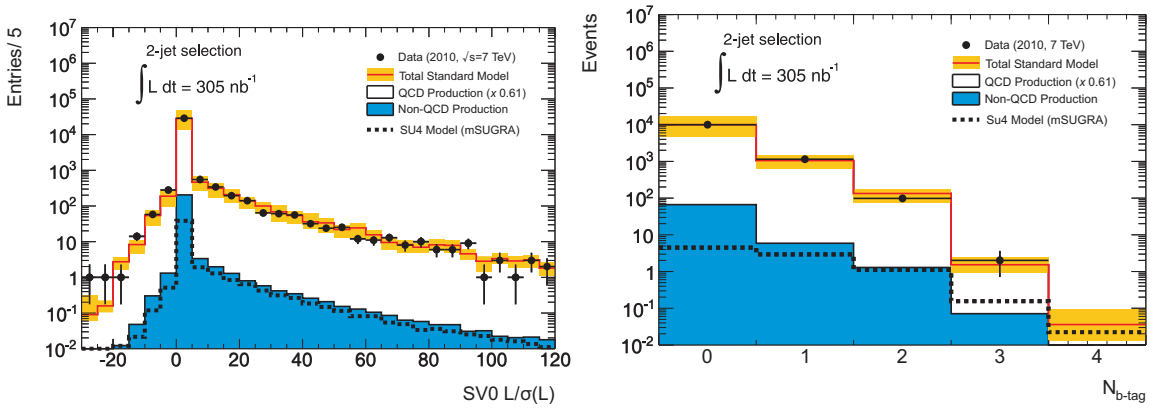

Figure A.5: b-tag SV0 $L/\sigma(L)$ distribution (*left*) and the multiplicity of b-tagged jets (*right*) for data and the different Standard Model contributions before the b-tagged jet requirement for the 2-jet event selection.

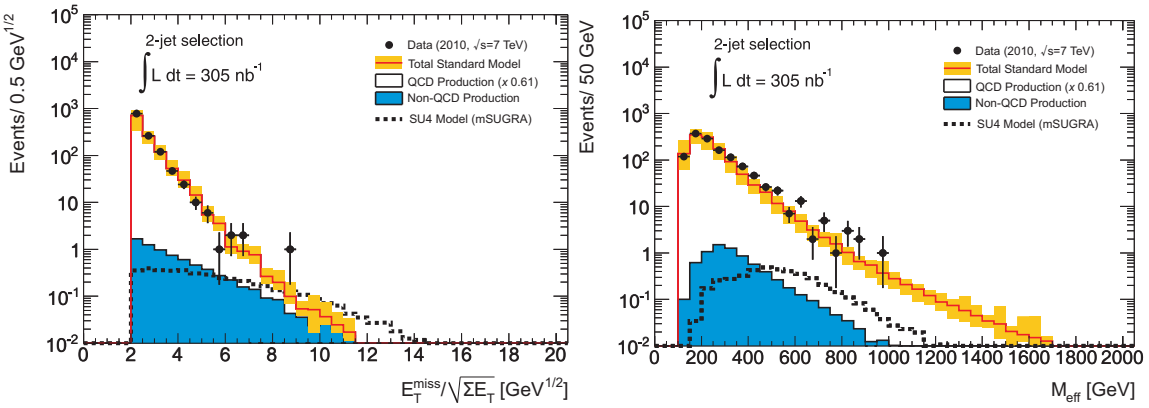

Figure A.6: $S_{E_T^{Miss}}$ (*left*) and Effective Mass m_{eff} (*right*) for data and the different Standard Model contributions after the 2-jet event selection is applied.

A.5.2 3-jet Selection

If another jet is required in the selection, 429 data events remain, in agreement with the Standard Model Monte Carlo expectation of 400^{+160}_{-160}. The number of events for supersymmetry bench mark point SU4 is approximately the same as in the 2-jet selection since the signal produces events with high jet multiplicities. The $S_{E_T^{Miss}}$, the m_{eff} and the p_{T} of the leading jet and the highest b-tagged SV0 $L/\sigma(L)$ jet, after the 3-jet event selection is applied, are shown in Figure A.8. Good agreement between data and Standard Model expectations is observed within the statistical and systematic uncertainties in all regions of phase space covered with the current dataset.

A.6 Summary

The purpose of this first data study was to begin probing the phase space relevant to SUSY searches and to ensure that the Monte Carlo generators provide a reasonable modelling of the background. Indeed good data to Monte Carlo agreement is observed in most distributions, well within the systematic uncertainties derived. The only tensions can be seen in the tails of the p_{T} distributions where the MC used

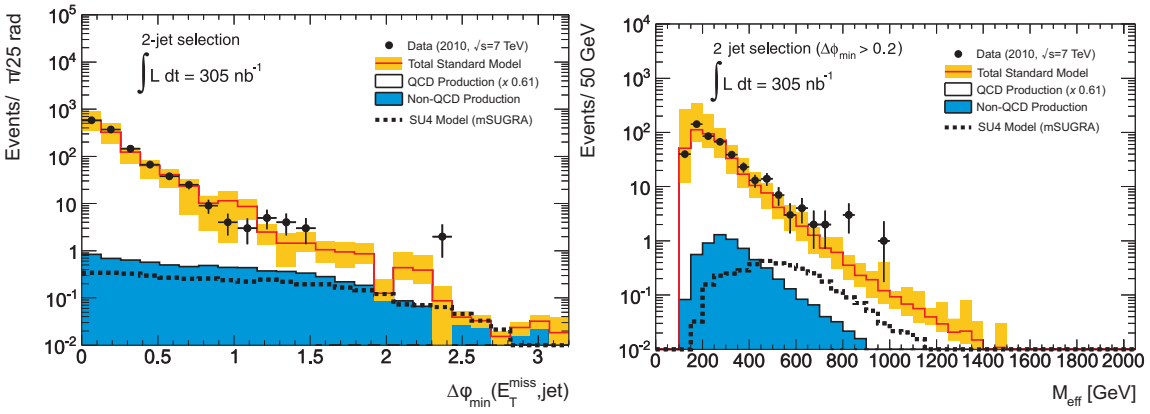

Figure A.7: Minimal azimuthal angle between the jets with highest p_{T} and the $E_{\mathrm{T}}^{\mathrm{miss}}$ (*left*) and the Effective mass (m_{eff}) distribution after $\Delta\varphi_{min}(E_{\mathrm{T}}^{\mathrm{miss}}, \mathrm{jet}) > 0.2$ (*right*) for data and the expected Standard Model contributions after the 2-jet event selection is applied.

is not expected to describe the data well. This motivates the use of data driven techniques when calculating the multijet background, which is discussed in Chapter 5. Furthermore no clear excess is observed in the data, indicating that, should new physics appear at 7 TeV, it is not in the bulk of the distributions and must lie in the tails.

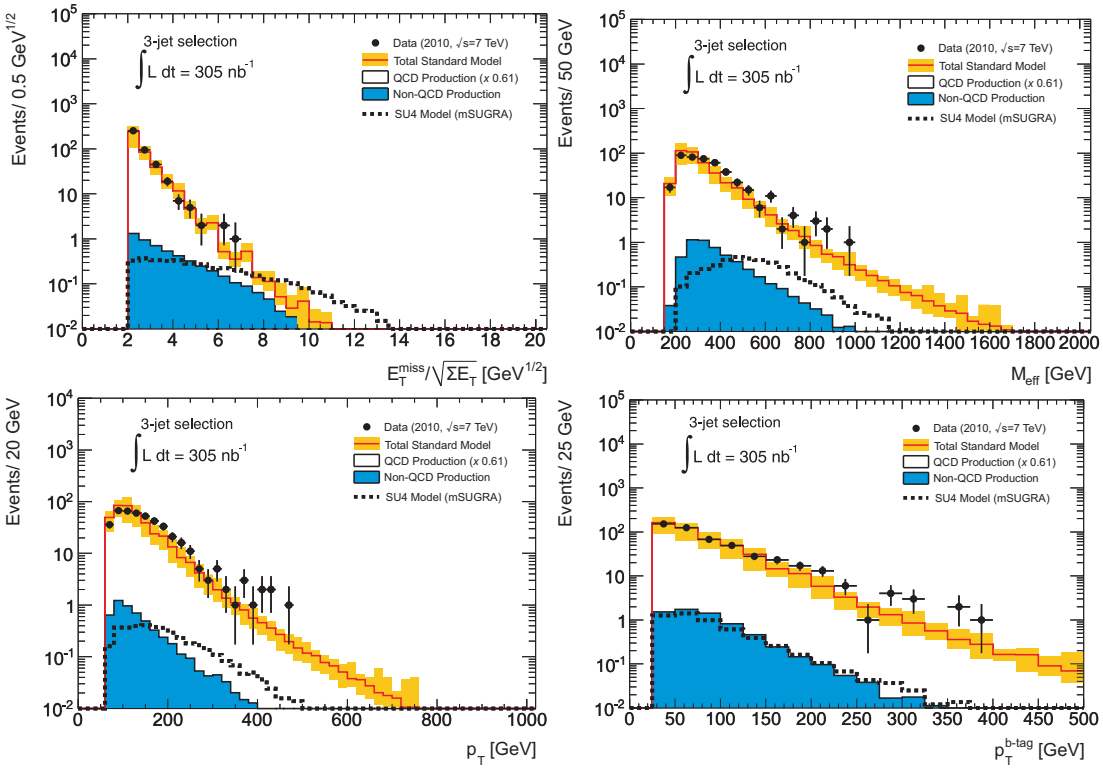

Figure A.8: $S_{E_T^{Miss}}$ (*top left*), m_{eff} (*top right*), p_{T} of the leading jet (*bottom left*) and p_{T} of the highest SV0 $L/\sigma(L)$ b-tagged jet (*bottom right*) distributions for data and the expected Standard Model contributions after the 3-jet event selection is applied.

Appendix B

Jet Smearing in the LAr hole

During data taking in 2011 around 0.87 fb^{-1} of data were affected by problems in the LAr calorimeter, where a region was not functional. The problem was localised in η and φ with a "hole" located at $-1 < \eta < 1.5$ and $-0.9 < \varphi < 0.5$. To tackle the LAr hole problem a slight modification of the smearing technique was required. A different response function, which mirrors the problem in the calorimeter, is required. The seed selection and normalisation also need to be changed.

Response Function

A $t\bar{t}$ Monte Carlo sample, containing 1.5 million events, was generated with the LAr problem built into the simulation. Jets pointing at the LAr hole were selected from this sample, and used to construct a "LAr-hole response function". Due to the low statistics of jets in the LAr hole the response function is constructed using two bins only, encompassing $[0, 100]$ GeV and $[100, 3500]$ GeV. Figure B.1 shows the LAr response in two different p_{T} ranges. Also shown, in the same figure, is the response for light jets outside the LAr hole.

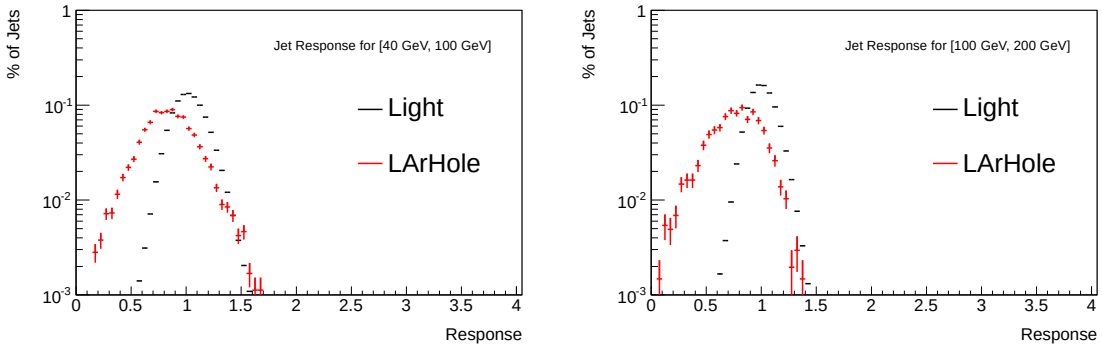

Figure B.1: Plots of the response function for light jets inside and outside the LAr hole in the true p_{T} ranges $[40, 100]$ GeV (*left*) and $[100, 200]$ GeV (*right*).

Seed Selection

The standard seed selection will not retain any events with a jet within the LAr hole as large energy loss will result in events rich in $E_{\mathrm{T}}^{\mathrm{miss}}$. The reversed $E_{\mathrm{T}}^{\mathrm{miss}}$ significance requirement will therefore cut out such events. To counter for this, the seed selection is modified slightly. Regular seed events, without a jet pointing towards the LAr hole, are selected. They are then repeatedly rotated by a random angle, such that one of the jets lies facing the LAr hole. Jets outside the LAr hole are smeared using the standard response functions and jets within the LAr hole are smeared using the special response function showed in Figure B.1.

Validation and Normalisation

Since the LAr issue is one which will affect the non-Gaussian component of the response function, it is crucial that this part of the response is validated. The Mercedes selection is repeated, with the additional requirement that the fluctuating jet lies within, or opposite, the LAr hole. After a correction to the low side part of the response one obtains the distribution shown in Figure B.2, with reasonably good agreement observed.

To normalize pseudoevents generated with the LAr hole sample a separate con-

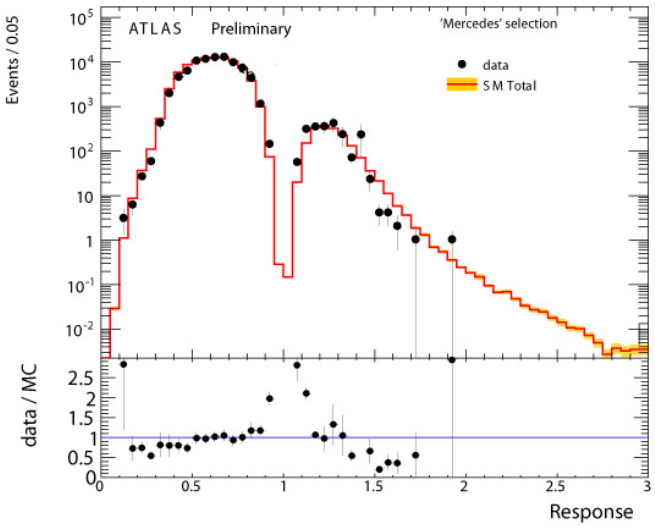

Figure B.2: The Mercedes selection for events with a jet pointing to the LAr hole, after corrections are applied.

trol region needs to be defined. Events are selected if they have a jet pointing towards the LAr hole, and substantial $E_{\mathrm{T}}^{\mathrm{miss}}$ which is close this jet in φ. The contamination from non-multijet events in the control region is $\lesssim$10% and this is approximated using MC.

Appendix C

Gluino-Mediated Sbottoms Signal Regions

This appendix summarises the signal regions used in the search for gluino-mediated sbottom quarks.

35 pb^{-1} Analysis (2010)	2 fb^{-1} Analysis (2011)	4.7 fb^{-1} Analysis (2011)
Common selection: Data Quality, Event Cleaning, Bad Jet vetos No Electrons or Muons		
Luminosity dependent cuts:		
$p_T^{j1} > 130$ GeV $p_T^{j2} > 30$ GeV $p_T^{j3} > 30$ GeV -	$p_T^{j1} > 130$ GeV $p_T^{j2} > 50$ GeV $p_T^{j3} > 50$ GeV -	$p_T^{j1} > 160$ GeV $p_T^{j2} > 50$ GeV $p_T^{j3} > 50$ GeV $p_T^{j4} > 50$ GeV
$E_{\mathrm{T}}^{\mathrm{miss}} > 100$ GeV	$E_{\mathrm{T}}^{\mathrm{miss}} > 130$ GeV	$E_{\mathrm{T}}^{\mathrm{miss}} > 160$ GeV
$E_{\mathrm{T}}^{\mathrm{miss}}/m_{\mathrm{eff}} > 0.2$		
$\Delta\varphi_{min} > 0.4$		
≥ 1 b-jet ($p_T^{b1} > 30$ GeV)	$\geq 1(2)$ b-jets ($p_T^{b1} > 50$ GeV)	≥ 3 b-jets ($p_T^{b1} > 30$ GeV)
SR: $m_{\mathrm{eff}} > 600$ GeV	SR1-A (SR2-A): $m_{\mathrm{eff}} > 500$ GeV SR1-B (SR2-B): $m_{\mathrm{eff}} > 700$ GeV SR1-C (SR2-C): $m_{\mathrm{eff}} > 900$ GeV	loose: $m_{\mathrm{eff}} > 500$ GeV medium: $m_{\mathrm{eff}} > 700$ GeV tight: $m_{\mathrm{eff}} > 900$ GeV

Table C.1: Signal regions for the different analyses used to search for gluino-mediated sbottom quarks.

Appendix D

Maltese Proverbs

Throughout this thesis, following each chapter title, one can find a Maltese proverb. For the benefit of those who do not speak the language I have listed the translations below.

- *Il-mistoqsija oħt il-għerf*: The question is the sister of wisdom.
- *Ebda warda bla xewka* : No rose is without thorns.
- *L-għodda nofs is-sengħa*: The tools are half the trade.
- *L-ilma fil-bir ma jaqtax għatx*: Water in the well does not quench thirst.
- *Qis mitt darba, u aqta' darba*: Measure one hundred times, and cut once.
- *Biex taqta' sewwa trid tisma ż-żewġ naħat* : To decide fairly one must listen to both sides.
- *Fuq tlieta toqgħod il-borma*: The pot rests on a tripod.
- *Bil-qatra l-qatra timtela l-ġarra*: Drop by drop, the jar is slowly filled.
- *Alla jagħlaq bieb u jiftaħ mija*: God closes one door, and opens a hundred.

Bibliography

[1] ATLAS Collaboration, *Search for supersymmetry in pp collisions at* $\sqrt{s} = 7$ *TeV in final states with missing transverse momentum, b-jets and no leptons with the ATLAS detector*, ATLAS-CONF-2011-098, 2011.

[2] ATLAS Collaboration, *Search for supersymmetry in pp collisions at* $\sqrt{s} = 7$ TeV *in final states with missing transverse momentum and b-jets with the ATLAS detector*, Phys. Rev. **D85** (2012) 112006.

[3] ATLAS Collaboration, *Search for Scalar Bottom Quark Pair Production with the ATLAS Detector in pp Collisions at* $\sqrt{s} = 7$ *TeV*, Phys. Rev. Lett. **108** (2012) 181802.

[4] ATLAS Collaboration, *Search for top and bottom squarks from gluino pair production in final states with missing transverse energy and at least three b-jets with the ATLAS detector*, `arXiv:hep-ex/1207.4686 [hep-ex]`.

[5] ATLAS Collaboration, *Search for a supersymmetric partner of the top quark in final states with jets and missing transverse momentum at* $\sqrt{s} = 7$ *TeV with the ATLAS detector*, ATLAS-CONF-2012-074, 2012.

[6] ATLAS Collaboration, *Search for scalar bottom pair production in final states with missing transverse momentum and two b-jets in pp collisions at* $\sqrt{s} = 7$ *TeV with the ATLAS Detector*, ATLAS-CONF-2012-106, 2012.

[7] ATLAS Collaboration, *Search for new phenomena in final states with large jet multiplicities and missing transverse momentum using* $\sqrt{s} = 7$ *TeV pp collisions with the ATLAS detector*, JHEP **11** (2011) 1–38.

[8] ATLAS Collaboration, *Search for supersymmetry in pp collisions at $\sqrt{s} = 7$ TeV in final states with missing transverse momentum and b-jets*, `arXiv:1103.4344 [hep-ex]`.

[9] ATLAS Collaboration, *Search for squarks and gluinos using final states with jets and missing transverse momentum with the ATLAS detector in proton proton collisions*, Phys. Lett. B **710** (2012) 67 – 85.

[10] ATLAS Collaboration, *Search for supersymmetry in pp collisions at $\sqrt{s} = 7$ TeV in final states with missing transverse momentum, b-jets and one lepton with the ATLAS detector*, ATLAS-CONF-2011-130, 2011.

[11] ATLAS Collaboration, *The ATLAS Experiment at the CERN Large Hadron Collider*, JINST **3** (2008) S08003.

[12] J. Thomson, *Cathode Rays*, Philosophical Magazine **44** (1897) 295.

[13] I. Aitchison and A. Hey, *Gauge theories in particle physics: a practical introduction*. Graduate Student Series in Physics. A. Hilger, 2008.

[14] D. Griffiths, *Introduction to Elementary Particles*. Wiley, 2008.

[15] S. P. Martin, *A Supersymmetry Primer*, 1997. `arXiv:hep-ph/9709356`.

[16] *Introduction to Elementary Particles*. Wiley-VCH, 2nd ed., Oct., 2008. `http://www.worldcat.org/isbn/3527406018`.

[17] S. L. Glashow, *Partial Symmetries of Weak Interactions*, Nucl. Phys. **22** (1961) 579–588.

[18] S. Weinberg, *A Model of Leptons*, Phys. Rev. Lett. **19** (1967) 1264–1266.

[19] A. Salam, *Gauge unification of fundamental forces*, Rev. Mod. Phys. **52** (1980) 525–538.

[20] J. Beringer et al. (Particle Data Group), *Review of Particle Physics*, Phys. Rev. **D86** (2012) 010001.

[21] F. Englert and R. Brout, *Broken Symmetry and the Mass of Gauge Vector Mesons*, Phys. Rev. Lett. **13** (1964) 321–323.

[22] G. S. Guralnik, C. R. Hagen, and T. W. B. Kibble, *Global Conservation Laws and Massless Particles*, Phys. Rev. Lett. **13** (1964) 585–587.

[23] P. W. Higgs, *Broken Symmetries and the Masses of Gauge Bosons*, Phys. Rev. Lett. **13** (1964) 508–509.

[24] Super-Kamiokande Collaboration, *Evidence for Oscillation of Atmospheric Neutrinos*, Phys. Rev. Lett. **81** (1998) 1562–1567.

[25] MINOS Collaboration, *Measurement of Neutrino Oscillations with the MINOS Detectors in the NuMI Beam*, Phys. Rev. Lett. **101** (2008) 131802.

[26] KamLAND Collaboration, *Measurement of neutrino oscillation with KamLAND: Evidence of spectral distortion*, Phys.Rev.Lett. **94** (2005) 081801.

[27] GNO Collaboration, *Complete results for five years of GNO solar neutrino observations*, Phys. Lett. **B616** (2005) 174–190.

[28] N. Cabibbo, *Unitary Symmetry and Leptonic Decays*, Phys. Rev. Lett. **10** (1963) 531–533.

[29] M. Kobayashi and T. Maskawa, *CP-Violation in the Renormalizable Theory of Weak Interaction*, Prog. Theor. Phys. **49** (1973) 652–657.

[30] J. H. Christenson, J. W. Cronin, V. L. Fitch, and R. Turlay, *Evidence for the 2π Decay of the K_2^0 Meson*, Phys. Rev. Lett. **13** (1964) 138–140.

[31] D0 Collaboration, *Search for High Mass Top Quark Production in $p\overline{p}$ Collisions at $\sqrt{s} =$ 1.8 TeV*, Phys. Rev. Lett. **74** (1995) 2422–2426.

[32] CDF Collaboration, *Observation of Top Quark Production in $\overline{p}p$ Collisions with the Collider Detector at Fermilab*, Phys. Rev. Lett. **74** (1995) 2626–2631.

[33] DONUT Collaboration Collaboration, K. Kodama et al., *Observation of tau neutrino interactions*, Phys.Lett. **B504** (2001) 218–224, `arXiv:hep-ex/0012035 [hep-ex]`.

[34] ATLAS Collaboration, *Observation of a new particle in the search for the Standard Model Higgs boson with the ATLAS detector at the LHC*, Phys. Lett. **B08** (2012) 20.

[35] CMS Collaboration, *Observation of a new boson at a mass of 125 GeV with the CMS experiment at the LHC*, Phys. Lett. **B08** (2012) 21.

[36] F. Zwicky, *On the Masses of Nebulae and of Clusters of Nebulae*, ApJ **86** (1937) 217.

[37] V. C. Rubin and W. K. Ford, Jr., *Rotation of the Andromeda Nebula from a Spectroscopic Survey of Emission Regions*, ApJ **159** (1970) 379.

[38] F. Zwicky, *Die Rotverschiebung von extragalaktischen Nebeln*, Helvetica Physica Acta **6** (1933) 110–127.

[39] F. Zwicky, *On the Masses of Nebulae and of Clusters of Nebulae*, ApJ **86** (1937) 217.

[40] N. Arkani-Hamed, S. Dimopoulos, and G. Dvali, *The hierarchy problem and new dimensions at a millimeter*, Phys. Lett. B **429** (1998) 263 – 272.

[41] O. Klein, *Quantentheorie und funfdimensionale Relativitatstheorie*, Zeitschrift fur Physik A Hadrons and Nuclei **37** (1926) 895–906.

[42] Y. Golfand and E. Likhtman, *Extension of the Algebra of Poincare Group Generators and Violation of p Invariance*, JETP Lett. **13** (1971) 323–326.

[43] A. Neveu and J. H. Schwarz, *Factorizable dual model of pions*, Nucl. Phys. **B31** (1971) 86–112.

[44] A. Neveu and J. H. Schwarz, *Quark Model of Dual Pions*, Phys. Rev. **D4** (1971) 1109–1111.

[45] P. Ramond, *Dual Theory for Free Fermions*, Phys. Rev. **D3** (1971) 2415–2418.

[46] D. Volkov and V. Akulov, *Is the Neutrino a Goldstone Particle?*, Phys. Lett. **B46** (1973) 109–110.

[47] J. Wess and B. Zumino, *A Lagrangian Model Invariant Under Supergauge Transformations*, Phys. Lett. **B49** (1974) 52.

[48] J. Wess and B. Zumino, *Supergauge Transformations in Four-Dimensions*, Nucl. Phys. **B70** (1974) 39–50.

[49] U. Amaldi, W. de Boer, and H. Furstenau, *Comparison of grand unified theories with electroweak and strong coupling constants measured at LEP*, Phys. Lett. **B260** (1991) 447–455.

[50] P. Nath and P. F. Parez, *Proton stability in grand unified theories, in strings and in branes*, Physics Reports **441** (2007) 191 – 317.

[51] G. 't Hooft, *Symmetry Breaking through Bell-Jackiw Anomalies*, Phys. Rev. Lett. **37** (1976) 8–11.

[52] J. Ellis, J. Hagelin, D. Nanopoulos, K. Olive, and M. Srednicki, *Supersymmetric Relics from the Big Bang*, Nuclear Physics B **238** (1984) 453 – 476.

[53] A. H. Chamseddine, R. Arnowitt and P. Nath, *Locally Supersymmetric Grand Unification*, Phys. Rev. Lett. **49** (1982) 970–974.

[54] `PROSPINO2`, `HTTP://WWW.PH.ED.AC.UK/~TPLEHN/PROSPINO/`.

[55] J. Alwall, P. Schuster, and N. Toro, *Simplified Models for a First Characterization of New Physics at the LHC*, Phys. Rev. **D79** (2009) 075020.

[56] CDF Collaboration, *Search for the Production of Scalar Bottom Quarks in ppbar collisions at* $\sqrt{s}$ *= 1.96 TeV*, Phys. Rev. Lett. **105** (2010) 081802.

[57] D0 Collaboration, *Search for scalar bottom quarks and third-generation leptoquarks in ppbar collisions at* $\sqrt{s}$ *= 1.96 TeV*, Phys. Lett. **B693** (2010) 95–101.

[58] CDF Collaboration, *Search for Gluino-Mediated Sbottom Production in* $p\bar{p}$ *Collisions at* $\sqrt{s}$ *= 1.96-TeV*, Phys. Rev. Lett. **102** (2009) 221801.

[59] D0 Collaboration, *Search for associated production of charginos and neutralinos in the trilepton final state using 2.3 fb^{-1} of data*, Phys. Lett. **B680** (2009) 34–43.

[60] CDF Collaboration, *Search for Supersymmetry in $p\bar{p}$ Collisions at $\sqrt{s} = 1.96$ TeV Using the Trilepton Signature for Chargino-Neutralino Production*, Phys. Rev. Lett. **101** (2008) 251801.

[61] CDF Collaboration, *Inclusive Search for Squark and Gluino Production in $p\bar{p}$ Collisions at $\sqrt{s} = 1.96$ TeV*, Phys. Rev. Lett. **102** (2009) 121801.

[62] D0 Collaboration, D0 Collaboration, *Search for squarks and gluinos in events with jets and missing transverse energy using 2.1 fb^{-1} of $p\bar{p}$ collision data at $\sqrt{s}$ = 1.96- TeV*, Phys. Lett. **B660** (2008) 449–457.

[63] LEP SUSY Working Group (ALEPH, DELPHI, L3, OPAL), Notes LEPSUSYWG/01-03.1 and 04-01.1, http://lepsusy.web.cern.ch/lepsusy/Welcome.html.

[64] E. Daw, J. Fox, J.-L. Gauvreau, C. Ghag, L. Harmon, et al., *Spin-Dependent Limits from the DRIFT-IId Directional Dark Matter Detector*, Astropart.Phys. **35** (2012) 397–401.

[65] CDMS II Collaboration, T. Saab, *The CDMS II experiment: Dark matter results from the complete data set*, PoS **IDM2010** (2011) 010.

[66] EDELWEISS Collaboration, P. Loaiza, *Latest results of the edelweiss-II dark matter search experiment*, AIP Conf.Proc. **1338** (2011) 126–129.

[67] M. Benedikt, P. Collier, V. Mertens, J. Poole, and K. Schindl, *LHC Design Report*. CERN, Geneva, 2004.

[68] L. Evans and P. Bryant, *LHC Machine*, JINST **3** (2008) S08001.

[69] CMS Collaboration, *The CMS experiment at the CERN LHC*, JINST **3** (2008) S08004.

[70] LHCb Collaboration, *The LHCb Detector at the LHC*, JINST **3** (2008) S08005.

[71] ALICE Collaboration, *The ALICE experiment at the CERN LHC*, JINST **3** (2008) S08002.

[72] Figure from CERN Public webpages. http://public.web.cern.ch/public/en/research/AccelComplex-en.html.

[73] ATLAS Collaboration, *Expected Performance of the ATLAS Experiment: Detector, Trigger and Physics*, CERN-OPEN-2008-020, 2008.

[74] *ATLAS Fact Sheet*, `http://atlas.ch/fact-sheets.html`.

[75] ATLAS Collaboration, *Performance of the ATLAS Trigger System in 2010*, Eur. Phys. J. **C72** (2012) 1849.

[76] T. Sjostrand, S. Mrenna, and P. Z. Skands, *PYTHIA 6.4 Physics and Manual*, JHEP **05** (2006) 026.

[77] M. Mangano et al., *ALPGEN, a generator for hard multiparton processes in hadronic collisions*, JHEP **07** (2003) 001.

[78] S. Frixione and B. R. Webber, *The MC@NLO 3.2 Event Generator*, `arXiv:hep-ph/0601192`.

[79] H. Baer, F. E. Paige, S. D. Protopescu, and X. Tata, *ISAJET 7.69: A Monte Carlo Event Generator for pp, $\bar{p}p$ and e^+e^- Reactions*, `arXiv:hep-ph/0312045`.

[80] J. Alwall, M. Herquet, F. Maltoni, O. Mattelaer, and T. Stelzer, *MadGraph 5: Going Beyond*, JHEP **06** (2011) 128, `1106.0522`.

[81] A. Djouadi, M. M. Muhlleitner, and M. Spira, *Decays of Supersymmetric Particles: the program SUSY-HIT (SUspect-SdecaY-Hdecay-InTerface)*, Acta Phys. Polon. **B38** (2007) 635–644.

[82] G. Corcella et al., *HERWIG 6: An event generator for hadron emission reactions with interfering gluons (including supersymmetric processes)*, JHEP **01** (2001) 010.

[83] W. Beenakker, R. Hopker, and M. Spira, *PROSPINO: A Program for the production of supersymmetric particles in next-to-leading order QCD*, `arXiv:hep-ph/9611232 [hep-ph]`.

[84] J. Butterworth, J. R. Forshaw, and M. Seymour, *Multiparton interactions in photoproduction at HERA*, Z.Phys. **C72** (1996) 637–646.

[85] GEANT4 Collaboration, S. Agostinelli et al., *GEANT4: A simulation toolkit*, Nucl. Instrum. Meth. **A506** (2003) 250–303.

[86] E. Barberio, et al., *Fast simulation of electromagnetic showers in the ATLAS calorimeter: Frozen showers*, JPCS **160** (2009) 012082.

[87] E. Barberio, et al., *The Geant4-Based ATLAS Fast Electromagnetic Shower Simulation*, ATL-SOFT-CONF-2007-002, 2007.

[88] K. Edmonds, S. Fleischmann, T. Lenz, C. Magass, J. Mechnich, et al., *The fast ATLAS track simulation (FATRAS)*, ATL-SOFT-PUB-2008-001, 2008.

[89] ATLAS Collaboration, *Early supersymmetry searches in events with missing transverse energy and b-jets with the ATLAS detector*, ATLAS-CONF-2010-079, 2010.

[90] ATLAS Collaboration, *ATLAS Computing Technical Design Report*, 2005. CERN-LHCC-2005-022.

[91] G. S. M. Cacciari and G. Soyez, *The anti-k_t jet clustering algorithm*, JHEP **04** (2008) 063.

[92] ATLAS Collaboration, *Jet energy scale and its systematic uncertainty for jets produced in proton-proton collisions at $\sqrt{s}$=7 TeV and measured with the ATLAS detector*, ATLAS-CONF-2010-056, 2010.

[93] ATLAS, *Calorimeter Clustering Algorithms: Description and Performance*, ATL-LARG-PUB-2008-003, 2008.

[94] ATLAS Collaboration, *Performance of the ATLAS Secondary Vertex b-tagging Algorithm in 7 TeV Collision Data*, ATLAS-CONF-2010-042, 2010.

[95] ATLAS Collaboration, *Commissioning of the ATLAS high-performance b-tagging algorithms in the 7 TeV collision data*, ATLAS-CONF-2011-102, 2011.

[96] G. Piacquadio and C. Weiser, *A new inclusive secondary vertex algorithm for b-jet tagging in ATLAS*, JPCS **119** (2008) 032032.

[97] ATLAS Collaboration, *Calibrating the b-Tag Efficiency and Mistag Rate in 35 pb^{-1} of Data with the ATLAS Detector*, ATLAS-CONF-2011-089, 2011.

[98] I. Hinchliffe, F. Paige, M. Shapiro, J. Soderqvist, and W. Yao, *Precision SUSY measurements at CERN LHC*, Phys.Rev. **D55** (1997) 5520–5540.

[99] D. Tovey, *On measuring the masses of pair-produced semi-invisibly decaying particles at hadron colliders*, JHEP **04** (2008) 034.

[100] G. Polesello and D. Tovey, *Supersymmetric particle mass measurement with the boost- corrected contransverse mass*, JHEP **03** (2010) 030.

[101] ATLAS Collaboration, *Updated Luminosity Determination in pp Collisions at $\sqrt{s}$ = 7 TeV using the ATLAS Detector*, ATLAS-CONF-2011-011, 2011.

[102] F. Berends, W. Giele, H. Kuijf, R. Kleiss, and W. Stirling, *Multijet production in W, Z events at pp colliders*, Phys. Lett. **B224** (1989) 237 – 242.

[103] ATLAS Collaboration, *Measurement of the cross section for the production of a W boson in association with b-jets in pp collisions at with the ATLAS detector*, Phys. Lett. **B707** (2012) 418 – 437.

[104] P. M. Nadolsky, H. Lai, Q. Cao, J. Huston, J. Pumplin, et al., *Implications of CTEQ global analysis for collider observables*, Phys.Rev. **D78** (2008) 013004.

[105] *PHYSTAT 2011 Workshop on Statistical Issues Related to Discovery Claims in Search Experiments and Unfolding*. 2011.

[106] J. Neyman and E. S. Pearson, *On the Problem of the Most Efficient Tests of Statistical Hypotheses*, Phil. Trans. R. Soc. Lond. A **231** (1933) 289–337.

[107] A. Wald, *Tests of Statistical Hypotheses Concerning Several Parameters When the Number of Observations is Large*, Transactions of the American Mathematical Society **54** (1943) 426–482.

[108] G. Cowan, K. Cranmer, E. Gross, and O. Vitells, *Asymptotic formulae for likelihood-based tests of new physics*, Eur. Phys. J. (2011) 1554.

[109] G. Cowan, K. Cranmer, E. Gross, and O. Vitells, *Power-Constrained Limits*, `arXiv:1105.3166 [physics.data-an]`.

[110] A. L. Read, *Presentation of search results: the CL_s technique*, J. Phys. G: Nucl. Part. Phys. **28** (2002) 2693.

[111] ATLAS Collaboration, *Search for squarks and gluinos using final states with jets and missing transverse momentum with the ATLAS detector in $\sqrt{s} = 7$ TeV proton-proton collisions*, Phys. Lett. **B710** (2012) 67–85.

[112] ATLAS Collaboration, *Search for gluino-mediated scalar top and bottom quark production in final states with missing transverse energy and at least three b-jets with the ATLAS Detector*, Atlas-conf-2012-058, 2012.

[113] R. Barbieri and G. Giudice, *Upper bounds on supersymmetric particle masses*, Nucl. Phys. **B306** (1988) 63 – 76.

[114] G. Larsen, Y. Nomura, and H. L. Roberts, *Supersymmetry with Light Stops*, JHEP **06** (2012) 32.

[115] ATLAS Collaboration, *Search for squarks and gluinos using final states with jets and missing transverse momentum with the ATLAS detector in $\sqrt{s} = 7$ TeV proton-proton collisions*, Phys. Lett. **B701** (2011) 186–203.

[116] LHCb Collaboration Collaboration, R. Aaij et al., *Strong constraints on the rare decays B_s to $\mu^+\mu^-$ and B^0 to $\mu^+\mu^-$*, Phys.Rev.Lett. **108** (2012) 231801, `arXiv:1203.4493 [hep-ex]`.

[117] F. Mahmoudi, S. Neshatpour, and J. Orloff, *Supersymmetric constraints from $B_s \to \mu^+\mu^-$ and $B \to K * \mu^+\mu^-$ observables*, JHEP **1208** (2012) 092, `arXiv:1205.1845 [hep-ph]`.

[118] L. S. Stark, P. Hafliger, A. Biland, and F. Pauss, *New allowed mSUGRA parameter space from variations of the trilinear scalar coupling A0*, JHEP **08** (2005) 059.

[119] ATLAS Collaboration, *Early supersymmetry searches in channels with jets and missing transverse momentum with the ATLAS detector*, ATLAS-CONF-2010-065, 2010.